ABSTRACT

Title of dissertation: An Unsplit Staggered Mesh Scheme For Multidimensional Magnetohydrodynamics: A Staggered Dissipation-control Differencing Algorithm

Dongwook Lee, Doctor of Philosophy, 2006

Dissertation directed by: Associate Research Professor Anil E. Deane
Institute For Physical Science & Technology

A new unsplit staggered mesh algorithm (USM) that solves multidimensional magnetohydrodynamics (MHD) on a staggered mesh is introduced and studied. Proper treatments of multidimensional flow problems are required for MHD simulations to avoid unphysical results that can even introduce numerical instability. The research work in this dissertation, which is based on an approach that combines the high-order Godunov method and the constrained transport (CT) scheme, uses such multidimensional consideration in a spatial reconstruction-evolution step.

The core problem of MHD simulation is the nonlinear evolution of solutions using well-designed algorithms that maintain the divergence-free constraint of the magnetic field components. The USM algorithm proposed in this dissertation ensures the solenoidal constraint by using Stokes' Theorem as applied to a set of induction equations. In CT-type of MHD schemes, one solves the discrete induction equations to proceed temporal evolutions of the staggered magnetic fields using electric fields. The accuracy of the computed electric fields therefore directly influ-

ence the solution quality of the magnetic fields. To meet this end, an accurate and improved electric field construction (IEC) scheme has been introduced as one of the essential parts of the current dissertation work.

Another important feature in this work is a development of a new algorithm that solves the induction equations with an added capability that controls numerical (anti)dissipations of the magnetic fields. This staggered dissipation-control differencing algorithm (SDDA) makes use of extra dissipation terms, for which their derivations are established from modified equations of the induction equations.

A series of comparison studies in a suite of numerical results of the USM-IEC-SDDA scheme will show a great deal of qualitative improvements in many stringent multidimensional MHD test problems.

An Unsplit Staggered Mesh Scheme For Multidimensional Magnetohydrodynamics: A Staggered Dissipation-control Differencing Algorithm

by

Dongwook Lee

Dissertation submitted to the Faculty of the Graduate School of the
University of Maryland, College Park in partial fulfillment
of the requirements for the degree of
Doctor of Philosophy
2006

Advisory Committee:

Associate Research Professor Anil E. Deane, Chair/Advisor
Professor David C. Levermore
Professor Howard C. Elman
Associate Professor James D. Baeder
Associate Research Professor Kevin Olson

DEDICATION

To my parents for all their everlasting love

ACKNOWLEDGMENTS

I would like to express my sincere gratitude to my advisor, Dr. Anil E. Deane, for steering me toward this graduate research work. His fruitful suggestions and never-ending support have been a bright beacon during all phases of this study.

I would also like to thank Professors James Baeder, David Levermore, Howard Elman, and Kevin Olson for their kind help. I especially thank Dr. Kevin Olson for his support and help for implementing my research code with the PARAMESH Adaptive Mesh Refinement library. Without his advice, I might still wander to find hidden bugs in my MHD code.

I am grateful to my great friends with whom I had pleasure to work and enjoy. I have been very fortunate to share the sense of friendship and integrity that we all experienced together.

I would like to acknowledge the ASC FLASH Center at the University of Chicago. All my experiences working with them have been always challenging and creative. It is also a true privilege to have a chance to join them for my post-doctoral career.

Most of all, I want to thank my parents for their unlimited love and support of my endeavor throughout all of my endless graduate years.

TABLE OF CONTENTS

LIST OF TABLES

LIST OF FIGURES

Chapter 1

INTRODUCTION

If you wish to make an apple pie truly from scratch,

you must first invent the universe.

Carl Sagan

The latest available challenges of the numerical MHD simulations are discussed in Chapter 1. Among many others, three major solenoidal constraint preserving algorithms are briefly compared with an emphasis on the divergence-free constraint property in various CT-type MHD solvers. The physical importance to keep the divergence-free fields in MHD simulations will be first discussed, and different numerical approaches to preserve the solenoidal magnetic fields will be inter-compared. Based on the comparison study, several key advantages in using the CT-type of divergence-free approach, from which the USM-IEC-SDDA algorithm stems, will be drawn.

The general ideas given in Chapter 1 will be extended to develop algorithms of the USM-IEC-SDDA in the following chapters. To this end, related issues in each different MHD scheme will be first overviewed and then important consequences of introducing the USM scheme with the IEC and SDDA developments will be laid out.

The last part of the chapter is devoted to discuss the validity of MHD theory.

Major interest covers the basic concepts of physical motivations to develop MHD theory, which can be approached using from the kinetic theory to the fluid (multi-fluid, two-fluid and single-fluid) theories. Several conditions of validity for MHD theory will be outlined.

1.1 Motivation

USM-IEC-SDDA is a multidimensional MHD scheme that uses a staggered mesh algorithm combined with an unsplit time integration method. The method is a second-order finite volume Godunov algorithm which has a TVD version of the MUSCL-Hancock scheme. This unsplit approach is found to be more accurate than most dimensional splitting time integration methods, where there are generally operator splitting errors. The current MHD algorithm conveys full aspects of multidimensional MHD problems. Most importantly, the solenoidal constraint of the magnetic fields by using a staggered mesh algorithm (Balsara *et al.*, 1999 [9]; Balsara, 2001 [10, 11]) has been successfully achieved in the USM-IEC-SDDA development.

The staggered mesh algorithm is shown to be very efficient (Tóth, 2000 [88]) for maintaining the divergence-free constraint on the magnetic fields in solving MHD problems numerically. The staggered mesh algorithm updates the magnetic field components (surface variables) by preserving the divergence-free constraint up to round-off error. The staggered mesh algorithm further uses a Godunov-type finite volume scheme as an underlying solver to update the rest of the volumetric variables

(e.g., density, momentum, and total energy). An approximate Roe-type Riemann solver is then a good choice to compute the high-order Godunov fluxes at each cell interface center.

In Godunov-type finite volume schemes there are two approaches to update temporal integrations of multidimensional conservation laws: the dimensional splitting and unsplit methods. The simplest and comparatively less expensive way is to use the dimensional splitting method. This type of method, which is simply an extension of the finite volume scheme in one-dimension to multi-dimension, is shown to be robust, relatively straightforward to implement, and generally faster than the unsplit method. The method, however, does generally introduce splitting errors when solving one-dimensional subproblems in each sweep direction. This is because the linearized Jacobian flux matrices do not commute, e.g., $\bar{\mathbf{A}}_x\bar{\mathbf{A}}_y \neq \bar{\mathbf{A}}_y\bar{\mathbf{A}}_x$, in most of the nonlinear multidimensional problems [53, 54].

Alternatively, one can use the unsplit method to update the cell averaged solutions by simultaneously accounting for the flux contributions from all interface boundaries in a single step. This approach is more accurate than the splitting scheme, and forms a basis of the scheme in this dissertation to solve the multidimensional MHD equations. Compared to the dimensional splitting algorithm, the unsplit scheme usually requires more storage, and its implementation has been quite limited for use of MHD schemes. Crockett *et al.* [26] have recently presented an unsplit MHD scheme, based on the unsplit algorithm for hydrodynamics of Colella [24], using a projection divergence-cleaning method.

The staggered mesh algorithm has a major advantage over the projection

scheme in that it is computationally inexpensive. It also has many attractive features, such as that it can be easily applied with different boundary conditions or different types of zoning. This is in contrast with most of the FFT based projection schemes, for which the choice of boundary conditions are very restrictive. While many works [6, 21, 46] have used multigrid methods in incompressible flows and such restrictions seem much less severe, the numerical design still requires extra implementations, whereas the staggered mesh algorithm does not.

One of the well known difficulties in modern MHD codes is to keep the $\nabla \cdot \mathbf{B} = 0$ constraint throughout simulations. This constraint comes from the physical observation that there are no isolated magnetic sources or monopoles. This implies that the magnetic field lines, which are tangent to $\mathbf{B}$, are closed or have ends at infinity. Ideally, one would like to have the same constraint in his/her numerical scheme to avoid unphysical effects. Violating the $\nabla \cdot \mathbf{B} = 0$ constraint allows errors to be accumulated over each time step and may produce erroneous solutions [18]. Several attempts have been made to maintain the $\nabla \cdot \mathbf{B} = 0$ constraint in shock-capturing MHD codes. As recent studies have shown; however, successful development of such comprehensive code is a difficult problem. The issues in such schemes have been well documented and compared by Tóth [88]. The formulations within shock-capturing high-order Godunov-type schemes can be categorized into three major approaches.

The first approach is the *constrained transport* (CT) type of schemes on a staggered mesh, originally proposed by Yee (1966) [94], and studied by many others [9, 11, 19, 28, 33, 34, 37, 59, 78]. Recently Balsara and Spicer [9] proposed a CT scheme

(flux-CT) that utilizes high-order Godunov fluxes to construct electric fields, followed by an update of the divergence-free magnetic fields by solving the induction equations with the electric fields. Historically, the name, *constrained transport*, was first introduced by Evans and Hawley [34], and it simply means a particular choice of finite difference discretization on a staggered grid that maintains $\nabla \cdot \mathbf{B} = 0$ in the discretized form of equations. In the CT-type of schemes, the accuracy of round-off errors can be achieved in the discretized form of $\nabla \cdot \mathbf{B} = 0$, provided that the initial and boundary conditions satisfy the divergence-free condition. Tóth [88] compares seven different algorithms which are widely used in modern MHD codes and underscores both the physical and numerical importance of maintaining the solenoidal constraint in MHD problems. In his study, Balsara and Spicer's flux-CT scheme is shown to be the most accurate scheme for the test problems therein. The next section will discuss several different approaches and key ideas adopted in the CT schemes in more detail.

The second approach is the *projection* scheme, first proposed by Brackbill and Barnes (1980) [18] for use in MHD. The basic idea behind this method is to construct a mathematical vector space and its subspace, where the non divergence-free magnetic fields are projected to the subspace of zero divergence fields by a linear operator. In each time step, these projections (or corrections) of magnetic fields are performed by solving corresponding Poisson equations and the divergence-free mode of magnetic fields can be obtained to the same order of accuracy as the Poisson solver. The approach is shown to be very accurate and works well for any grid on which the Poisson equation can be solved (even on unstructured grids). It

has, however, the additional complexity of computing the Poisson solution at each time step. There are two choices in the projection of the magnetic fields, either to project the cell-centered fields or face-centered fields. The first is consistent with the underlying topologies of the cell center based Godunov schemes; however, there are some numerical issues such as energy imbalance from the changes in the cell-centered magnetic fields in the fluid as well as the checkerboard-type instabilities involving a centered difference approximation to the divergence operator. The second type of projection, also called the MAC projection [26], has as its advantage that it uses the projected divergence-free fields in calculating fluxes and therefore is more reliable in keeping the algorithm conservative.

The third approach is the *8-wave (or divergence-wave)* formulation which was suggested by Powell *et al.* [68]. This method solves the MHD equations using an additional eighth wave of the governing equations. The formulation requires some source terms, proportional to $\nabla \cdot \mathbf{B}$, on the right hand side of the governing equations, where they are residual terms that cannot be expressed in divergence form in their cell-centered field formulation. Since the scheme uses an additional eighth wave corresponding to monopoles, such unphysical monopoles will effectively travel at the flow speed over time and presumably be advected out of the domain eventually. The scheme also requires a minor modification to an approximate Riemann-type solver due to its extra wave structure of the scheme. Powell *et al.* [68] also cited another downside of the method in solving the governing equations with additional source terms: the truncation error is reflected on the right hand side of the equations proportional to the order of the truncation error of $\nabla \cdot \mathbf{B}$. In turn, this makes the

scheme to be non-strictly conservative and hence the method can give incorrect jump conditions across discontinuities. However, for many practical problems of interest, even with this non-conservative property, the 8-wave formulation is found to be robust in terms of stability and accuracy.

The current motivation in developing MHD solvers that retain the $\nabla \cdot \mathbf{B} = 0$ property stems from the solar wind modeling work [40, 74, 79]. An approach therein used Flux Corrected Transport (FCT), a method that does not require a Riemann solver, and employed a staggered mesh with cell-centered and face-centered magnetic fields and edge-based electric fields. That code solves the full 3D MHD system in spherical coordinates and thus obtains the radial expansion of the solar wind in a natural way. An AMR (adaptive mesh refinement) version has been formulated in [29]. It is envisioned that the method presented in this dissertation, when extended to 3D, will be eminently suitable for solar wind work. It will retain the unsplit multidimensional staggered mesh arrangement, thus preserving the $\nabla \cdot \mathbf{B} = 0$ condition in a similar way to FCT, but provide a significantly more accurate and robust approach in that it is less diffusive.

The goal in this dissertation is to develop a new unsplit MHD solver for multidimensional flow problems, and is fourfold. Firstly, a new unsplit method that employs a method of *multidimensional* characteristic analysis for reconstructing the Riemann state variables has been introduced. The characteristic method will be shown to be very efficient to treat multidimensional MHD terms. This is in contrast to all previous approaches have used *one-dimensional* characteristic tracing method to reconstruct the Riemann states. The development of the characteristic method

is discussed in Chapter 2.

Secondly, the base flux-CT scheme of Balsara and Spicer has been extended to develop a new electric field construction scheme on a staggered grid. In this development, a new high-order construction algorithm will be presented that provides more accurate directional gradient information as well as an improved treatment of numerical dissipations. This algorithm, which will be called as an *improved electric field construction* (IEC) scheme, is described in Chapter 3.

Thirdly, a new (anti)dissipation relationship has been established in solving the MHD induction equations by considering modified equations of the induction equations. Such (anti)dissipation control will be shown to play an important role to prevent unphysical growths of the components of the magnetic field in MHD simulations. Details of the development, which will be designated as *staggered dissipation-control differencing algorithm* (SDDA), is discussed in Chapter 4.

Finally, an implementation of a parallel, adaptive mesh refinement (AMR) version of USM-IEC-SDDA will be described in Chapter 5. The implementation has been achieved in the FLASH 3 simulation code [36] using the PARAMESH AMR library [62].

In Chapter 6, results of several test problems are presented, including the Brio-Wu shock tube [20], field loop advection/diffusion problems [37, 82], Orszag-Tang vortex [65], rotor problem [9,11,55,56,60,88], shock-cloud interaction problem [28, 56, 88], MHD blast problem [11, 95], and current sheet problem [37, 82]. It will be shown that the USM-IEC-SDDA scheme has a great capability to solve these stringent MHD problems in multidimension.

Several conclusions and future work will be drawn in Chapter 7.

1.2 Divergence-Free MHD Algorithms

In this section, discussions of several key aspects in multidimensional MHD flow problems will be made. Such discussions will underline the numerical efficiency and robustness of the background of the USM-IEC-SDDA scheme. Concepts of the electric fields construction and the evolutions of the induction equations on the staggered grid will also be presented briefly and they will be further developed for the USM-IEC-SDDA scheme in later chapters.

1.2.1 Divergence-Free Requirement for MHD

A well-designed numerical MHD algorithm should generate solutions that reflect the fact that there are no isolated magnetic monopoles. It is due to Brackbill and Barnes (1980) [18] that violating the $\nabla \cdot \mathbf{B} = 0$ constraint can cause fictitious forces to develop parallel to the magnetic fields. This results in additional extra source terms in the momentum, induction and energy equations. For instance, one can see that the Lorentz force per unit volume (assuming overall charge neutrality) can be written as

$$\begin{aligned} \mathbf{j} \times \mathbf{B} &= (\nabla \times \mathbf{B}) \times \mathbf{B} && (1.1) \\ &= (\mathbf{B} \cdot \nabla)\mathbf{B} - \frac{1}{2}\nabla B^2 && (1.2) \\ &= \nabla \cdot (\mathbf{B}\mathbf{B}) - (\nabla \cdot \mathbf{B})\mathbf{B} - \frac{1}{2}\nabla B^2, && (1.3) \end{aligned}$$

where $\mathbf{j}$ and B are the current density and magnitude of the magnetic fields, respectively. Note that the first and second terms in equation (1.2) represent the forces from the magnetic tension and magnetic pressure, respectively.

If $\nabla \cdot \mathbf{B} = 0$, then one can rewrite the last equation (1.3) in a conservation form as the divergence of the Maxwell stress tensor $T = \mathbf{BB} - \frac{B^2}{2}\mathbf{I}$:

$$\mathbf{j} \times \mathbf{B} = \nabla \cdot (\mathbf{BB}) - \frac{1}{2}\nabla B^2 = \nabla \cdot T, \tag{1.4}$$

where $\mathbf{I}$ is a unit matrix. As a consequence, when $\nabla \cdot \mathbf{B} \neq 0$ this conservation form of the Lorentz force is violated and hence the MHD equations are no longer to be conservative (See more details in [18]). Furthermore, the nonzero value of $\nabla \cdot \mathbf{B}$ is proportional to $\mathbf{B}$ and hence there will be an extra compressive magnetic component parallel to the magnetic fields. This will allow unphysical magnetic acceleration along the field lines. Notice that the gas pressure p is

$$p = (\gamma - 1)(E - \frac{1}{2}\rho U^2 - \frac{1}{2}B^2), \tag{1.5}$$

where E, U, and B are the total energy density, magnitudes of velocity fields and magnetic fields, respectively. The above equation (1.5) shows that if there is an extra development of magnetic compressive components due to the nonzero $\nabla \cdot \mathbf{B}$ value, then the magnetic pressure $\frac{1}{2}B^2$ will be increased and hence the gas pressure p will be apparently reduced during the simulation. The greater the magnetic force acceleration is relative to the fluid velocity the lesser the fluid velocity is relative to the Alfvén wave. In numerical simulations, $\nabla \cdot \mathbf{B}$ is typically small, but not exactly zero. Since $\nabla \cdot \mathbf{B}$ itself is a numerical discretization error, the resultant

error would be accumulated over the computational domain and may produce an erroneous solution.

1.2.2 Cell-centered Fields Algorithms in High-Order Godunov MHD

Over the last decade the high-order Godunov method, one of the accurate and robust schemes originally developed in hydrodynamics, has become a great interest for use in MHD. A brief list of developments includes Brio and Wu (1988) [20], Zachary, Malagoli, and Colella (1994) [95], Dai and Woodward (1994) [27], Powell *et al.* (1994) [68], Ryu and Jones (1995) [77], Balsara and Spicer (1998) [9], Londrillo and Del Zanna (1999) [59], Pen *et al.* (2003) [67], Londrillo and Del Zanna (2004) [60], Balsara (2003) [11], Crockett *et al.* (2005) [26], and Gardiner and Stone (2005) [37].

The high-order Godunov scheme was first developed by van Leer (1979) for Euler flows and substantial progress thereafter has opened a new era of robust and accurate performance in numerical simulations of MHD as well as hydrodynamics. It is interesting to notice that early efforts in high-order Godunov MHD schemes focused entirely on the numerical formulations that collocate the magnetic fields at zone centers. This was because of the fact that the underlying aspects of the Godunov algorithms are based on the conservation laws in which the zone centered variables are conserved. The MHD equations, thus, were treated as a simple system of conservation laws in earlier formulations.

In the cell-centered fields formulations one does not encounter any difficulty

until one tries to solve multidimensional MHD problems. This is because in one-dimensional MHD the normal field is held to be a constant and there is no need to worry about keeping the divergenceless evolution of the magnetic fields. In multidimensional MHD, however, one needs to maintain the solenoidal constraint via solving the induction equation. For instance the induction equation for the ideal MHD has the form:

$$\frac{\partial \mathbf{B}}{\partial t} + \nabla \times \mathbf{E} = 0. \tag{1.6}$$

A correct interpretation of the above induction equation does not mean to follow any conservation law but the divergenceless evolution of the magnetic fields. This can be seen by taking the divergence of the induction equation (1.6):

$$\frac{\partial \nabla \cdot \mathbf{B}}{\partial t} = \nabla \cdot (-\nabla \times \mathbf{E}) = 0. \tag{1.7}$$

Apparently this analytical result may not be true numerically, because the discrete divergence of the discrete curl may not give zero exactly.

Until recently, two traditional approaches have been proposed to enforce the divergence-free constraint in the formulations using the cell-centered fields. The first method is the projection method, which, in the context of MHD, was first proposed by Brackbill and Barnes [18] (also earlier work in [8, 77, 95] and recently in [26]), takes a divergence-cleaning step in their high-order Godunov based MHD schemes. In this approach two types of schemes are available, a scalar divergence-cleaning type and a vector divergence-cleaning type, depending on a choice of a space in which the divergence-cleaning is evaluated: real space or Fourier space. This method potentially contains some disadvantages. One needs to pay the price

to solve the associated Poisson problems either directly or iteratively. This, in general, is computationally expensive with possible restrictions on boundary conditions and difficulties on non-Cartesian domains. Also, since the method requires a global solution to the Poisson problem the approach has no choice to avoid all-to-all communication on a parallel machine. Another disadvantage in this method is the extra complexity because the discretization of the elliptic equation must be compatible with that of the MHD equations. With a lot of efforts, an adaptive mesh refinement (AMR) can be accommodated in the scalar divergence-cleaning approach, yet it would be hobbled in solving the Poisson problems and become progressively computationally expensive as the AMR hierarchy increases. Finally, the situation becomes even worse for the vector divergence-cleaning approach, in that there seems to be no AMR algorithm available yet. More details on other various numerical issues for this approach have been well cataloged in [12, 88].

The second method, the so-called 8-wave formalism, proposed by Powell *et al.* [70], utilizes the modified MHD equations that includes source terms that are proportional to $\nabla \cdot \mathbf{B}$. An additional eighth wave reflects the propagation of the magnetic monopole that is designed to be convected with the local flow speed, and eventually advected out of the computational domain. Although the scheme is found to be robust and accurate (as compared to the basic conservative scheme), obviously this set-up results in non-conservative forms of the MHD governing equations and is susceptible to produce incorrect jump conditions and propagation speed across discontinuities in certain problems [70, 88]. Due to its inherent formalism allowing the truncation error of $\nabla \cdot \mathbf{B}$ that travels with the local flow, the price this scheme

should pay is the loss of the divergence-free property. Potentially this would lose the important physics of MHD and hence the magnetic field topologies. Recently, there also have been other approaches [31, 48] to extend the 8-wave schemes that manifest the $\nabla \cdot \mathbf{B}$ source term.

1.2.3 Cell Face-centered Fields Algorithms in High-Order Godunov MHD: the Staggered Mesh Algorithm

For the reasons that have been raised in the high-order Godunov based MHD formulations using the cell-centered fields, and to overcome such issues, many researchers have developed various efficient staggered mesh algorithms by taking an alternative line of thought that uses a staggered collocation of the magnetic fields. The basic idea in the staggered approach is to evolve MHD flows by solving the MHD induction equation (1.6) via Stokes' Theorem in a discrete sense.

The staggered grid algorithm was first introduced by Yee (1966) [94] to compute the divergence-free MHD flow in the finite difference formulation that transports the electromagnetic fields. Ever since, many approaches have been proposed to use the staggered grid to keep $\nabla \cdot \mathbf{B} = 0$. Bretcht *et al.* (1981) [19] used the staggered mesh formulation for their global MHD modeling of Earth's magnetosphere for which they used a non-linear FCT flux limiter. The *constrained transport* (CT) method later by Evans and Hawley (1988) [34] followed the vector potential approach on the staggered grid for evolutions of the MHD induction equations. Another approach by DeVore (1991) [33] also used the staggered mesh algorithm of

Brecht *et al.* [19] and applied it to a flux corrected transport (FCT) algorithm.

Due to Evans and Hawley [34], the name *constrained transport* (CT) has become a popular name that encompasses all the branches that have been developed in the staggered mesh approaches [9, 11, 28, 33, 34, 37, 59, 78]. The original CT method places the surface variable (or the magnetic flux) – the components of the magnetic field at the cell face centers, and the rest of the volumetric variables such as mass, momentum and energy at the cell centers on the staggered grid. There also has been a variant CT approach by Tóth [88] that places all of the variables at the cell centers and uses central differencing for the induction equation. In his paper, Tóth made an extensive and comparative study of different MHD schemes focusing on the divergence-free property of each scheme. He compared the various approaches that are different in how the base scheme (*e.g.* van Leer's TVD-MUSCL, or Yee's TVD-Lax Friedrich) is modified regarding the induction equation. Tóth's study did not only compare three *major* different algorithms (*e.g.* the projection schemes, the 8-wave schemes, and the CT based staggered mesh schemes) but also different approaches in the CT formulation.

In the CT schemes, different approaches adopt different ideas on how to obtain the electro-motive force (EMF) $\mathbf{E}$, which can be defined by $\mathbf{E} = -\mathbf{u} \times \mathbf{B}$ as a simple case in ideal MHD. The *flux*-CT scheme by Balsara and Spicer [9] uses the second-order Godunov fluxes to construct the EMF by using the so-called duality relationship between the components of the flux vector and the electric fields. The *field-interpolated* CT scheme designed by Dai and Woodward [28] simply uses the interpolated magnetic and velocity fields to obtain the EMF in their Godunov-type

formulation. Ryu *et al.* [78] also proposed the *transport-flux-interpolated* CT scheme which basically transports the upwind fluxes along with the upwind correction terms for maintaining the TVD property. Balsara's series of recent work [10, 11] studied a new reconstruction algorithm for the cell-centered magnetic fields. In his *modified*-CT approach the magnetic fields at each cell center are reconstructed directly from the divergence-free cell face-centered field components using the reconstruction polynomial. Such reconstructed magnetic fields at the cell centers (not only the cell face fields) are also guaranteed to maintain the divergence-free constraint by design. Recently, Gardiner and Stone [37] developed a multidimensional CT scheme that is consistent with the plane-parallel, grid-aligned one-dimensional base flow problems by modifying the simple arithmetic electric fields averaging scheme of Balsara and Spicer [9]. As another approach, *upwinding*-CT (UTC) scheme, was proposed in Londrillo and Del Zanna [60]. Their approach used a similar reconstruction algorithm as described in [10, 11] for the magnetic fields and evaluate the EMF based on the upwinding strategy in their Godunov-type scheme. In the UTC scheme, the divergence-free property is maintained as a built-in property. Yet it is evident from their test results that their scheme suffers from keeping $\nabla \cdot \mathbf{B}$ sufficiently low, and allowing up to the order of 10^{-4} (See [59]), while, it will be shown in later chapters that, the USM-IEC-SDDA scheme allows $\nabla \cdot \mathbf{B}$ only up to the orders of $10^{-12} \sim 10^{-16}$ in most of the simulations.

It is worth mentioning that, in Tóth's work [88], one of the most accurate high-order MHD schemes is the flux-CT scheme by Balsara and Spicer [9]. Recently, Balsara [10, 11] has extended his original flux-CT scheme on an AMR grid.

According to the observation have made so far, in this dissertation a CT approach which stems from the work of Balsara and Spicer [9] is adopted and extended to develop the USM-IEC-SDDA scheme.

In Chapter 3, a new electric field construction algorithm (IEC) will be presented that improves the base construction scheme of Balsara and Spicer [9]. Later in Chapter 4, the improved electric field construction (IEC) algorithm will be used to solve the induction equations according to the SDDA scheme.

1.3 Basic Properties of MHD

The ideal MHD equations can be formulated as a hyperbolic system of conservation laws. High-order Godunov schemes are often preferable to more traditional schemes such as FCT to solve this conservative system to increase the accuracy of numerical solution. In general the resistive MHD equations can be written in a quasi-conservative form as following:

$$\frac{\partial \rho}{\partial t} + \nabla \cdot (\rho \mathbf{u}) = 0, \tag{1.8}$$

$$\frac{\partial \rho \mathbf{u}}{\partial t} + \nabla \cdot (\rho \mathbf{u}\mathbf{u} - \mathbf{B}\mathbf{B}) + \nabla p_{tot} = 0, \tag{1.9}$$

$$\frac{\partial \mathbf{B}}{\partial t} + \nabla \cdot (\mathbf{u}\mathbf{B} - \mathbf{B}\mathbf{u}) + \nabla \times (\eta \mathbf{j}) = 0, \tag{1.10}$$

$$\frac{\partial E}{\partial t} + \nabla \cdot (\mathbf{u}e + \mathbf{u}p_{tot} - \mathbf{B}\mathbf{B} \cdot \mathbf{u} - \mathbf{B} \times \eta \mathbf{j}) = 0. \tag{1.11}$$

The above equations represent the continuity equation, momentum equation, induction equation, and energy equation, respectively.

The conservative variables are the plasma mass density ρ, plasma momentum density $\rho\mathbf{u}$, magnetic field $\mathbf{B}$, and total energy density E. The plasma velocity $\mathbf{u}$,

current density $\mathbf{j} = \nabla \times \mathbf{B}$, total pressure $p_{tot} = p + \mathbf{B}^2/2$, and thermal pressure $p = (\gamma - 1)(E - \frac{1}{2}\rho U^2 - \frac{1}{2}B^2)$ are derived quantities, where $U^2 = u^2 + v^2 + w^2$ and $B^2 = B_x^2 + B_y^2 + B_z^2$. Flow parameters include the ratio of specific heats γ and resistivity η. The initial conditions should satisfy $\nabla \cdot \mathbf{B} = 0$.

The resistivity η is zero for ideal MHD, otherwise $\eta > 0$. The resistive MHD equations are formally of mixed type, containing both hyperbolic waves which satisfy a causality condition and have a finite domain of dependence, as well as parabolic diffusion, due to the term $\nabla \times (\eta \mathbf{j}) = \eta \nabla^2 \mathbf{B}$ in the induction equation (1.10), in which the term describes diffusion of the magnetic field with a formally infinite domain of dependence. For zero resistivity ($\eta = 0$) the ideal MHD equations are hyperbolic and admit wave-like solutions that propagate without dissipation. As long as the advection time scale is short compared to the resistive time scale, the numerical techniques applicable to the ideal MHD equations are also suitable for resistive MHD and numerical schemes have mostly been developed for solving the ideal equations.

There are some interesting properties of the ideal MHD equations: the system of equations is not strictly hyperbolic due to the fact that the wave speeds can be equal. The ideal MHD equations yield non-convexity, which allows the existence of compound waves. The wave structure of ideal MHD consists of three different families: slow, Alfvén, and fast waves, and they give more complicated structures than in the pure hydrodynamics case. The Alfvén wave is linearly degenerate and propagates with a speed $v_A = |\mathbf{B}|/\sqrt{\rho}$, whereas fast and slow waves involve compression of plasma and are related to ordinary sound waves propagating with the

sound speed.

This Alfvén speed v_A is indeed a fundamental quantity in the fluid description of MHD. As it will be discussed in the next section, v_A is the characterization of the very-low frequency fluid-like macroscopic dynamics of the magnetic field lines to which the plasma is fastened. The Alfvén waves are consequence of the magnetic tension, as appeared in the first term of the Lorentz force (1.2), which tends to restore the initial shape just like in the way that a sling-shot exerts a force directed to the local center of curvature. Furthermore, since the frequency of the macroscopic MHD depend on the wavelength[1], the slowest waves have the longest wavelengths. This points to a fundamental property of the Alfvén waves that they *feel* the global magnetic configuration, viz., Alfvén waves carry the information of the overall magnetic geometry.

The formidable complexity in numerical MHD problems is to keep the divergence-free constraint properly. In simulations of MHD flow problems, violating the divergence-free constraint would lead to unphysical parallel force to the magnetic field [18]. As was discussed previously, by losing the constraint, the magnetohydrodynamics equations are no longer to be in conservation form. Even with very small errors in preserving the divergence-free constraint can lead to large errors in the solutions of the conservative form of the magnetohydrodynamics equations. In the work of Brackbill and Barnes [18], such erroneous effect was first studied, and a use of non-conservative formulation of the momentum equation, rather than the conservative

[1]This is in contrast with the fact that the microscopic plasma oscillations with the plasma frequency is independent of the wavelength.

form, was proposed to eliminate the non divergence-free error.

The equations of ideal MHD can be written in a conservative form (or divergence form). The ideal part (i.e., $\eta = 0$) of the equations (1.8)$\sim$(1.11), thus, can be rewritten in a short form of a conservative system equation in full three-dimensions as

$$\frac{\partial \mathbf{U}}{\partial t} + \frac{\partial \mathbf{F}}{\partial x} + \frac{\partial \mathbf{G}}{\partial y} + \frac{\partial \mathbf{H}}{\partial z} = 0, \tag{1.12}$$

where $\mathbf{U}$ contains the eight MHD conservative variables and $\mathbf{F}, \mathbf{G}, \mathbf{H}$ represent corresponding conservative fluxes in x, y, z directions respectively.

One can find that $\mathbf{U}$ is given as

$$\mathbf{U} = (\rho, \rho u, \rho v, \rho w, B_x, B_y, B_z, E)^T, \tag{1.13}$$

and multidimensional fluxes $\mathbf{F}, \mathbf{G}, \mathbf{H}$ are also given by

$$\mathbf{F} = \begin{pmatrix} \rho u \\ \rho u^2 + p_{tot} - B_x^2 \\ \rho uv - B_y B_x \\ \rho uw - B_z B_x \\ 0 \\ uB_y - vB_x = -E_z \\ uB_z - wB_x = E_y \\ (E + p_{tot})u - B_x(uB_x + vB_y + wB_z) \end{pmatrix}, \tag{1.14}$$

$$\mathbf{G} = \begin{pmatrix} \rho v \\ \rho v u - B_x B_y \\ \rho v^2 + p_{tot} - B_y^2 \\ \rho v w - B_z B_y \\ v B_x - u B_y = E_z \\ 0 \\ v B_z - w B_y = -E_x \\ (E + p_{tot}) v - B_y (u B_x + v B_y + w B_z) \end{pmatrix}, \tag{1.15}$$

$$\mathbf{H} = \begin{pmatrix} \rho w \\ \rho w u - B_x B_z \\ \rho w v - B_y B_z \\ \rho w^2 + p_{tot} - B_z^2 \\ w B_x - u B_z = -Ey \\ w B_y - v B_z = E_x \\ 0 \\ (E + p_{tot}) w - B_z (u B_x + v B_y + w B_z) \end{pmatrix}. \tag{1.16}$$

Notice that Ohm's law for perfectly conducting plasma, $\mathbf{E} = -\mathbf{u} \times \mathbf{B}$, has been used, where $\mathbf{E} \equiv (E_x, E_y, E_z)^T$, is the electromotive force (EMF, or simply the electric fields).

In one-dimensional problems, one often uses 1.5D (or 1.75D) to represent symmetry-reduced 2D problems. This allows one to keep track of the component of $\mathbf{B}$ perpendicular to the x axis (i.e., B_y or B_z). For instance, we have

$$\mathbf{U} = \begin{cases} (\rho, \rho u, \rho v, B_y, E)^T & \text{for 1.5D,} \\ (\rho, \rho u, \rho v, \rho w, B_y, B_z, E)^T & \text{for 1.75D.} \end{cases} \tag{1.17}$$

For example, one of the well known one-dimensional problems such as the Brio-Wu MHD shock tube problem is of 1.5-dimension in this sense. Notice that in one-dimension, $\nabla \cdot \mathbf{B} = 0$ implies B_x to be constant in both cases, reducing the number of the conserved variables by one. With the reduced number of governing equations in one-dimensional MHD problems, the divergence-free constraint of magnetic fields is satisfied trivially, and it is not required to implement any *divergence-cleaning* routine. However, the situation is different in multidimension. For instance, in two-dimensional Orszag-Tang MHD vortex problem, the initial conditions are given by smooth sinusoidal waves and they evolve into complicated wave structures, i.e., the magnetic fields are no longer to be constant. A proper divergence cleaning scheme should be then applied to keep $\nabla \cdot \mathbf{B} = 0$ in this case.

In designing such multidimensional MHD solvers, it should be noted in multi-dimension, an unsplit scheme is more natural because the system of the governing equations (1.12) is written that way. Splitting such full multidimensional equations into one-dimensional subproblems results in unphysical situations, in that the non-linearly coupled systems are forced to be decoupled. Although the formal accuracy of the dimensional splitting formulation is the same as the accuracy of the unsplit method the splitting method can potentially cause unphysical errors due to the

operator splitting. Also it is to be noted that when the splitting scheme is used, the one-dimensional MHD equations exclude the possibility of jumps in the normal field. While this is clearly acceptable in one-dimension, this can decrease accuracy in multidimension since nonlinear waves propagate not only along the cardinal axes, but also to any direction.

For many purposes, astrophysical flows are highly compressible. A choice with Godunov-type formulations, thus, appears to be an attractive approach for this class of problem. Godunov-type techniques are based on the finite volume scheme. In constructing computational models for compressible flows it is advantageous to introduce a numerical scheme that allows weak solutions, i.e., discontinuous solutions such as contact or rotational discontinuity or shock waves. The most desirable choice is to use the finite volume discretization, as the integral form of the equations is same as the analytical definition of weak solutions, and hence the scheme automatically satisfies the conservation property. In general, the theory (such as Lax equivalence theorem) of the consistency, stability, and convergence of a numerical scheme are only valid for smooth solutions and therefore one cannot guarantee that an arbitrary numerical scheme could correctly approximate weak solutions if other types of discretization (e.g., finite difference, finite element) are employed straightforwardly.

1.4 Limits of MHD Theory

At this point it is useful to outline MHD theory and discuss the regions of validity. MHD is a macroscopic, non-relativistic theory to study large-scale (global)

and low-frequency (slow) phenomena in magnetic plasmas. Quite recently, the desire to understand the basic properties of plasma has largely stimulated by ranges of physical recognition of the importance of solar physics, space physics, and astrophysics. Especially in the 1950s, prospects for the development of safe controlled thermonuclear fusion energy have unleashed a new era towards fusion research, such as early pinch experiments and tokomaks.

One of the remarkable plasma phenomena out in the universe is that the Sun emits a highly conducting tenuous plasma, called the solar wind, which is a consequence of the hot ($1 \sim 2 \times 10^6$ K) corona. Closer at home, such high speed solar wind and the magnetic storms on the Sun interact with the Earth. Luckily, the Earth resides within a vast magnetic cavity, called the magnetosphere, and it is not vulnerable to attack from the sky. The existence of the magnetosphere is a consequence that the solar wind reacts to the magnetic field of the Earth and is deflected by shock waves around the fields. In a bigger picture, the Sun also has its own magnetosphere, called the heliosphere, which contains most of the solar system but not the most distant comets. The importance of understanding plasma physics, therefore, arises when one realizes almost all astrophysical objects are in the plasma state, the fourth state.

Down on the Earth, human beings seek for an almost unlimited and relatively clean means for energy production, and controlled nuclear fusion seems to be the best solution for that. One of the main obstacles for this ambitious plan is to provide a way to confine and control plasmas with high temperatures of the order of 10^8 K and with high densities of $10^{20}\mathrm{m}^{-3}$. It is clear that there are no material containers

that can hold these hot and dense plasmas during times in the order of minutes (or at least seconds) without immediately burning. One way to solve this problem is to use the confining properties of the magnetic fields. All these scientific desires have triggered off theoretical and experimental research into the properties of magnetic plasmas.

A plasma is a macroscopically electrically charged neutral substance with many interacting free electrons and ions which exhibit *collective behavior* due to the long-range[2] Coulomb forces. Thus, a plasma can be viewed as a large N-body system[3] of mobile charged particles and electromagnetic fields. To understand and solve the system of plasmas, many practitioners have developed a number of plasma models.

The kinetic model, which contains all the relevant physical phenomena, is hard to be solved even with the most powerful modern supercomputers. Even if the system is solved exactly, there would be far more information than one would require from using the kinetic model. There are also fluid models such as multi-fluid theory, two-fluid theory, and single-fluid theory. MHD is based on taking this last single-fluid approach, a macroscopic and non-relativistic fluid description, and provides large-scale and low-frequency solutions in magnetic plasmas. MHD can be considered as classical fluid dynamics combined with the additional complication

[2]This Coulomb interaction is a long-range interaction so that one particle interacts simultaneously with many particles.

[3]The fundamental difference between a neutral gas and a plasma should be noted. In a neutral gas the forces are very strong and short-range, and the dynamics of it is dominated by two-body billiard-ball-like collisions. In a plasma state, the inter-particle forces between charged particles are comparatively weak and long-range electromagnetic forces obeying the Coulomb's law.

that the fluid is electrically conducting.

One way to achieve equations of MHD is to begin from first principles with the fundamental microscopic equations (kinetic theory) and then systematically derive the equations of multi-fluid and single-fluid MHD. It is encouraged to present only a brief outline on such mathematical derivations in this section. More detailed descriptions can be found in [35, 38, 43].

Kinetic Theory

In kinetic theory one replaces the real plasma consisting of discrete particles with a smeared-out density distribution function in phase space. It is often convenient that, instead of looking at each individual particle, one adopts a kinetic description with distribution functions for the different species. The Boltzmann equation[4] governs the evolution of such species in the phase space and time. The equation reads

$$\frac{\partial f_\alpha}{\partial t} + \mathbf{w} \cdot f_\alpha(\mathbf{r}, \mathbf{w}, t) + \mathbf{a} \cdot \nabla_w f_\alpha(\mathbf{r}, \mathbf{w}, t) = \Big(\frac{\partial f_\alpha}{\partial t}\Big)_{\text{coll}}, \tag{1.18}$$

where f_α is the distribution function in the phase space for particles of type α, $\mathbf{r}$ is a position, and $\mathbf{w}$ is a velocity vector. The term that appears on the right hand side represents the net variation (gain or loss) of particles of type α per unit volume in phase space and unit time due to collision. The Boltzmann equation together with

[4]The collisionless Boltzmann equation or Vlasov equation can be obtained taking the collision term on the right hand side zero.

the Maxwell equations

$$\nabla \times \mathbf{E} = -\frac{\partial \mathbf{B}}{\partial t}, \tag{1.19}$$

$$\nabla \cdot \mathbf{B} = 0, \tag{1.20}$$

$$\nabla \times \mathbf{B} = \mu \mathbf{j} + \frac{1}{c^2}\frac{\partial \mathbf{E}}{\partial t}, \tag{1.21}$$

$$\nabla \cdot \mathbf{E} = \frac{Q}{\epsilon}, \tag{1.22}$$

form a closed set of system equations. Here $\mathbf{E}$ is the electric field, $\mathbf{B}$ is the magnetic induction, $\mathbf{j}$ is the total electric current density, Q is the total electric charge density, and μ and ϵ are the magnetic permeability and the electric permittivity of the plasma. In this kinetic approach, any macroscopic quantity, such as density, pressure, temperature, can be determined by integrating the expressions involving $f_\alpha(\mathbf{r}, \mathbf{w}, t)$ over velocity space.

There are three important criteria for plasma in this microscopic particle approach. The first is the Debye shielding length λ_D. The potential around a point charge in warm plasma has different Coulomb potential because of the screening by the other charged particles. Only within distances smaller than λ_D the potential follows the Coulomb potential, otherwise it decreases exponentially. This first criterion for a plasma essentially concerns overall charge neutrality, viz., the volume occupied by the plasma must be much larger than a Debye sphere so that there is overall charge neutrality in the plasma. The spatial length scale L of the plasma, thus, must be larger than λ_D. Only over time spans which is much longer than the plasma oscillation[5], the charge neutrality becomes a valid approximation.

[5]Plasma oscillations are high-frequency motions of electrons due to deviations from charge

The second criterion for plasma is that there are sufficiently many particles in the Debye sphere so that there is effective screening and collective behavior. The average inter-particle distance is to be much smaller than λ_D and the average potential energy of a particle to its nearest neighbor should be much smaller than its kinetic energy: the plasma is weakly coupled.

The third criterion concerns damping of plasma oscillations due to collisions of electrons with heavy neutral particles, causing a loss of momentum of electrons. Such plasma oscillations should only be slightly damped by the collisions and the frequency for collisions of electrons with neutrals must be smaller than the electron plasma frequency.

In plasmas the interaction of charged particles with the magnetic field lines plays an important role. For instance, the particles are said to be magnetized in a sense that they are effectively glued to the magnetic field lines: they move in Larmor circles around the magnetic field lines with their Larmor frequency. The Larmor radius (or cyclotron gyration radius) $r_{L,t}$ gives a description of Larmor circles, which is defined by

$$r_{L,t} = \frac{v_t}{\omega_c}, \tag{1.23}$$

where v_t is the particle's thermal velocity and $\omega_c = |q|B/m$ is the angular frequency (Larmor frequency). Here q is a particle's charge and m is its mass, with B a magnitude of the magnetic fields. The light electrons can be easily magnetized (i.e., glued to the field lines), however, the heavy ions could be deviated from the Larmor circles. In that situation one can expect the predictions available from ideal

neutrality in a cold plasma.

MHD are lost due to the heavy ion dynamics. It is also noted that the high-frequency behavior of plasma, such as the electron plasma frequency ($\omega_{p,e}$), Debye length (λ_D), Larmor frequency of electron ($\omega_{c,e}$), Larmor radius of electron ($r_{L,e}$), are dominated by the dynamics of electrons, and the quantities such as $\omega_{p,i}, \omega_{c,i}, r_{L,i}$ characterize the low-frequency behavior and are dominated by the dynamics of ions.

Fluid Description

Should a very detailed description of plasma behavior be provided using the full set of Boltzmann-Maxwell equations (1.18)$\sim$(1.22), solving the set of equations become virtually impossible in any nontrivial situation. The simpler mathematical model, fluid theories, can give a narrower range of applicability for this purpose.

In multi-fluid theory one recognizes that the plasma is composed of different particle species and assumes that each species behaves as a separate fluid. The light electrons and the heavy ions are treated differently in their fluid behaviors. Taking zeroth, first, and second moments of the Boltzmann equation (1.18) give a set of differential equations of mass (continuity equation), conservation of momentum (equation of motion), and conservation of energy (energy equation) in the macroscopic variables. The resulting equations contain information about global quantities related to the particles of type α ranging from high-frequency short-scale dynamics up to low-frequency large-scale fluid dynamics. The microphysics that is available from the distribution functions in the kinetic theory is lost by integrating the Boltzmann equations as applied with three moments. Unfortunately, the result-

ing differential equations are hard to be satisfactory when one realizes that the new set of equations are not in closed form at each stage of the hierarchy of moments.

As a special case of the multi-fluid theory, one can obtain the two-fluid theory equations. These equations consider a fully ionized plasma consisting of electrons and only one type of ions, still containing information of both high-frequency and low-frequency fluid dynamics.

Further simplification can be made if one considers plasma as a conducting fluid without specifying its various individual species, and therefore, use quantities for the plasma as a whole. This approach is called the single-fluid theory. In this theory, each macroscopic variable is formed by adding contributions of the various particle species in the plasma, by using collisional invariance. In contrast with the plasma descriptions so far, this single-fluid theory loses the high-frequency short scale plasma dynamics of the electrons and ions when adopting the single-fluid equations. Since the single-fluid equations for mass, momentum and internal energy still do not form a closed system, they are not very useful yet.

To close the system of equations, therefore, one further needs to take the first order charge moment of the Boltzmann equation and get the *generalized Ohm's law*,

$$\mathbf{E} = \underbrace{-\mathbf{u}\times\mathbf{B}}_{\text{IT}} + \underbrace{\frac{\mathbf{j}}{\sigma}}_{\text{OT}} + \underbrace{\frac{1}{en_e}\mathbf{j}\times\mathbf{B}}_{\text{HT}} \underbrace{-\frac{1}{en_e}\nabla p_e}_{\text{BT}}, \tag{1.24}$$

where one can see the first term is the dynamo term or the induction term (IT), the second is the Ohmic term (OT), the third is the Hall term (HT), and the last is the battery term (BT). One can arrive at the above generalized Ohm's law on assumption that the collisions lead to isotropic distribution functions for both

electrons and ions, and hence one only considers pressure tensor contributions for electrons and ions from the isotropic electron and ion pressures for the battery term. Classical MHD also assumes the equal temperatures of electrons and ions to make physical sense that the temperatures of electrons and ions should be as comparable as a whole plasma temperature.

Finally one can obtain closed form of MHD equations (1.8)$\sim$(1.11) by using the single-fluid equations with combinations[6] of the generalized Ohm's law and the pre-Maxwell equations[7] which are defined as

$$\nabla \times \mathbf{E} = -\frac{\partial \mathbf{B}}{\partial t}, \tag{1.25}$$

$$\nabla \cdot \mathbf{B} = 0, \tag{1.26}$$

$$\nabla \times \mathbf{B} = \mu \mathbf{j} \tag{1.27}$$

$$\nabla \cdot \mathbf{E} = \frac{Q}{\epsilon}. \tag{1.28}$$

Returning attention to the generalized Ohm's law for a moment, one can realize that it is an equation for the electric field involving four terms. Choosing the induction term $-\mathbf{u} \times \mathbf{B}$ as a reference, one can compare the other terms to find out which terms are relatively important. On carrying out some approximations and

[6]For instance, the induction equation (1.10) is a combination of the first equation (Faraday's equation) of the pre-Maxwell equations substituted with the equation of the electric field given by the generalized Ohm's law (1.24). The third equation (Ampére's equation without the displacement current term) of the pre-Maxwell equations can also be solved for $\mathbf{j}$ and substituted in (1.24).

[7]The pre-Maxwell equations are the Maxwell equations that are simplified for non-relativistic MHD version. Hence one can effectively drop the displacement current. This implies that the electromagnetic waves are removed from the consideration for the non-relativistic plasma.

algebras, one can obtain

$$\frac{\mathrm{OT}}{\mathrm{IT}} = 10^{-12} << 1, \quad \frac{\mathrm{HT}}{\mathrm{IT}} = 10^{-1} << 1, \quad \frac{\mathrm{BT}}{\mathrm{IT}} = 10^{-2} << 1. \tag{1.29}$$

This comparison shows that in a typical large-scale low-frequency plasma situation, the induction term is comfortably larger than all the other terms of the generalized Ohm's law (1.24). Excluding all three terms except the induction term, one can achieve a very good approximation of the generalized Ohm's law,

$$\mathbf{E} = -\mathbf{u} \times \mathbf{B}. \tag{1.30}$$

This is the *ideal MHD limit* of the generalized Ohm's law. Retaining the Hall term gives the Ohm's law in the Hall MHD which estimates the effect of the electric field caused by the motion of the electron gas in the presence of the magnetic field,

$$\mathbf{E} = -\mathbf{u} \times \mathbf{B} + \frac{1}{en_e}\mathbf{j} \times \mathbf{B} = -\mathbf{u}_e \times \mathbf{B}. \tag{1.31}$$

Similarly, for the resistive MHD, one gets

$$\mathbf{E} = -\mathbf{u} \times \mathbf{B} + \frac{\mathbf{j}}{\sigma}. \tag{1.32}$$

Let us now discuss, based on the observations made so far, to get conditions of validity for MHD. First note that the approximation of MHD makes physical sense for plasma situations where the spatial and temporal scales of the variations of the fluids and fields are substantially longer than the corresponding scales of the heaviest component of plasmas, viz., ions. One hence arrives at a conclusion for MHD to give the first vital condition of *small gyro-radius*:

$$\frac{r_{L,i}}{L} << 1, \quad \frac{\omega}{\omega_{c,i}} << 1, \tag{1.33}$$

where ω is used for the characteristic frequency of any plasma variation. Also MHD theory assumes sufficient collisions to take place in order to make the distribution functions locally nearly Maxwellian. This is required in that the collision times are short compared to the global time scale of the system defined by e.g., the thermal velocity of the ions $v_{t,i}$ and the size L of the system, viz.,

$$\frac{\tau_{e,i} v_{t,i}}{L} << 1, \quad \frac{\tau_{i,i} v_{t,i}}{L} << 1, \tag{1.34}$$

where averaged collision times $\tau_{i,i} = 1/\bar{\nu}_{i,i}$ and $\tau_{e,i} = 1/\bar{\nu}_{e,i}$ with the average frequency $\bar{\nu}$ of collisions between the charged particles. This is equivalent to having small Knudsen numbers, i.e.,

$$Kn_{e,i} = \frac{\ell_{e,i}}{L} << 1, \quad Kn_{i,i} = \frac{\ell_{i,i}}{L} << 1, \tag{1.35}$$

where $\ell_{\alpha,\beta}$ is the mean free path for particles of type α and β.

It is also required that the ions and electrons have the same temperature, leading to the energy equilibration time $\tau_{eq} \approx (m_i/m_e)\tau_{e,i}$ is much shorter than global time scale $L/v_{t,i}$:

$$\frac{m_i}{m_e}\tau_{e,i} << \frac{L}{v_{t,i}}, \tag{1.36}$$

which yields a second condition for *high collisionality*

$$\frac{m_i}{m_e}\frac{\tau_{e,i} v_{t,i}}{L} << 1. \tag{1.37}$$

The above inequality implies that the thermal conduction of the energy equation can be neglected. The relationships in (1.33) and (1.37) constitute important conditions for MHD to be an accurate representation of plasma phenomenon characterized by a given temporal scale τ and a length scale L.

A third condition of the large magnetic Reynolds number $R_m = Lv/\eta >> 1$ (i.e., *small resistivity* condition for ideal MHD) is additionally required for ideal MHD.

Let us conclude this chapter by making some observations for different regimes of MHD. Firstly, the generalized Ohm's law can be simplified by comparing the various terms with the induction term. The limitations in ideal MHD, therefore, can arise by only keeping the induction term and dropping all other terms. This is the very low-frequency large-scale approximation taken to the extreme. The movement of the plasma affects the temporal evolution of magnetic fields. In ideal MHD, the essential condition for this approximation to make sense is that the length scale of the plasma phenomenon is much longer than the ion Larmor radius.

Secondly, the Hall term becomes important when the heavy ions start to deviate from the magnetic field lines. In other words, dropping this term is still valid if the ions as well as the electrons are both magnetized, i.e., tightly glued to the magnetic field lines. Ideal MHD, therefore, yields a good valid estimate for the plasma fastened to the field lines as a whole. It is easily considered that, for the light electrons, they are effectively magnetized. This is, however, not obvious for the heavy ions. In that situation the Hall terms should be recovered. From the induction equation, one can see that the properties of flux conservation and frozen-in magnetic field lines are the most basic properties of ideal MHD. Due to terms other than the induction term, deviation from flux conservation occurs. Inclusion of the Hall term to account the effect that the ions are no longer to be glued to the magnetic field lines is one source to break the flux conservation. The Hall term ef-

fectively predicts the relationship that the magnetic fields are frozen to the electron flow rather than to the bulk velocity fields. The Hall effect becomes large whenever $\mathbf{j}$ is large, notably in thin current sheets, and the Hall term serves as to decouple ions from electrons.

Thirdly, the resistive terms also cause the deviation from the ideal flux freezing. The magnetic field becomes diffusive when the magnetic field is spatially inhomogeneous at the presence of the resistive terms. This diffusion process takes place on a long time scale, and eventually turns dissipation of magnetic energy into heat.

Lastly, one shall largely forget about the battery term according to the comparison with the induction term. The battery term, in fact, can generate a (weak) electrical field in the direction along the magnetic fields, since the component ∇p_e has components both parallel and normal to the magnetic field lines. Because the induction term, which does not have any component parallel to the field lines, dominates the battery term, the electric field parallel the field lines can be ignored in general.

The next chapter describes the development of a method of multidimensional characteristic analysis in the USM-IEC-SDDA scheme that retains a novel way to treat important physical consideration in multidimensional MHD.

Chapter 2

MATHEMATICAL MODELING OF THE USM SCHEME

Whatever Nature has in store for mankind,

unpleasant as it may be,

men must accept,

for ignorance is never better than knowledge.

Enrico Fermi

In Chapter 2 a mathematical description of the USM scheme is presented. Crockett *et al.* [26] and Gardiner *et al.* [37] seem to have first recognized computational necessary for including multidimensional MHD terms that have been neglected in previous efforts in MHD simulations. The USM scheme, in this aspect, has included such multidimensional requirements in a data reconstruction-evolution step, in which a very versatile and computationally efficient multidimensional characteristic method is used.

The mathematical formulation of the USM-IEC-SDDA scheme can be divided into several steps and will be described throughout the rest of the dissertation. These steps include a data reconstruction step to solve Riemann problem which will be studied in this chapter, an improved electric field construction (IEC) step in Chapter 3, and finally a staggered dissipation-control differencing algorithm (SDDA) step in Chapter 4.

2.1 USM-IEC-SDDA: An Unsplit Staggered Mesh Scheme for MHD

The first step of the USM-IEC-SDDA scheme for multidimensional MHD problems is now discussed in this section. This first step uses a second-order MUSCL-Hancock type TVD algorithm for a data reconstruction. The reconstruction uses the cell-centered data to evaluate boundary extrapolated values that are required to solve Riemann problems at cell interfaces. In this reconstruction step it is important to include terms that reflect multidimensional relationships in MHD governing equations. These relationships have been ignored in many one-dimensional based dimensional splitting type MHD solvers until they were studied by Gardiner *et al.* [37], and Crockett *et al.* [26] very recently. In this dissertation work, similar multidimensional consideration has been achieved by using a method of multidimensional characteristic analysis, rather than using a simple one-dimensional tracing method. The method forms a new approach in a data reconstruction strategy in that aspect. An update of the cell-centered variables is followed using the high-order Godunov fluxes which are solutions to the Riemann problem. The overall procedure of the USM-IEC-SDDA scheme can be broken up into the following steps:

- Quasi-linearization: This replaces the nonlinear system of equations (1.12) with an approximate, quasi-linearized system of equations.

- Evolution in normal directions: Given the cell-centered variables, the quasi-linearized equations are solved to compute the boundary extrapolated Riemann state variables, followed by temporal evolutions by a half time step. A second-order TVD slope limiter is used in constructing a MUSCL-Hancock

type of evolution. Multidimensional MHD terms proportional to $\partial B_x/\partial x$ (or $\partial B_y/\partial y$) are to be included in x-normal directional update (or y-normal directional update).

- Transversal flux contributions: Another set of quasi-linearized equations are solved to account for the contributions from the transversal fluxes. Again, multidimensional terms that are proportional to $\partial B_y/\partial y$ (or $\partial B_x/\partial x$) are included at this y-transversal step (or x-transversal step). The transversal flux updates provide the two Riemann states which are of second-order.

- Riemann problem: Using the updated left and right Riemann states the scheme proceeds to solve the Riemann problem to obtain the second-order fluxes at the cell interfaces.

- Update of cell-centered variables: The unsplit time integrations are performed using the high-order Godunov fluxes to update the cell-centered variables for the next time step.

- IEC algorithm: Using the high-order Godunov fluxes, at the same time, the cell corner (edge in 3D) based electric fields are constructed.

- SDDA scheme: The electric fields are used to evolve the cell face-centered magnetic fields by solving the induction equations. The SDDA scheme will effectively eliminate any possible erroneous growth of the magnetic fields by balancing numerical anti-dissipative terms with added dissipative contributions.

2.2 Quasi-linearization of MHD Equations

The linearization procedure involves obtaining the Roe flux Jacobian matrices $\bar{\mathbf{A}} = (\bar{\mathbf{A}}_x, \bar{\mathbf{A}}_y, \bar{\mathbf{A}}_z)$, where they are quasi-linearized forms of the exact flux Jacobian matrices $\mathbf{A} = (\mathbf{A}_x, \mathbf{A}_y, \mathbf{A}_z)$. The construction of the matrices $\mathbf{A}$ and $\bar{\mathbf{A}}$ can be simplified by writing the governing equations (1.12)$\sim$(1.16) as a linearized system in the primitive variables,

$$\mathbf{V} = (\rho, u, v, w, B_x, B_y, B_z, p)^T. \tag{2.1}$$

Note that there is a simple relationship between the conservative ($\mathbf{U}$) and primitive ($\mathbf{V}$) variables such that

$$d\mathbf{U} = Q d\mathbf{V}, \tag{2.2}$$

where Q is a Jacobian matrix defined as

$$Q = \frac{\partial \mathbf{U}}{\partial \mathbf{V}} = \begin{pmatrix} 1 & 0 & 0 & 0 & 0 & 0 & 0 & 0 \\ u & \rho & 0 & 0 & 0 & 0 & 0 & 0 \\ v & 0 & \rho & 0 & 0 & 0 & 0 & 0 \\ w & 0 & 0 & \rho & 0 & 0 & 0 & 0 \\ 0 & 0 & 0 & 0 & 1 & 0 & 0 & 0 \\ 0 & 0 & 0 & 0 & 0 & 1 & 0 & 0 \\ 0 & 0 & 0 & 0 & 0 & 0 & 1 & 0 \\ \frac{1}{2}U^2 & \rho u & \rho v & \rho w & B_x & B_y & B_z & \frac{-1}{k} \end{pmatrix}, \tag{2.3}$$

where $k = 1 - \gamma$.

In general the equation of state for ideal gases, the range of typical values of $\gamma = c_P/c_V$ is $1 < \gamma < 2$. As a special case, $\gamma = 1$ is used for isothermal gas, for

which the pressure is a function of the density only, and a barotropic equation of state is obtained. For adiabatic process one has $PV^{\gamma} = \text{constant}$, leading to a stiff[1] equation of state for large γ and a soft[2] equation of state for small γ. One can express γ in terms of degrees of freedom d for a given particle, viz., $\gamma = (d+2)/d$. For instances, monatomic ideal gas which has no internal degrees of freedom can have three translational degrees of freedom ($d = 3$), giving $\gamma = 5/3$, diatomic gas which has two additional rotational degrees of freedom ($d = 5$) gives $\gamma = 7/5$, and polyatomic gas allowing three translational and three rotational degrees of freedom ($d = 6$) yields $\gamma = 8/6$. In the macroscopic large-scale fluid description of MHD, $\gamma = 5/3$ is used for many simulation purposes.

Now inverting Q in (2.2), one gets

$$d\mathbf{V} = Q^{-1} d\mathbf{U}, \tag{2.4}$$

where

$$Q^{-1} = \frac{\partial \mathbf{V}}{\partial \mathbf{U}} = \begin{pmatrix} 1 & 0 & 0 & 0 & 0 & 0 & 0 & 0 \\ -\frac{u}{\rho} & \frac{1}{\rho} & 0 & 0 & 0 & 0 & 0 & 0 \\ -\frac{v}{\rho} & 0 & \frac{1}{\rho} & 0 & 0 & 0 & 0 & 0 \\ -\frac{w}{\rho} & 0 & 0 & \frac{1}{\rho} & 0 & 0 & 0 & 0 \\ 0 & 0 & 0 & 0 & 1 & 0 & 0 & 0 \\ 0 & 0 & 0 & 0 & 0 & 1 & 0 & 0 \\ 0 & 0 & 0 & 0 & 0 & 0 & 1 & 0 \\ \frac{-k}{2}U^2 & du & kv & kw & kB_x & kB_y & kB_z & -k \end{pmatrix}. \tag{2.5}$$

[1]Adiabatic compression yields large pressure increase.

[2]Adiabatic compression yields small pressure increase.

The conservative form of the equation (1.12) can then be rewritten in primitive variables,

$$Q\frac{\partial \mathbf{V}}{\partial t} + \frac{\partial \mathbf{F}}{\partial \mathbf{U}}Q\frac{\partial \mathbf{V}}{\partial x} + \frac{\partial \mathbf{G}}{\partial \mathbf{U}}Q\frac{\partial \mathbf{V}}{\partial y} + \frac{\partial \mathbf{H}}{\partial \mathbf{U}}Q\frac{\partial \mathbf{V}}{\partial z} = 0, \tag{2.6}$$

or

$$\frac{\partial \mathbf{V}}{\partial t} + Q^{-1}\frac{\partial \mathbf{F}}{\partial \mathbf{U}}Q\frac{\partial \mathbf{V}}{\partial x} + Q^{-1}\frac{\partial \mathbf{G}}{\partial \mathbf{U}}Q\frac{\partial \mathbf{V}}{\partial y} + Q^{-1}\frac{\partial \mathbf{H}}{\partial \mathbf{U}}Q\frac{\partial \mathbf{V}}{\partial z} = 0. \tag{2.7}$$

This gives rise to the exact flux Jacobian matrices $\mathbf{A}_x, \mathbf{A}_y$, and $\mathbf{A}_z$ defined by,

$$\mathbf{A}_x = Q^{-1}\frac{\partial \mathbf{F}}{\partial \mathbf{U}}Q = Q^{-1}\frac{\partial \mathbf{F}}{\partial \mathbf{V}}, \quad \mathbf{A}_y = Q^{-1}\frac{\partial \mathbf{G}}{\partial \mathbf{U}}Q = Q^{-1}\frac{\partial \mathbf{G}}{\partial \mathbf{V}}, \tag{2.8}$$

$$\mathbf{A}_z = Q^{-1}\frac{\partial \mathbf{H}}{\partial \mathbf{U}}Q = Q^{-1}\frac{\partial \mathbf{H}}{\partial \mathbf{V}}. \tag{2.9}$$

Equation (2.7) can be now written as

$$\frac{\partial \mathbf{V}}{\partial t} + \mathbf{A}_x\frac{\partial \mathbf{V}}{\partial x} + \mathbf{A}_y\frac{\partial \mathbf{V}}{\partial y} + \mathbf{A}_z\frac{\partial \mathbf{V}}{\partial z} = 0. \tag{2.10}$$

On carrying out the algebra one obtains

$$\mathbf{A}_x = \begin{pmatrix} u & \rho & 0 & 0 & 0 & 0 & 0 & 0 \\ 0 & u & 0 & 0 & -\frac{B_x}{\rho} & \frac{B_y}{\rho} & \frac{B_z}{\rho} & \frac{1}{\rho} \\ 0 & 0 & u & 0 & -\frac{B_y}{\rho} & -\frac{B_x}{\rho} & 0 & 0 \\ 0 & 0 & 0 & u & -\frac{B_z}{\rho} & 0 & -\frac{B_x}{\rho} & 0 \\ 0 & 0 & 0 & 0 & 0 & 0 & 0 & 0 \\ 0 & B_y & -B_x & 0 & -v & u & 0 & 0 \\ 0 & B_z & 0 & -B_x & -w & 0 & u & 0 \\ 0 & \gamma p & 0 & 0 & -\mathbf{u}\cdot\mathbf{B} & 0 & 0 & u \end{pmatrix}, \tag{2.11}$$

$$\mathbf{A}_y = \begin{pmatrix} v & 0 & \rho & 0 & 0 & 0 & 0 & 0 \\ 0 & v & 0 & 0 & -\frac{B_y}{\rho} & -\frac{B_x}{\rho} & 0 & 0 \\ 0 & 0 & v & 0 & \frac{B_x}{\rho} & -\frac{B_y}{\rho} & \frac{B_z}{\rho} & \frac{1}{\rho} \\ 0 & 0 & 0 & v & 0 & -\frac{B_z}{\rho} & -\frac{B_y}{\rho} & 0 \\ 0 & -B_y & B_x & 0 & v & -u & 0 & 0 \\ 0 & 0 & 0 & 0 & 0 & 0 & 0 & 0 \\ 0 & 0 & B_z & -B_y & 0 & -w & v & 0 \\ 0 & 0 & \gamma p & 0 & 0 & -\mathbf{u}\cdot\mathbf{B} & 0 & v \end{pmatrix}, \qquad (2.12)$$

$$\mathbf{A}_z = \begin{pmatrix} w & 0 & 0 & \rho & 0 & 0 & 0 & 0 \\ 0 & w & 0 & 0 & -\frac{B_z}{\rho} & 0 & -\frac{B_x}{\rho} & 0 \\ 0 & 0 & w & 0 & 0 & -\frac{B_z}{\rho} & -\frac{B_y}{\rho} & 0 \\ 0 & 0 & 0 & w & \frac{B_x}{\rho} & \frac{B_y}{\rho} & -\frac{B_z}{\rho} & \frac{1}{\rho} \\ 0 & -B_z & 0 & B_x & w & 0 & -u & 0 \\ 0 & 0 & -B_z & B_y & 0 & w & -v & 0 \\ 0 & 0 & 0 & 0 & 0 & 0 & 0 & 0 \\ 0 & 0 & 0 & \gamma p & 0 & 0 & -\mathbf{u}\cdot\mathbf{B} & w \end{pmatrix}. \qquad (2.13)$$

Note that, from relations (1.14)$\sim$(1.16), there are only seven non-trivial equations and one trivial equation for which the time derivative becomes zero. This yields the zeros located in each corresponding row in the above 8×8 matrices (2.11)$\sim$(2.13) as shown. In general the primitive form of the equations can be re-

placed by a quasi-linear system of equations,

$$\frac{\partial \mathbf{V}}{\partial t} + \bar{\mathbf{A}} \cdot \nabla \mathbf{V} = \frac{\partial \mathbf{V}}{\partial t} + (\bar{\mathbf{A}}_x, \bar{\mathbf{A}}_y, \bar{\mathbf{A}}_z) \cdot \nabla \mathbf{V} = 0, \tag{2.14}$$

where $\bar{\mathbf{A}} = \bar{\mathbf{A}}(\mathbf{V}_L, \mathbf{V}_R)$ with two left and right states, $\mathbf{V}_L, \mathbf{V}_R$. The matrix $\bar{\mathbf{A}}$ is subject to satisfy the following properties [20]:

- Hyperbolicity of the system: $\bar{\mathbf{A}}$ has real eigenvalues and linearly independent right eigenvectors, where eigenvalues can be degenerate (non-strict hyperbolicity).
- Consistency with the exact Jacobian: $\bar{\mathbf{A}}(\mathbf{V}_0, \mathbf{V}_0) = \mathbf{A}(\mathbf{V}_0)\Big(\equiv \frac{\partial \mathbf{Flux}}{\partial \mathbf{V}}\Big|_{\mathbf{V}=\mathbf{V}_0}\Big)$, for all $\mathbf{V}_0$.
- Conservation across discontinuities: $\Delta \mathbf{Flux} = \bar{\mathbf{A}} \Delta \mathbf{V} = \bar{\mathbf{A}}(\mathbf{V}_L, \mathbf{V}_R)(\mathbf{V}_R - \mathbf{V}_L)$.

These three properties guarantee that the numerical scheme with these properties is consistent and conservative. In practice the last property is shown to be the most difficult to obtain. The nonlinear behavior of the MHD solutions would depend on the choice of the mean state value $\mathbf{V}_{\text{avg}}$ of the given left and right states, $\mathbf{V}_L$ and $\mathbf{V}_R$. In Brio and Wu [20] the Roe matrix $\bar{\mathbf{A}}$ for the MHD equations has been constructed for a special case $\gamma = 2$ satisfying all three properties. For many practical purposes, a typical choice of $\bar{\mathbf{A}}$ is to use the exact flux Jacobian matrices $\mathbf{A}$ with its analytic entries replaced by their averaged numerical counterparts. (See equation (2.15).)

Many efforts have been made to find a Roe average for the MHD equations. In [69], Powell *et al.* introduced two mean states, but their average is computationally expensive and not always well-behaved. As a result, their average scheme has not found much use. Roe [75] has provided a single linearized Jacobian matrix which satisfies the linearization conditions in that the corresponding averaging in the Euler equation is the $\sqrt{\rho}$ –weighted average for $1/\rho, u, v, w$ and enthalpy h^2.

In fact, if a linearized Jacobian matrix which satisfies Roe's conditions can be constructed, then there exist an infinite number of such linearizations. The existence of a Roe linearization for ideal MHD is thus guaranteed on rather general grounds [45]. Cargo and Gallice [23] also discussed the non-uniqueness of the Roe linearization and studied on the relative efficiency of two different Roe linearizations for ideal MHD.

It has been shown that the arithmetic Roe-averaging derived for $\gamma = 2$ plasmas as in [20] works quite well for other values of γ too [41, 58]. Moreover, Roe and Balsara [76] have shown that the computed flux is not sensitive to the choice of such a mean state $\mathbf{V}_{\text{avg}}$. For these reasons the simplest choice $\mathbf{V}_{\text{avg}} = (\mathbf{V}_L + \mathbf{V}_R)/2$ is adopted for general values of $\gamma \neq 2$, while the Roe-averages [20] is used for $\gamma = 2$.

It is now ready to define the Roe flux Jacobian matrices $\bar{\mathbf{A}} = (\bar{\mathbf{A}}_x, \bar{\mathbf{A}}_y, \bar{\mathbf{A}}_z)$ in terms of $\mathbf{A} = (\mathbf{A}_x, \mathbf{A}_y, \mathbf{A}_z)$ by

$$\bar{\mathbf{A}}(\mathbf{V_L}, \mathbf{V_R}) = \mathbf{A}(\mathbf{V}_{\text{avg}}). \tag{2.15}$$

With this replacement, the quasi-linearized conservative form of the equation (2.10)

in primitive variables can be rewritten as:

$$\frac{\partial \mathbf{V}}{\partial t} + \bar{\mathbf{A}}_x \frac{\partial \mathbf{V}}{\partial x} + \bar{\mathbf{A}}_y \frac{\partial \mathbf{V}}{\partial y} + \bar{\mathbf{A}}_z \frac{\partial \mathbf{V}}{\partial z} = 0. \tag{2.16}$$

2.3 Multidimensional MHD Terms

In one-dimensional MHD the full eight MHD equations can be reduced to seven equations. Should the gradient of the normal magnetic field be zero, one would not need such constant normal field to be evaluated. For multidimensional MHD, however, the terms $\partial B_x/\partial x$ and $\partial B_y/\partial y$ are not zeros in general. They play crucial roles and cannot be ignored. A simple dimensional splitting algorithm based on a truly one-dimensional MHD system of equations does not have these gradient terms and would produce incorrect solutions for this reason.

To treat the gradient terms that arise in multidimensional MHD, the full matrices (2.11)$\sim$(2.13) should be modified. The current work follows an approach similar to Crockett *et al.* [26] for obtaining the multidimensional MHD terms. The idea is to treat the evolution of the normal field B_N separately from the other primitive variables, i.e., for a case with $B_N = B_x$, one can define

$$\bar{\mathbf{V}} = \begin{bmatrix} \hat{\mathbf{V}} \\ \\ B_x \end{bmatrix} \text{ and } \bar{\mathbf{A}}_x = \begin{bmatrix} \hat{\mathbf{A}}_x & \mathbf{A}_{B_x} \\ \\ \mathbf{0} & 0 \end{bmatrix}. \tag{2.17}$$

Here $\hat{\mathbf{V}}$ is a 7×1 vector excluding B_x, $\hat{\mathbf{A}}_x$ is a 7×7 matrix omitting both fifth row and fifth column in the original matrix $\mathbf{A}_x$ (2.11), and $\mathbf{A}_{B_x}$ is a 7×1 vector which is defined by

$$\mathbf{A}_{B_x} = \left[0, -\frac{B_x}{\rho}, -\frac{B_y}{\rho}, -\frac{B_z}{\rho}, -v, -w, -\mathbf{u}\cdot\mathbf{B}\right]^T. \tag{2.18}$$

Similarly, for $B_N = B_y$, $\hat{\mathbf{A}}_y$ can be constructed by omitting both sixth row and column in the original matrix $\mathbf{A}_y$ (2.12), and $\mathbf{A}_{B_y}$ is defined by

$$\mathbf{A}_{B_y} = \left[0, -\frac{B_x}{\rho}, -\frac{B_y}{\rho}, -\frac{B_z}{\rho}, -u, -w, -\mathbf{u}\cdot\mathbf{B}\right]^T. \tag{2.19}$$

The terms $\mathbf{A}_{B_x}$ and $\mathbf{A}_{B_y}$ will be called the multidimensional MHD terms hereafter. Note that the hat ($\hat{}$) notation has been introduced for the reduced system and the bar ($\bar{}$) notation for the re-assembled full system.

2.4 Boundary Extrapolation

The reconstructions of the four multidimensional Riemann states $\mathbf{V}^{n+1/2}_{i,j,N}$, $\mathbf{V}^{n+1/2}_{i,j,S}$, $\mathbf{V}^{n+1/2}_{i,j,E}$ and $\mathbf{V}^{n+1/2}_{i,j,W}$ at cell boundaries, as illustrated in figure 2.1, are achieved to second-order accuracy by using a TVD MUSCL-Hancock approach. In extrapolating the cell center values to the cell boundaries (or interfaces) one can use a TVD slope limiter to the primitive variables.

It is important to discuss the strategy used in this dissertation for employing a TVD limiting at this stage. The limiting is applied to the zone-centered variables, such as density, velocity fields, and pressure, in both normal and transversal directions, while only in *transversal* direction to the cell face-centered magnetic fields. In other words, for the normal field variables, no limiting is used; rather directly use the divergence-free field values at the cell face centers from the previous time step. As a consequence, the C^0 continuity of the normal component of the magnetic field at zone faces are maintained. This recognition is based on numerical consideration to prevent undesired jumps in the normal fields at the cell boundaries.

Indeed, Powell *et al.* [68] have known that if the normal fields have jumps at the cell boundaries, the resultant cell-centered field based MHD formulations using the Riemann solver become ill-defined. They eventually resolved this situation by introducing their 8-wave model with the modified MHD equations.

This situation is completely removed in the current CT-type of scheme using the cell face-centered fields, where, as just mentioned, one can easily meet the continuity consideration of the normal fields at the cell interfaces. More details of such strategy will further be discussed in the next section.

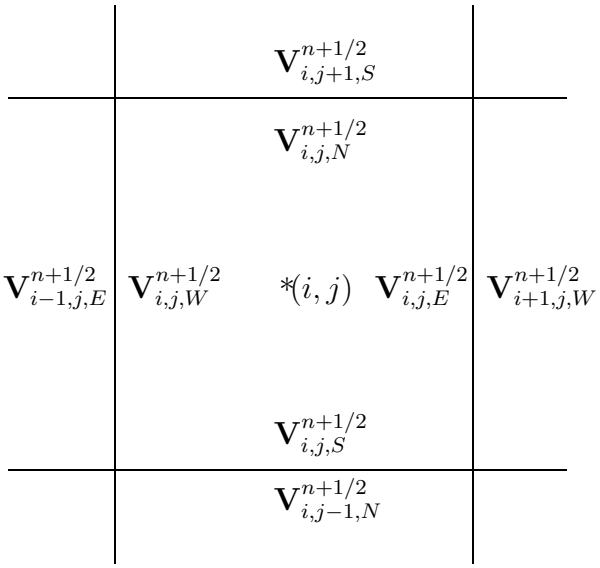

Figure 2.1: The boundary extrapolated values on a 2D cell geometry. The values are subscripted by N, S, E and W accordingly. These are used as the state values for solving the Riemann problems at each cell boundary interface.

Keeping the strategy in mind, only the cell center values of reduced system $\hat{\mathbf{V}}_{i,j}$ are extrapolated to the cell boundaries using a TVD slope limiter. The extrapolated

values are

$$\hat{\mathbf{V}}^{\#}_{i,j,W} = \hat{\mathbf{V}}^{n}_{i,j} - \frac{1}{2}\hat{\Delta}^{n}_{i}; \quad \hat{\mathbf{V}}^{\#}_{i,j,E} = \hat{\mathbf{V}}^{n}_{i,j} + \frac{1}{2}\hat{\Delta}^{n}_{i} \tag{2.20}$$

$$\hat{\mathbf{V}}^{\#}_{i,j,S} = \hat{\mathbf{V}}^{n}_{i,j} - \frac{1}{2}\hat{\Delta}^{n}_{j}; \quad \hat{\mathbf{V}}^{\#}_{i,j,N} = \hat{\mathbf{V}}^{n}_{i,j} + \frac{1}{2}\hat{\Delta}^{n}_{j}, \tag{2.21}$$

where $\hat{\Delta}^{n}_{i}$ and $\hat{\Delta}^{n}_{j}$ are undivided differences using a TVD slope limiter. Given the n-time step's cell-centered variables one obtains

$$\hat{\Delta}^{n}_{i} = \texttt{TVD\_Limiter}\Big(\hat{\mathbf{V}}^{n}_{i+1,j} - \hat{\mathbf{V}}^{n}_{i,j}, \hat{\mathbf{V}}^{n}_{i,j} - \hat{\mathbf{V}}^{n}_{i-1,j}\Big), \tag{2.22}$$

$$\hat{\Delta}^{n}_{j} = \texttt{TVD\_Limiter}\Big(\hat{\mathbf{V}}^{n}_{i,j+1} - \hat{\mathbf{V}}^{n}_{i,j}, \hat{\mathbf{V}}^{n}_{i,j} - \hat{\mathbf{V}}^{n}_{i,j-1}\Big), \tag{2.23}$$

where the choice of the `TVD_Limiter` can be such as MINMOD, MC or van Leer's limiter.

One can also choose a mixed type of limiter as described in [11]. In this choice, one uses a compressible limiter such as MC or van Leer's limiter to produce a more crisp representation for linearly degenerate wave fields. Such wave families include an entropy wave and left- and right-going Alfvén waves. Since much of the variations in these waves consist of the density and the magnetic fields, a compressive limiter can be applied to these two variables. Other variables, the velocity field components and pressure, constitute four genuinely nonlinear wave families (e.g., left- and right-going fast/slow magneto-sonic waves) in MHD. These genuinely nonlinear wave families inherently behave according to their self steepening mechanism and one can simply use a diffusive but robust MINMOD limiter.

2.5 Method of Multidimensional Characteristic Analysis

At each cell, the above extrapolated boundary values (2.20)∼(2.21) are evolved by a half time step, $\Delta t/2$, in the quasi-linearized system (2.16). In the discretized form, the quasi-linearized equation can be written as

$$\mathbf{V}^{n+1/2}_{i,j,E,W} = \mathbf{V}^{\#}_{i,j,E,W} + \frac{\Delta t}{2\Delta x}\mathbf{A}_x(\mathbf{V}^n_{i,j})[\mathbf{V}^{\#}_{i,j,W} - \mathbf{V}^{\#}_{i,j,E}] + \frac{\Delta t}{2\Delta y}\mathbf{A}_y(\mathbf{V}^n_{i,j})[\mathbf{V}^{\#}_{i,j,S} - \mathbf{V}^{\#}_{i,j,N}], \tag{2.24}$$

and

$$\mathbf{V}^{n+1/2}_{i,j,N,S} = \mathbf{V}^{\#}_{i,j,N,S} + \frac{\Delta t}{2\Delta x}\mathbf{A}_x(\mathbf{V}^n_{i,j})[\mathbf{V}^{\#}_{i,j,W} - \mathbf{V}^{\#}_{i,j,E}] + \frac{\Delta t}{2\Delta y}\mathbf{A}_y(\mathbf{V}^n_{i,j})[\mathbf{V}^{\#}_{i,j,S} - \mathbf{V}^{\#}_{i,j,N}]. \tag{2.25}$$

Substitutions of $\mathbf{V}^{\#}_{i,j,E,W}$ and $\mathbf{V}^{\#}_{i,j,N,S}$, as obtained from (2.20) and (2.21), into (2.24) and (2.25) yield

$$\mathbf{V}^{n+1/2}_{i,j,E,W} = \mathbf{V}^n_{i,j} + \frac{1}{2}[\pm\mathbf{I} - \frac{\Delta t}{\Delta x}\mathbf{A}_x(\mathbf{V}^n_{i,j})]\Delta^n_i - \frac{\Delta t}{2\Delta y}\mathbf{A}_y(\mathbf{V}^n_{i,j})\Delta^n_j, \tag{2.26}$$

$$\mathbf{V}^{n+1/2}_{i,j,N,S} = \mathbf{V}^n_{i,j} - \frac{\Delta t}{2\Delta x}\mathbf{A}_x(\mathbf{V}^n_{i,j})\Delta^n_i + \frac{1}{2}[\pm\mathbf{I} - \frac{\Delta t}{\Delta y}\mathbf{A}_y(\mathbf{V}^n_{i,j})]\Delta^n_j, \tag{2.27}$$

where the plus and minus signs correspond to directions of E, N and W, S, respectively. $\mathbf{A}_x(\mathbf{V}^n_{i,j})$ and $\mathbf{A}_x(\mathbf{V}^n_{i,j})$ are the matrices calculated at $\mathbf{V}^n_{i,j}$. At this stage, thus far, the full system of equations in the quasi-linearized form is available.

For the characteristic analysis of (2.26) and (2.27), one can split the evolution procedure into two separate steps, the normal predictor and transversal corrector. To compute the normal predictor step for (2.26), let us return to the reduced system

(2.17),

$$\begin{bmatrix} \hat{\mathbf{V}} \\ B_x \end{bmatrix}_{i,j,E,W}^{n+1/2,\|} = \begin{bmatrix} \hat{\mathbf{V}} \\ B_x \end{bmatrix}_{i,j}^{n} + \frac{1}{2}\left(\pm \begin{bmatrix} \hat{\mathbf{I}} & \mathbf{0} \\ \mathbf{0} & 1 \end{bmatrix} - \frac{\Delta t}{\Delta x} \begin{bmatrix} \hat{\mathbf{A}}_x & \mathbf{A}_{B_x} \\ \mathbf{0} & 0 \end{bmatrix}_{i,j}^{n} \right) \bar{\Delta}_i^n, \quad (2.28)$$

where $\bar{\Delta}_i^n = \left(\hat{\Delta}_i^n, \Delta B_{x,i}^n\right)^T$ and $\Delta B_{x,i}^n = b_{x,i+1/2,j}^n - b_{x,i-1/2,j}^n$. The notations B_τ and b_τ will be reserved for the cell-centered and the cell face-centered magnetic field component respectively, where $\tau = x, y, z$. It is worth mentioning that, with the favor of the staggered mesh CT algorithm, $\Delta B_{x,i}^n$ is constructed in such a way that the numerical divergence is zero with the use of the cell face-centered magnetic fields. In other words, $\Delta B_{x,i}^n$ and $\Delta B_{y,j}^n$ are chosen such that

$$\frac{\Delta B_{x,i}^n}{\Delta x} + \frac{\Delta B_{y,j}^n}{\Delta y} = 0, \quad (2.29)$$

where one can similarly define $\Delta B_{y,j}^n = b_{y,i,j+1/2}^n - b_{y,i,j-1/2}^n$. It should also be noted that no forms of TVD limiting are applied to $\Delta B_{x,i}^n$ and $\Delta B_{y,j}^n$.

Now solving (2.28) is equivalent to considering two subsystems

$$\begin{cases} \hat{\mathbf{V}}_{i,j,E,W}^{n+1/2,\|} = \hat{\mathbf{V}}_{i,j}^n + \frac{1}{2}\left(\pm\hat{\mathbf{I}} - \frac{\Delta t}{\Delta x}\hat{\mathbf{A}}_x\right)_{i,j}^n \hat{\Delta}_i^n - \frac{\Delta t}{2\Delta x}(\mathbf{A}_{B_x})_{i,j}^n \Delta B_{x,i}^n, \\ (B_x)_{i,j,E,W}^{n+1/2,\|} = B_{x,i,j}^n \pm \frac{1}{2}\Delta B_{x,i}^n. \end{cases} \quad (2.30)$$

It can be easily seen that the second equation in (2.30) becomes

$$(B_x)_{i,j,E,W}^{n+1/2,\|} = B_{x,i,j}^n \pm \frac{1}{2}\Delta B_{x,i}^n = b_{x,i+1/2,j}^n, \quad (2.31)$$

when the cell-centered magnetic field is reconstructed as

$$B_{x,i,j}^n = \frac{1}{2}\left(b_{x,i+1/2,j}^n + b_{x,i-1/2,j}^n\right). \quad (2.32)$$

It will be shown in Chapter 5 that the relation in (2.32) is indeed a choice for the USM-IEC-SDDA scheme.

One can now apply the eigenstructure of the one-dimensional based MHD equations (see Appendix A) and use the characteristic tracing for the first two terms in the first equation in (2.30). Following Colella [24] the reference states at the cell left $(i-1/2,j)$ and right $(i+1/2,j)$ are given by

$$\hat{\mathbf{V}}^{\text{Ref}}_{i-1/2,j} = \hat{\mathbf{V}}_{i,j} - \Big[\frac{1}{2} + \min\left(\lambda^{-}_{f,i,j}, 0\right)\frac{\Delta t}{2\Delta x}\Big]\hat{\Delta}^{n}_{i}, \tag{2.33}$$

$$\hat{\mathbf{V}}^{\text{Ref}}_{i+1/2,j} = \hat{\mathbf{V}}_{i,j} + \Big[\frac{1}{2} - \max\left(\lambda^{+}_{f,i,j}, 0\right)\frac{\Delta t}{2\Delta x}\Big]\hat{\Delta}^{n}_{i}, \tag{2.34}$$

where $\lambda^{-}_{f,i,j} = \lambda^{1}_{i,j}$ and $\lambda^{+}_{f,i,j} = \lambda^{7}_{i,j}$ are the smallest and largest eigenvalues, respectively, at (i,j). Then the Riemann states at the cell boundaries are evaluated using the characteristic tracing in the normal direction as

$$\hat{\mathbf{V}}^{n+1/2,\|}_{i,j,W} = \hat{\mathbf{V}}^{\text{Ref}}_{i-1/2,j} + \frac{\Delta t}{2\Delta x}\sum_{k;\lambda^{k}_{i,j}<0}\left(\lambda^{1}_{i,j} - \lambda^{k}_{i,j}\right)\mathbf{r}^{k}_{x,i,j}\mathbf{l}^{k}_{x,i,j}\cdot\hat{\Delta}^{n}_{i}, \tag{2.35}$$

$$\hat{\mathbf{V}}^{n+1/2,\|}_{i,j,E} = \hat{\mathbf{V}}^{\text{Ref}}_{i+1/2,j} + \frac{\Delta t}{2\Delta x}\sum_{k;\lambda^{k}_{i,j}>0}\left(\lambda^{7}_{i,j} - \lambda^{k}_{i,j}\right)\mathbf{r}^{k}_{x,i,j}\mathbf{l}^{k}_{x,i,j}\cdot\hat{\Delta}^{n}_{i}. \tag{2.36}$$

Here $\lambda^{k}_{x,i,j}, \mathbf{r}^{k}_{x,i,j}, \mathbf{l}^{k}_{x,i,j}$ represent the eigenvalue, and the right and left eigenvectors of $\hat{\mathbf{A}}_{x}$, calculated at the corresponding cell center (i,j) in x-direction at time step n. The dot product of the k-th left eigenvector $\mathbf{l}^{k}_{x,i,j}$ with $\hat{\Delta}^{n}_{i}$ reflects the jump in the k-th characteristic variable.

In general, one can obtain two different sets of eigenstructure available for the MHD system. The first is the eigensystem, $\mathbf{r}^{k}, \mathbf{l}^{k}$, which can be derived from the governing equations in the primitive form. The second is its counterpart $\mathbf{R}^{k}, \mathbf{L}^{k}$ from the conservative form. One can effectively convert one from the other by multiplying the Jacobian matrices (2.3) and (2.5):

$$\mathbf{L}^{k} = \mathbf{l}^{k}\frac{\partial \mathbf{V}}{\partial \mathbf{U}}; \quad \mathbf{R}^{k} = \frac{\partial \mathbf{U}}{\partial \mathbf{V}}\mathbf{r}^{k}, \quad k = 1, ..., 7. \tag{2.37}$$

The primitive form eigenstructure should be used in this characteristic tracing method because the method uses the primitive variables. At this stage the normal predictor state variables which include all multidimensional consideration have been obtained. The calculation of the normal predictor of (2.27) in y-direction follows the same procedure, involving only the first and the last terms therein.

The next step is to update the transversal flux contribution to the updated normal predictor state variables. The transversal correction step follows the similar approach using the eigenstructure of the MHD equations. This correction step finalizes the update from the transversal flux contributions, e.g., the last and second terms in (2.26) and (2.27), respectively. In (2.26) the transversal corrector step can be updated as

$$\mathbf{V}_{i,j,E,W}^{n+1/2} = \mathbf{V}_{i,j,E,W}^{n+1/2,\parallel} - \frac{\Delta t}{2\Delta y}\mathbf{A}_y(\mathbf{V}_{i,j}^n)\Delta_j^n. \tag{2.38}$$

Again, this can be written as

$$\begin{bmatrix} \hat{\mathbf{V}} \\ B_y \end{bmatrix}_{i,j,E,W}^{n+1/2} = \begin{bmatrix} \hat{\mathbf{V}} \\ B_y \end{bmatrix}_{i,j,E,W}^{n+1/2,\parallel} - \frac{\Delta t}{2\Delta y}\begin{bmatrix} \hat{\mathbf{A}}_y & \mathbf{A}_{B_y} \\ \mathbf{0} & 0 \end{bmatrix}_{i,j}^{n} \bar{\Delta}_j^n. \tag{2.39}$$

This reduces to solving just one subsystem

$$\hat{\mathbf{V}}_{i,j,E,W}^{n+1/2} = \hat{\mathbf{V}}_{i,j,E,W}^{n+1/2,\parallel} - \frac{\Delta t}{2\Delta y}(\hat{\mathbf{A}}_y)_{i,j}^n\hat{\Delta}_j^n - \frac{\Delta t}{2\Delta y}(\mathbf{A}_{B_y})_{i,j}^n\Delta B_{y,j}^n. \tag{2.40}$$

Using the eigensystem at the cell nodal point (i,j) in y-direction, one gets

$$\hat{\mathbf{V}}_{i,j,E,W}^{n+1/2} = \hat{\mathbf{V}}_{i,j,E,W}^{n+1/2,\parallel} - \frac{\Delta t}{2\Delta y}\sum_{k=1}^{7}\lambda_{y,i,j}^k\mathbf{r}_{y,i,j}^k\mathbf{l}_{y,i,j}^k\cdot\hat{\Delta}_j^n - \frac{\Delta t}{2\Delta y}(\mathbf{A}_{B_y})_{i,j}^n\Delta B_{y,j}^n. \tag{2.41}$$

Similarly, the transversal update for (2.27) is straightforward as

$$\hat{\mathbf{V}}_{i,j,N,S}^{n+1/2} = \hat{\mathbf{V}}_{i,j,N,S}^{n+1/2,\parallel} - \frac{\Delta t}{2\Delta x}\sum_{k=1}^{7}\lambda_{x,i,j}^k\mathbf{r}_{x,i,j}^k\mathbf{l}_{x,i,j}^k\cdot\hat{\Delta}_i^n - \frac{\Delta t}{2\Delta x}(\mathbf{A}_{B_x})_{i,j}^n\Delta B_{x,i}^n. \tag{2.42}$$

So far, all four Riemann states $\mathbf{V}^{n+1/2}_{i,j,N}$,$\mathbf{V}^{n+1/2}_{i,j,S}$,$\mathbf{V}^{n+1/2}_{i,j,E}$ and $\mathbf{V}^{n+1/2}_{i,j,W}$ have been obtained at each cell. At this stage, it should be noticed that upon taking the transversal corrector step as in (2.40), the C^0 continuities of the normal fields at the cell boundaries have been lost. Note that the continuities were imposed, for instance, in the second equation of the normal predictor step (2.30) and (2.31). Maintaining this continuity requirement of the normal fields at the boundaries has been pointed out and recognized as one of the important issues in the MHD Riemann problem [11, 26, 37]. This requirement is essential for physical consistency for solving MHD Riemann problem. Computationally, allowing jumps in the normal fields at the cell boundaries will lead to more diffusive solutions to the Riemann problems from the upwinding procedure in the Riemann solvers. For the transversal components of the magnetic field, however, discontinuities are allowed to mediate the proper upwindings for them. As a last step, therefore, it is encouraged to enforce the normal field components to be continuous at the cell normal boundaries, based on the relationship in equation (2.31). This step thus leads to

$$B^{n+1/2}_{x,i,j,E} = b^n_{x,i+1/2,j}, \quad B^{n+1/2}_{x,i,j,W} = b^n_{x,i-1/2,j}, \tag{2.43}$$

$$B^{n+1/2}_{y,i,j,N} = b^n_{y,i,j+1/2}, \quad B^{n+1/2}_{y,i,j,S} = b^n_{y,i,j-1/2}. \tag{2.44}$$

It is to be realized that the algorithm for the Riemann state data reconstruction completely based on the method of multidimensional characteristic analysis. There have been other approaches to get the second-order accurate approximations of the transversal flux derivatives [24, 26]. For their transversal updating step, they used the normal predictor step values to solve another set of two intermediate Riemann

problems. The resulting interface fluxes are then used to take numerical derivatives, which completes the construction of the second-order Riemann states for evaluating the multidimensional Riemann states.

The current characteristic method, which accommodates the MHD eigenstructure multidimensionally all at the same time, is simpler and computationally cheaper than the approach using the extra Riemann problem to evaluate the transversal fluxes. This approach causes no loss of stability for appropriately chosen Courant numbers. The characteristic method is mathematically consistent with the quasi-linearized system of MHD equations, (2.24) and (2.25).

Another valuable aspect of the current approach can be viewed in that the multidimensional terms $\mathbf{A}_{B_x}$ and $\mathbf{A}_{B_y}$ are included in such a way that they are proportional to $\Delta B_{x,i}/\Delta x$ and $\Delta B_{y,j}/\Delta y$. These derivatives are computed using the cell face-centered magnetic fields that are divergence-free due to the CT-type of USM-IEC-SDDA scheme. This fact implies that the quantities u, v, w, B_z, p are all evolved proportional to the sum $\frac{\Delta B_{x,i}}{\Delta x} + \frac{\Delta B_{y,j}}{\Delta y}$, which is preserved to be zero numerically (see equation (2.29)). As a result, this phenomenon has an important meaning: if perturbations to the divergence $\frac{\Delta B_{x,i}}{\Delta x} + \frac{\Delta B_{y,j}}{\Delta y}$ were introduced, such perturbation would affect the whole behavior of u, v, w, B_z, p. The USM-IEC-SDDA method, taking care of the multidimensional MHD terms properly and efficiently, does not suffer from such phenomenon, and it will be seen clearly in the test suite in Chapter 6.

The use of the transversal flux approach in [26], after updating the characteristic tracing in the normal direction, thus might potentially yield incorrect con-

sequence. Although they used the same multidimensional terms $\mathbf{A}_{B_x}\Delta B^n_{x,i}/\Delta x$ for E, W states in the normal characteristic tracing step and $\mathbf{A}_{B_y}\Delta B^n_{y,j}/\Delta y$ for N, S states in another normal characteristic tracing step, the other set of the multidimensional term $\mathbf{A}_{B_y}\Delta B^n_{y,j}/\Delta y$ for E, W states (and $\mathbf{A}_{B_x}\Delta B^n_{x,i}/\Delta x$ for N, S states) are not included in the transversal direction; rather they just added the numerical derivative of the transversal fluxes. Updating such transversal fluxes would contribute some sort of similar effects of including $\mathbf{A}_{B_y}\Delta B^n_{y,j}/\Delta y$ for obtaining the E, W Riemann states ($\mathbf{A}_{B_x}\Delta B^n_{x,i}/\Delta x$ for N, S states), however, these multidimensional terms are not canceled identically.

2.6 Riemann Problem for USM-IEC-SDDA

Thus far $\mathbf{V}^{n+1/2}_{i,j,N,S,E,W}$ have been obtained and they provide the second-order accurate Riemann states. The second-order Godunov fluxes can now be evaluated from these states by solving Riemann problems (RP for short) at cell interfaces. That is,

$$\mathbf{F}^{*,n+1/2}_{i-1/2,j} = \mathrm{RP}\left(\mathbf{V}^{n+1/2}_{i-1,j,E}, \mathbf{V}^{n+1/2}_{i,j,W}\right), \quad \mathbf{F}^{*,n+1/2}_{i+1/2,j} = \mathrm{RP}\left(\mathbf{V}^{n+1/2}_{i,j,E}, \mathbf{V}^{n+1/2}_{i+1,j,W}\right), \tag{2.45}$$

and

$$\mathbf{G}^{*,n+1/2}_{i,j-1/2} = \mathrm{RP}\left(\mathbf{V}^{n+1/2}_{i,j-1,N}, \mathbf{V}^{n+1/2}_{i,j,S}\right), \quad \mathbf{G}^{*,n+1/2}_{i,j+1/2} = \mathrm{RP}\left(\mathbf{V}^{n+1/2}_{i,j,N}, \mathbf{V}^{n+1/2}_{i,j+1,S}\right). \tag{2.46}$$

A Roe-type Riemann solver is used for solving nonlinear MHD conservative system (see Appendix B).

2.7 Choice of Time Step Using CFL Stability Limit

The choice of the time step Δt follows Colella [24]. In his corner transport upwind (CTU) scheme, the CFL time step limit for multidimensional flow problems is given by

$$\max_{i,j,k}\left(\left|\lambda^k_{x,i,j}\frac{\Delta t}{\Delta x}\right|, \left|\lambda^k_{y,i,j}\frac{\Delta t}{\Delta y}\right|\right) \leq 1, \tag{2.47}$$

where $\lambda^k_{x,i,j}$ and $\lambda^k_{y,i,j}$ are chosen to be the maximum wave mode speeds in the x- and y-directions, respectively. In a practical point of view, this is equivalent to taking a time step Δt as

$$\Delta t = \text{CFL}\,\min\left(\frac{\Delta x}{\left|\lambda^{\max}_{x,i,j}\right|}, \frac{\Delta y}{\left|\lambda^{\max}_{y,i,j}\right|}\right). \tag{2.48}$$

Notice that the above time step limit (2.48) in multidimension is an extention of the one-dimensional Fourier stability limit as found in a simple linear model problem, e.g., an advection equation, discretized in a first-order accurate fashion. For such a simple linear advection equation, an 1D version of (2.48) serves as both necessary and sufficient conditions. However, for multidimensional nonlinear problems, such as the MHD equations, Fourier-type of stability analysis is not available due to the nonlinearity of the system. At least, it is expected that a second-order scheme should maintain the same stability limit as the usual first-order scheme must have. Therefore, one can see the relation in (2.48) from the fact that when the system is fully limited (i.e., Δ^n_i and Δ^n_j become zeros) in the presence of strong jumps, the interface and cell center states are equal, and the scheme yields first-order Godunov solutions in both x- and y-directions. The numerical tests in Chapter 6 have not found any difficulty when the time step is bound according to (2.48). For instance,

a CFL number of 0.5 should work without any loss of stability.

2.8 USM-IEC-SDDA Solution Update

The algorithm now updates the cell-centered conserved variables at time step $n+1$ using an unsplit single step:

$$\mathbf{U}_{i,j}^{n+1} = \mathbf{U}_{i,j}^{n} - \frac{\Delta t}{\Delta x}\left\{\mathbf{F}_{i+1/2,j}^{*,n+1/2} - \mathbf{F}_{i-1/2,j}^{*,n+1/2}\right\} - \frac{\Delta t}{\Delta y}\left\{\mathbf{G}_{i,j+1/2}^{*,n+1/2} - \mathbf{G}_{i,j-1/2}^{*,n+1/2}\right\}. \qquad (2.49)$$

In general, after this update, non-zero divergence magnetic fields are still present at cell centers. In the following two chapters the IEC and SDDA schemes are described to keep the magnetic field variables divergence-free numerically.

Chapter 3

CONSTRUCTION OF ELECTRIC FIELDS

Mathematics is a game

played according to certain simple rules

with meaningless marks on paper.

David Hilbert

A new improved electric field construction (IEC) scheme that demonstrates full directional information is introduced and studied in Chapter 3. The IEC scheme is obtained by using the second-order accurate Godunov fluxes that are available in classical staggered mesh schemes (see [9]). Taylor expansions are applied to the flux components of the magnetic fields (or electric fields by the duality relationship, [9]), at the face centers, to obtain extrapolations to each cell corners, where the electric fields are collocated on a staggered grid. These electric fields are then used in the next SDDA step.

The first part of the chapter will outline several basic algorithms that are used to construct electric fields in the flux-CT formulation, and the later part will discuss the IEC algorithm.

3.1 Classical Staggered Mesh Averaging Scheme

As briefly mentioned in the previous chapter, the CT based scheme requires to evaluate the EMF $\mathbf{E}$ (or simply electric fields). In the algorithm by Balsara & Spicer [9], a novel idea to evaluate the electric fields on a staggered mesh system using high-order Godunov fluxes was proposed. Among many others, one primary advantage in the CT-type schemes is that if a staggered mesh algorithm is adopted for the computation, then the scheme maintains $\nabla \cdot \mathbf{B} = 0$ up to machine round-off error [9, 88]. Balsara & Spicer's original arithmetic averaging scheme for the cell-cornered (cell edge-centered in three-dimension) electric field values, as described in [9], uses the duality relationship between the high-order Godunov flux components for magnetic fields and the electric fields. For instance, the negative of the sixth component of the flux in x (equation (1.14)) and the positive of the fifth component of the flux in y (equation (1.15)) can be interpreted as the z component of the electric fields, E_z, at the cell face centers on the staggered grid. One simple way to construct E_z at each cell corner is then to take a spatial average directly from this duality relationship:

$$\begin{aligned} E^{n+1/2}_{z,i+1/2,j+1/2} &= \frac{1}{4}\Big\{ - F^{*,n+1/2}_{6,i+1/2,j} - F^{*,n+1/2}_{6,i+1/2,j+1} + G^{*,n+1/2}_{5,i,j+1/2} + G^{*,n+1/2}_{5,i+1,j+1/2}\Big\} \\ &= \frac{1}{4}\Big\{E^{*,n+1/2}_{z,i+1/2,j} + E^{*,n+1/2}_{z,i+1/2,j+1} + E^{*,n+1/2}_{z,i,j+1/2} + E^{*,n+1/2}_{z,i+1,j+1/2}\Big\}, \quad (3.1) \end{aligned}$$

where the subscripts 6 and 5 denote the sixth and fifth components in the corresponding flux vectors in equations (1.14)–(1.15), and the superscript $*$ denotes the fluxes (or flux components) directly from the high-order Godunov schemes. The relationship in equation (3.1) will be called as the base electric field construction

scheme for the electric fields hereafter. See figure 3.1 for the staggered mesh arrangement.

The electric field E_z in equation (3.1) can now be used to update the MHD induction equations in a properly discretized manner depending on discretization schemes in different MHD solvers. To discretize the induction equation in a general sense, let us consider integrating the differential form (1.6) over a single three-dimensional control volume of a size $[i-\frac{1}{2}, i+\frac{1}{2}] \times [j-\frac{1}{2}, j+\frac{1}{2}] \times [k-\frac{1}{2}, k+\frac{1}{2}]$ in the Cartesian staggered grid (See figure 3.2). Taking a surface integral yields

$$\frac{\partial}{\partial t} \int \int_{\sum_\ell \mathcal{F}_\ell} \mathbf{B} \cdot \mathbf{n} dA + \int \int_{\sum_\ell \mathcal{F}_\ell} \nabla \times \mathbf{E} \cdot \mathbf{n} dA = 0, \tag{3.2}$$

where $\mathbf{n}$ is a unit normal vector and the summation is taken over the six bounding faces $\mathcal{F}_\ell$, $\ell = 1, \ldots, 6$. Then for each face $\mathcal{F}_\ell$ of the control volume one can use Stokes' Theorem and get

$$\begin{aligned} \frac{\partial}{\partial t} \int \int_{\mathcal{F}_\ell} \mathbf{B} \cdot \mathbf{n} dA &= -\int \int_{\mathcal{F}_\ell} \nabla \times \mathbf{E} \cdot \mathbf{n} dA \\ &= -\int_{\partial \mathcal{F}_\ell} \mathbf{E} \cdot \mathbf{T} dl \end{aligned} \tag{3.3}$$

where $\mathbf{T}$ is a unit tangential vector and dl is a line element. Considering the associated normal (denoted by η) and tangential (denoted by τ) components of the magnetic and electric fields for each face $\mathcal{F}_\ell$, one can let

$$b_\eta^n = \frac{1}{\mu(\mathcal{F}_\ell)} \int \int_{\mathcal{F}_\ell} B_\eta dA, \tag{3.4}$$

$$E_\tau^{n+1/2} = \frac{1}{\mu(\partial \mathcal{F}_\ell)} \int_{\partial \mathcal{F}_\ell} E_\tau dl, \tag{3.5}$$

where μ is a measure and $\eta, \tau = x, y, z$. Notice that in the CT formulation the magnetic field components b_η^n are the area-averaged values at cell faces, whereas the

rest of the conservative variables such as density, momentum, and energy are the volume-averaged quantities.

Using (3.4) and (3.5), one can rewrite the above equation (3.3) at each control volume's face in component-wise form as

$$\begin{aligned}
&\Delta y \Delta z \frac{\partial}{\partial t} b^n_{x,i\pm\frac{1}{2},j,k} \\
&= -\{\Delta z(E^{n+1/2}_{z,i\pm\frac{1}{2},j+\frac{1}{2},k} - E^{n+1/2}_{z,i\pm\frac{1}{2},j-\frac{1}{2},k}) + \Delta y(E^{n+1/2}_{y,i\pm\frac{1}{2},j,k-\frac{1}{2}} - E^{n+1/2}_{y,i\pm\frac{1}{2},j,k+\frac{1}{2}})\}, \quad (3.6) \\
&\Delta x \Delta z \frac{\partial}{\partial t} b^n_{y,i,j\pm\frac{1}{2},k} \\
&= -\{\Delta z(E^{n+1/2}_{z,i-\frac{1}{2},j\pm\frac{1}{2},k} - E^{n+1/2}_{z,i+\frac{1}{2},j\pm\frac{1}{2},k}) + \Delta x(E^{n+1/2}_{x,i,j\pm\frac{1}{2},k+\frac{1}{2}} - E^{n+1/2}_{x,i,j\pm\frac{1}{2},k-\frac{1}{2}})\}, \quad (3.7) \\
&\Delta x \Delta y \frac{\partial}{\partial t} b^n_{z,i,j,k\pm\frac{1}{2}} \\
&= -\{\Delta x(E^{n+1/2}_{x,i,j-\frac{1}{2},k\pm\frac{1}{2}} - E^{n+1/2}_{x,i,j+\frac{1}{2},k\pm\frac{1}{2}}) + \Delta y(E^{n+1/2}_{y,i+\frac{1}{2},j,k\pm\frac{1}{2}} - E^{n+1/2}_{y,i-\frac{1}{2},j,k\pm\frac{1}{2}})\}. \quad (3.8)
\end{aligned}$$

Note that in the above equations the lower case b denotes the magnetic fields at cell face centers, whereas the upper case B represents the cell-centered volumetric field variables as mentioned earlier.

Further by discretizing the temporal derivative terms and dividing out $\Delta x, \Delta y$ and Δz, one can obtain a set of discrete forms of the induction equations on the staggered grid. For instance, in two-dimension, one can get the original Yee's method (1966) [94] by applying the forward temporal discretization:

$$\begin{aligned}
b^{n+1}_{x,i+1/2,j} &= b^n_{x,i+1/2,j} - \frac{\Delta t}{\Delta y}\Big\{E^{n+1/2}_{z,i+1/2,j+1/2} - E^{n+1/2}_{z,i+1/2,j-1/2}\Big\}, \quad (3.9) \\
b^{n+1}_{y,i,j+1/2} &= b^n_{y,i,j+1/2} - \frac{\Delta t}{\Delta x}\Big\{-E^{n+1/2}_{z,i+1/2,j+1/2} + E^{n+1/2}_{z,i-1/2,j+1/2}\Big\}. \quad (3.10)
\end{aligned}$$

Many other CT schemes [9–11,37] fundamentally take the above discretization

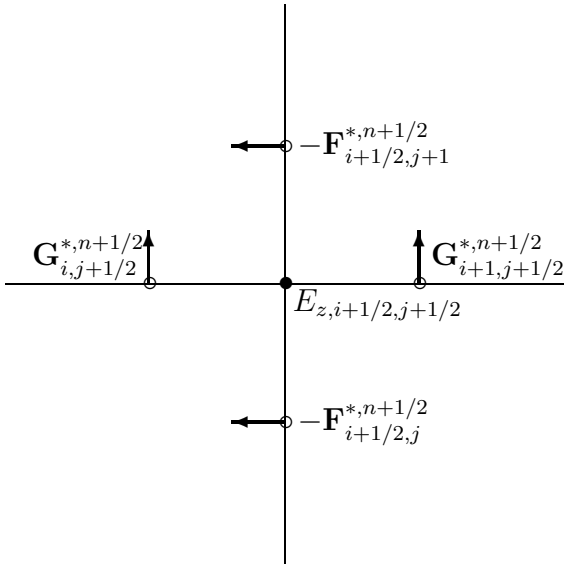

Figure 3.1: The 2D geometry of the staggered mesh in the flux-CT finite volume scheme. In the staggered mesh, the upwinded numerical fluxes $\mathbf{F}^*$ and $\mathbf{G}^*$ are collocated at the centers of cell interfaces and the electric fields $\mathbf{E}$ (only E_z is shown here for 2D) are collocated at the cell corners. The upwinded fluxes $\mathbf{F}^*$ and $\mathbf{G}^*$ from the high-order Godunov scheme are averaged and used to calculate the cell-cornered electric field E_z. See also next figure.

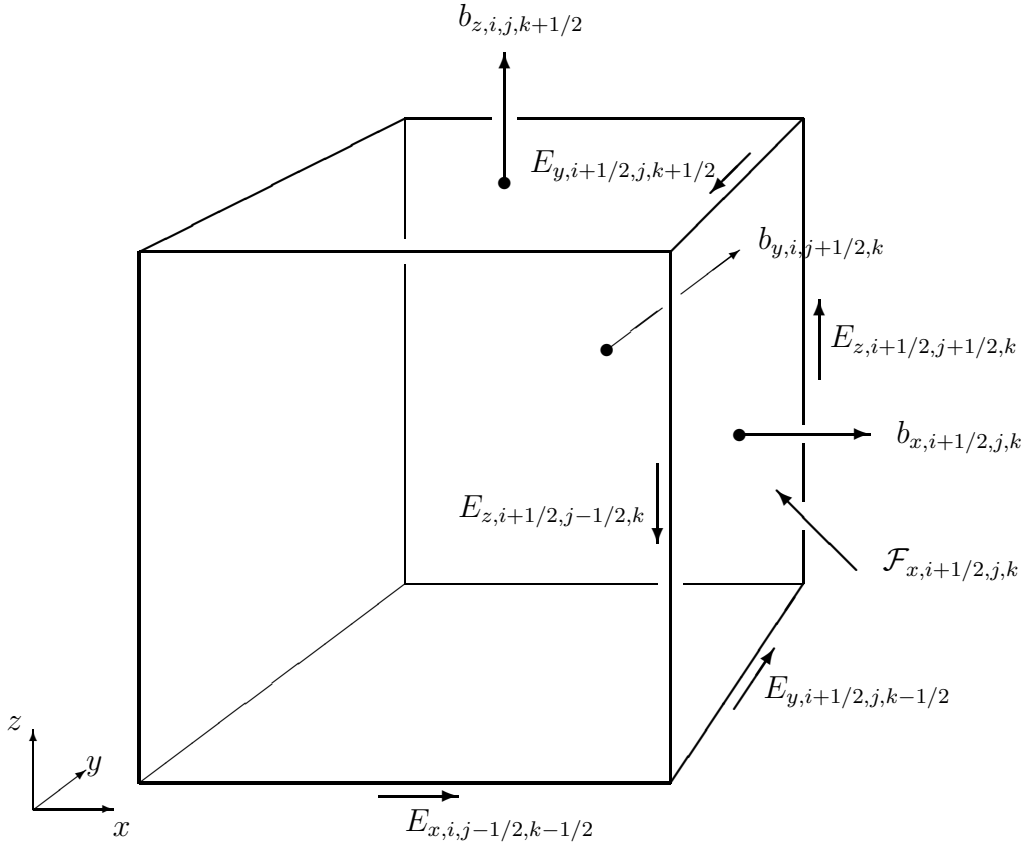

Figure 3.2: A 3D control volume on the staggered grid with the cell center at (i, j, k). The magnetic fields are collocated at the cell face centers and the electric fields at the cell edge centers. The line integral of the electric fields $\int_{\partial \mathcal{F}_n} \mathbf{E} \cdot \mathbf{T} dl$ in equation (3.3) along the four edges of the face $\mathcal{F}_{x,i+1/2,j,k}$ gives rise to the negative of the rate of change of the magnetic field flux in x-direction through the area enclosed by the four edges (e.g., the area of $\mathcal{F}_{x,i+1/2,j,k}$).

scheme. On the staggered grid, the numerical divergence of $\mathbf{B}$ is defined by

$$(\nabla \cdot \mathbf{B})_{i,j}^{n+1} = \frac{b_{x,i+1/2,j}^{n+1} - b_{x,i-1/2,j}^{n+1}}{\Delta x} + \frac{b_{y,i,j+1/2}^{n+1} - b_{y,i,j-1/2}^{n+1}}{\Delta y} \tag{3.11}$$

and it remains zero to the accuracy of machine round-off errors, provided that $(\nabla \cdot \mathbf{B})_{i,j}^{n} = 0$. See a proof in the next section.

3.2 Numerical Proof of Divergence-Free Constraint

It has been seen already in equation (1.7) that the divergence-free property of the magnetic fields can be obtained analytically by taking the divergence of the induction equation. This analytical proof, however, does not guarantee that the same nice property also holds in a discrete space. Thus it is encouraged to present a proof that shows the divergence-free constraint also holds in a discrete sense for the method described in the previous section.

Let us assume that $(\nabla \cdot \mathbf{B})_{(i,j)}^{n} = 0$ initially at time step n. Then

$$\begin{aligned}
(\nabla \cdot \mathbf{B})_{i,j}^{n+1} &= \frac{b_{x,i+1/2,j}^{n+1} - b_{x,i-1/2,j}^{n+1}}{\Delta x} + \frac{b_{y,i,j+1/2}^{n+1} - b_{y,i,j-1/2}^{n+1}}{\Delta y} \\
&= \frac{1}{\Delta x}\Big\{ b_{x,i+1/2,j}^{n} - \frac{\Delta t}{\Delta y}(E_{z,i+1/2,j+1/2}^{n+1/2} - E_{z,i+1/2,j-1/2}^{n+1/2}) \\
&\qquad - b_{x,i-1/2,j}^{n} + \frac{\Delta t}{\Delta y}(E_{z,i-1/2,j+1/2}^{n+1/2} - E_{z,i-1/2,j-1/2}^{n+1/2}) \Big\} \\
&\quad + \frac{1}{\Delta y}\Big\{ b_{y,i,j+1/2}^{n} - \frac{\Delta t}{\Delta x}(-E_{z,i+1/2,j+1/2}^{n+1/2} + E_{z,i-1/2,j+1/2}^{n+1/2}) \\
&\qquad - b_{y,i,j-1/2}^{n} + \frac{\Delta t}{\Delta x}(-E_{z,i+1/2,j-1/2}^{n+1/2} + E_{z,i-1/2,j-1/2}^{n+1/2}) \Big\} \\
&= \frac{b_{x,i+1/2,j}^{n} - b_{x,i-1/2,j}^{n}}{\Delta x} + \frac{b_{y,i,j+1/2}^{n} - b_{y,i,j-1/2}^{n}}{\Delta y} \\
&\quad + \frac{\Delta t}{\Delta x \Delta y}\Big\{ -E_{z,i+1/2,j+1/2}^{n+1/2} + E_{z,i+1/2,j-1/2}^{n+1/2} \\
&\qquad + E_{z,i-1/2,j+1/2}^{n+1/2} - E_{z,i-1/2,j-1/2}^{n+1/2}
\end{aligned}$$

$$
\begin{aligned}
&+E^{n+1/2}_{z,i+1/2,j+1/2} - E^{n+1/2}_{z,i-1/2,j+1/2} \\
&-E^{n+1/2}_{z,i+1/2,j-1/2} + E^{n+1/2}_{z,i-1/2,j-1/2}\Big\} \\
&= (\nabla \cdot \mathbf{B})^n_{i,j} \\
&= 0. \qquad (3.12)
\end{aligned}
$$

Notice that this divergence-free property is satisfied locally at each control volume, and thus one does not require any extra numerical treatment on AMR block structures. The next chapter will introduce a new efficient algorithm that also controls numerical dissipations in the induction equation. This new numerical dissipation algorithm on the staggered grid will also satisfy the divergence-free constraint locally and a new proof to that will also be presented.

3.3 Alternative Averaging Schemes

The *modified flux*-CT scheme by Balsara [11] evaluate the electric field directly at the nodes (e.g., cell corners in 2D, and cell edge centers in 3D) on the staggered grid. That is, in two-dimension, four Riemann problems are solved to obtain the fluxes at the cell corners and the resulting four flux components are used to construct the cell-cornered electric field directly. This method replaces the spatial averaging scheme in equation (3.1) with the direct construction scheme. To solve four Riemann problems at these nodal points one first needs to reconstruct four Riemann state variables from the cell center values. These procedures are apparently expensive computationally.

More recently, Gardiner *et al.* [37] introduced a systematic approach to con-

structing a two-dimensional flux-CT algorithm which is consistent with the underlying plane-parallel, grid-aligned integration algorithm. They addressed the potential inconsistency that can arise from the simple spatial arithmetic averaging scheme of equation (3.1) for the plane-parallel, grid-aligned flows. Such flows are, for instance, one-dimensional flow problems that are solved on a two-dimensional grid, in which the flow direction is parallel to one of the coordinate axes. Their approach is to add extra terms in the base electric fields construction scheme (e.g., equation (3.1)) in such a way that the electric fields at the cell corners obey the planar symmetry in the plane-parallel, grid-aligned flows. In other words, assuming $\frac{\partial}{\partial x} = 0$ so that the flow direction is fixed parallel to y axis, their construction scheme yields $E_{z,i+1/2,j+1/2} = E_{z,i,j+1/2}$. As yet their scheme is consistent with the underlying flows, it requires more computational efforts than the IEC update scheme does. In their CT algorithm, a two-step procedure is used to update solutions from nth to $(n+1)$th time step. From a practical point of view, both the Riemann problem and the electric field construction should be solved twice for each, and it is debatable if this more computationally expensive CT scheme is worth for the accuracy for which they claim.

3.4 IEC Algorithm using Directional Derivatives in Electric Fields Construction

A new electric field construction scheme is now described in this section. The scheme uses first- and second-order directional derivatives evaluated at cell face

centers to extrapolate the electric fields to cell corners. The cell face-centered electric fields are available from corresponding components of the high-order Godunov fluxes that are solutions to the Riemann problem. The superscript $*$ will be used in a consistent way as mentioned in the previous section.

Let us start with Taylor series expansions of the cell-cornered electric field value $E^{n+1/2}_{z,i+1/2,j+1/2}$ in all directions. Then one can obtain

$$\begin{cases} E^{n+1/2}_{z,i+1/2,j+1/2} = E^{*,n+1/2}_{z,i+1/2,j} + \frac{\Delta y}{2}\frac{\partial E^{*,n+1/2}_{z,i+1/2,j}}{\partial y} + \frac{\Delta y^2}{8}\frac{\partial^2 E^{*,n+1/2}_{z,i+1/2,j}}{\partial y^2} + \mathcal{O}(\Delta y^3) \\ E^{n+1/2}_{z,i+1/2,j+1/2} = E^{*,n+1/2}_{z,i+1/2,j+1} - \frac{\Delta y}{2}\frac{\partial E^{*,n+1/2}_{z,i+1/2,j+1}}{\partial y} + \frac{\Delta y^2}{8}\frac{\partial^2 E^{*,n+1/2}_{z,i+1/2,j+1}}{\partial y^2} + \mathcal{O}(\Delta y^3), \\ E^{n+1/2}_{z,i+1/2,j+1/2} = E^{*,n+1/2}_{z,i,j+1/2} + \frac{\Delta x}{2}\frac{\partial E^{*,n+1/2}_{z,i,j+1/2}}{\partial x} + \frac{\Delta x^2}{8}\frac{\partial^2 E^{*,n+1/2}_{z,i,j+1/2}}{\partial x^2} + \mathcal{O}(\Delta x^3), \\ E^{n+1/2}_{z,i+1/2,j+1/2} = E^{*,n+1/2}_{z,i+1,j+1/2} - \frac{\Delta x}{2}\frac{\partial E^{*,n+1/2}_{z,i+1,j+1/2}}{\partial x} + \frac{\Delta x^2}{8}\frac{\partial^2 E^{*,n+1/2}_{z,i+1,j+1/2}}{\partial x^2} + \mathcal{O}(\Delta x^3). \end{cases} \tag{3.13}$$

Taking an arithmetic average of these four Taylor expansions gives

$$\begin{aligned} & E^{n+1/2}_{z,i+1/2,j+1/2} \\ &= \frac{1}{4}\Big\{ E^{*,n+1/2}_{z,i+1/2,j} + \frac{\Delta y}{2}\left(\partial E^{*,n+1/2}_{z,i+1/2,j}\big/\partial y\right) + \frac{\Delta y^2}{8}\left(\partial^2 E^{*,n+1/2}_{z,i+1/2,j}\big/\partial y^2\right) \\ &\quad + E^{*,n+1/2}_{z,i+1/2,j+1} - \frac{\Delta y}{2}\left(\partial E^{*,n+1/2}_{z,i+1/2,j+1}\big/\partial y\right) + \frac{\Delta y^2}{8}\left(\partial^2 E^{*,n+1/2}_{z,i+1/2,j+1}\big/\partial y^2\right) \\ &\quad + E^{*,n+1/2}_{z,i,j+1/2} + \frac{\Delta x}{2}\left(\partial E^{*,n+1/2}_{z,i,j+1/2}\big/\partial x\right) + \frac{\Delta x^2}{8}\left(\partial^2 E^{*,n+1/2}_{z,i,j+1/2}\big/\partial x^2\right) \\ &\quad + E^{*,n+1/2}_{z,i+1,j+1/2} - \frac{\Delta x}{2}\left(\partial E^{*,n+1/2}_{z,i+1,j+1/2}\big/\partial x\right) + \frac{\Delta x^2}{8}\left(\partial^2 E^{*,n+1/2}_{z,i+1,j+1/2}\big/\partial x^2\right)\Big\}. \end{aligned} \tag{3.14}$$

Gardiner *et al.* [37] proposed a similar (but different) approach in terms of adding extra derivative terms in their electric field construction. Their construction scheme includes only up to the first derivative terms which are evaluated at off-nodal points. For instance,

$$E^{n+1/2}_{z,i+1/2,j+1/2} = E^{*,n+1/2}_{z,i+1/2,j} + \frac{\Delta y}{2}\left(\partial E^{*,n+1/2}_{z,i+1/2,j+1/4}\big/\partial y\right), \tag{3.15}$$

where the derivative is evaluated at $(i+\frac{1}{2}, j+\frac{1}{4})$, instead of at $(i+\frac{1}{2}, j)$. This quarter off-nodal point was chosen in order to reduce their scheme to a base integration scheme for the grid-aligned, plane-parallel flows as they claim, yet it is obvious that the choice is not a correct nodal point for Taylor expansion.

The inclusion of the directional derivative terms at this stage has several important aspects. In the CT-type of schemes one evolves the magnetic fields (surface variables) by solving the discretized induction equations (e.g., equations (3.9)$\sim$(3.10)), whereas other conservative (volumetric) variables such as density, momentum, and energy are updated by solving the underlying high-order Godunov scheme. These two sets of variables are updated differently. This does not mean that the surface and volumetric variables form two decoupled systems; rather, they are strongly coupled via momentum, energy, and induction equations. Therefore, to accomplish overall accurate solutions in MHD one needs to obtain high-order accuracy for both the surface and volumetric variables. The derivative terms in equation (3.14) clearly provide such added accuracy as compared with the base construction algorithm (See equation (3.1)).

The new algorithm shown in (3.14), which will be called an *improved electric field construction* (IEC) algorithm, is ideally a third-order in space for smooth profiles of the electric fields. Note that the base construction scheme only incorporates the smooth part of the electric fields by taking the simple arithmetic averages. This situation is improved in the IEC algorithm in such a way that the first derivative terms reflect correct spatial changes from the cell face centers to the cell corners. Furthermore, the second derivative terms will add proper amounts of dissipations

to the extrapolated cell-cornered electric fields. It is well known that insufficient dissipations will cause spurious oscillations near discontinuities in solutions.

To implement the IEC algorithm numerically it is needed to discretize the derivative terms therein. Two different discretization methods, a central differencing and an upwinded differencing methods, can be proposed and they will be described in the next two sections.

3.5 Central Differencing

A second-order central differencing can be used for both first and second derivative terms in the IEC algorithm. At x interfaces (e.g., at $i \pm \frac{1}{2}$), one can dicretize $\partial E^{*,n+1/2}_{z,i\pm1/2,j}\big/\partial y$ and $\partial^2 E^{*,n+1/2}_{z,i\pm1/2,j}\big/\partial y^2$ as

$$\frac{\partial E^{*,n+1/2}_{z,i\pm1/2,j}}{\partial y} = \frac{E^{*,n+1/2}_{z,i\pm1/2,j+1} - E^{*,n+1/2}_{z,i\pm1/2,j-1}}{2\Delta y}, \tag{3.16}$$

and

$$\frac{\partial^2 E^{*,n+1/2}_{z,i\pm1/2,j}}{\partial y^2} = \frac{E^{*,n+1/2}_{z,i\pm1/2,j+1} - 2E^{*,n+1/2}_{z,i\pm1/2,j} + E^{*,n+1/2}_{z,i\pm1/2,j-1}}{\Delta y^2}. \tag{3.17}$$

Similarly, discretizations at y interfaces (e.g., at $j \pm \frac{1}{2}$) are

$$\frac{\partial E^{*,n+1/2}_{z,i,j\pm1/2}}{\partial x} = \frac{E^{*,n+1/2}_{z,i+1,j\pm1/2} - E^{*,n+1/2}_{z,i-1,j\pm1/2}}{2\Delta x}, \tag{3.18}$$

and

$$\frac{\partial^2 E^{*,n+1/2}_{z,i,j\pm1/2}}{\partial x^2} = \frac{E^{*,n+1/2}_{z,i+1,j\pm1/2} - 2E^{*,n+1/2}_{z,i,j\pm1/2} + E^{*,n+1/2}_{z,i-1,j\pm1/2}}{\Delta x^2}. \tag{3.19}$$

3.6 Upwinded Differencing

A finite differencing in an upwinding fashion can also be used for the derivative terms. In fact, Gardiner *et al.* [37] adopted an upwinded differencing scheme for the first-order derivative terms according to the tangential contact mode at each interface. For instance, at x interface one can have

$$\frac{\partial E^{*,n+1/2}_{z,i\pm1/2,j}}{\partial y} = \begin{cases} \frac{1}{\Delta y}\left(E^{*,n+1/2}_{z,i\pm1/2,j} - E^{*,n+1/2}_{z,i\pm1/2,j-1}\right) & \text{if } \frac{v_{i,j}+v_{i\pm1,j}}{2} > \epsilon, \\ \frac{1}{\Delta y}\left(E^{*,n+1/2}_{z,i\pm1/2,j+1} - E^{*,n+1/2}_{z,i\pm1/2,j}\right) & \text{if } \frac{v_{i,j}+v_{i\pm1,j}}{2} < -\epsilon, \\ \frac{1}{2\Delta y}\left(E^{*,n+1/2}_{z,i\pm1/2,j+1} - E^{*,n+1/2}_{z,i\pm1/2,j-1}\right) & \text{otherwise,} \end{cases} \tag{3.20}$$

where ϵ is an arbitrary small positive number. Similarly for the second derivative, one can get

$$\frac{\partial^2 E^{*,n+1/2}_{z,i\pm1/2,j}}{\partial y^2} = \begin{cases} \frac{1}{\Delta y^2}\left(E^{*,n+1/2}_{z,i\pm1/2,j} - 2E^{*,n+1/2}_{z,i\pm1/2,j-1} + E^{*,n+1/2}_{z,i\pm1/2,j-2}\right) & \text{if } \frac{v_{i,j}+v_{i\pm1,j}}{2} > \epsilon, \\ \frac{1}{\Delta y^2}\left(E^{*,n+1/2}_{z,i\pm1/2,j+2} - 2E^{*,n+1/2}_{z,i\pm1/2,j+1} + E^{*,n+1/2}_{z,i\pm1/2,j}\right) & \text{if } \frac{v_{i,j}+v_{i\pm1,j}}{2} < -\epsilon, \\ \frac{1}{\Delta y^2}\left(E^{*,n+1/2}_{z,i\pm1/2,j+1} - 2E^{*,n+1/2}_{z,i\pm1/2,j} + E^{*,n+1/2}_{z,i\pm1/2,j-1}\right) & \text{otherwise.} \end{cases} \tag{3.21}$$

In the same fashion, upwinding at y interface is selected according to the velocity u in x-direction,

$$\frac{\partial E^{*,n+1/2}_{z,i,j\pm1/2}}{\partial x} = \begin{cases} \frac{1}{\Delta x}\left(E^{*,n+1/2}_{z,i,j\pm1/2} - E^{*,n+1/2}_{z,i-1,j\pm1/2}\right) & \text{if } \frac{u_{i,j}+u_{i,j\pm1}}{2} > \epsilon, \\ \frac{1}{\Delta x}\left(E^{*,n+1/2}_{z,i+1,j\pm1/2} - E^{*,n+1/2}_{z,i,j\pm1/2}\right) & \text{if } \frac{u_{i,j}+u_{i,j\pm1}}{2} < -\epsilon, \\ \frac{1}{2\Delta x}\left(E^{*,n+1/2}_{z,i+1,j\pm1/2} - E^{*,n+1/2}_{z,i-1,j\pm1/2}\right) & \text{otherwise.} \end{cases} \tag{3.22}$$

Similarly for the second derivative, one obtains

$$\frac{\partial^2 E^{*,n+1/2}_{z,i,j\pm1/2}}{\partial x^2} = \begin{cases} \frac{1}{\Delta x^2}\left(E^{*,n+1/2}_{z,i,j\pm1/2} - 2E^{*,n+1/2}_{z,i-1,j\pm1/2} + E^{*,n+1/2}_{z,i-2,j\pm1/2}\right) & \text{if } \frac{u_{i,j}+u_{i,j\pm1}}{2} > \epsilon, \\ \frac{1}{\Delta x^2}\left(E^{*,n+1/2}_{z,i+2,j\pm1/2} - 2E^{*,n+1/2}_{z,i+1,j\pm1/2} + E^{*,n+1/2}_{z,i,j\pm1/2}\right) & \text{if } \frac{u_{i,j}+u_{i,j\pm1}}{2} < -\epsilon, \\ \frac{1}{\Delta x^2}\left(E^{*,n+1/2}_{z,i+1,j\pm1/2} - 2E^{*,n+1/2}_{z,i,j\pm1/2} + E^{*,n+1/2}_{z,i-1,j\pm1/2}\right) & \text{otherwise.} \end{cases} \tag{3.23}$$

One can immediately notice here that the upwinded differencing requires wider stencil range (one more stencil point for each x and y-direction) than the central differencing does. This means that the bigger size of guard cells (equivalently, ghost cells) should be used for the upwinded differencing scheme when the scheme is solved on parallel and/or AMR grid structures. In parallel, AMR computation, the need for such guard cells is crucial to achieve proper boundary condition, for which the correct boundary information is stored on the guard cells via inter-processor communications. The guard cell exchange between processors, hence, becomes very expensive when a computer simulation is solved on extensively parallel computer architectures. In AMR block structures, one needs to pay an expensive price by having extra guard cells when the level of refinement becomes progressively increased. This parallel, AMR computing issue will be addressed in more details in Chapter 5.

As yet Gardiner *et al.* [37] proposed that the upwinded differencing at each interface may work well to lead a stable, non-oscillatory integration algorithm, this research work has not found any improvement in solutions of using the upwinding over the central differencing. It is believed that this is because the electric field is not the quantity that is propagated according to the contact mode in the characteristic curves. In general, an upwinding strategy is useful when one tries to obtain the direction of the propagation of information in a flow field along the characteristic curves. Evidently, the electric fields in ideal MHD, $\mathbf{E} = -\mathbf{u} \times \mathbf{B}$, do not propagate along the direction parallel to the velocity fields, nor to the magnetic fields. Rather, they are in direction perpendicular to both the velocity and the magnetic fields. For this physical consideration as well as the computational parallel efficiency just

mentioned above, the IEC algorithm will choose the central differencing strategy for discretizing the derivative terms.

The electric fields constructed in this chapter will be applied to the induction equations (3.9) $\sim$ (3.10) for temporal evolutions of the divergence-free magnetic fields. Before further proceeding to solve the induction equations, the next chapter will be devoted to introduce and develop a new staggered dissipation-control differencing algorithm (SDDA) that can be derived from a set of modified equations of the induction equations.

Chapter 4

A STAGGERED DISSIPATION-CONTROL DIFFERENCING ALGORITHM (SDDA)

One does not,

by knowing all the physical laws as we know them today,

immediately obtain an understanding of anything much.

Richard Feynman

In Chapter 4, a new staggered dissipation-control differencing algorithm (SDDA) is introduced and developed. The SDDA can be deduced from observations of modified equations for the induction equations. The main advantage of the SDDA is that the method can handle numerical anti-dissipations to prevent a secular growth in the magnetic field components.

As briefly mentioned in the previous chapter a strategy to control numerical dissipation plays a crucial role in many computational simulations. Indeed, for many applications in computer simulations, if the solution does not have enough artificial viscosity implicitly in the algorithm, then the solution will go unstable unless more artificial viscosity is added explicitly to the calculation. Numerical dissipation is the direct result of the even-order derivatives that exist in the form of the modified equation.

Ideally, one wishes that his/her numerical algorithm solves the PDE's of

his/her interest exactly. But in reality, when the corresponding difference equations are applied to discretize the original PDE's, such difference equations might not be solving the original PDE's; rather they may be solving a set of different PDE's – the modified equations. This phenomenon gives rise to raise important meanings for the derivation and display of the modified equation. In this chapter, a new dissipation control algorithm will be established to solve the MHD induction equations on the staggered grid by taking an approach using modified equations. The resultant solution improvement from adopting the SDDA in MHD simulations will be validated and studied in Chapter 6.

4.1 Modified Equations of the Induction Equations

In the previous chapter it has been shown that, in the IEC algorithm, the second-order derivative terms are added and they explicitly control proper amount of numerical dissipations for the electric fields. However, one should realize that these dissipations have nothing to do with the dissipations that arise in solving the system of the induction equations themselves. To obtain the dissipation relation connected to the induction equations, it is suggested to examine the modified equations of the induction equations.

Let us consider the induction equations in two-dimension:

$$\frac{1}{\Delta t}\Big\{b^{n+1}_{x,i\pm1/2,j} - b^{n}_{x,i\pm1/2,j}\Big\} = \frac{1}{\Delta y}\Big\{-E^{n+1/2}_{z,i\pm1/2,j+1/2} + E^{n+1/2}_{z,i\pm1/2,j-1/2}\Big\}, \quad (4.1)$$

$$\frac{1}{\Delta t}\Big\{b^{n+1}_{y,i,j\pm1/2} - b^{n}_{y,i,j\pm1/2}\Big\} = \frac{1}{\Delta x}\Big\{E^{n+1/2}_{z,i+1/2,j\pm1/2} - E^{n+1/2}_{z,i-1/2,j\pm1/2}\Big\}. \quad (4.2)$$

First, in equation (4.1), one considers Taylor series expansions for $b^{n+1}_{x,i\pm1/2,j}$, $E^{n+1/2}_{z,i\pm1/2,j+1/2}$,

and $E^{n+1/2}_{z,i\pm1/2,j-1/2}$ as follows:

$$b^{n+1}_{x,i\pm1/2,j} = b^{n}_{x,i\pm1/2,j} + \frac{\partial b^{n}_{x,i\pm1/2,j}}{\partial t}\Delta t + \frac{\partial^2 b^{n}_{x,i\pm1/2,j}}{\partial t^2}\frac{\Delta t^2}{2} + \mathcal{O}(\Delta t^3), \quad (4.3)$$

$$E^{n+1/2}_{z,i\pm1/2,j+1/2} = E^{n+1/2}_{z,i\pm1/2,j} + \frac{\partial E^{n+1/2}_{z,i\pm1/2,j}}{\partial y}\frac{\Delta y}{2} + \frac{\partial^2 E^{n+1/2}_{z,i\pm1/2,j}}{\partial y^2}\frac{\Delta y^2}{8} + \mathcal{O}(\Delta y^3), \quad (4.4)$$

$$E^{n+1/2}_{z,i\pm1/2,j-1/2} = E^{n+1/2}_{z,i\pm1/2,j} - \frac{\partial E^{n+1/2}_{z,i\pm1/2,j}}{\partial y}\frac{\Delta y}{2} + \frac{\partial^2 E^{n+1/2}_{z,i\pm1/2,j}}{\partial y^2}\frac{\Delta y^2}{8} + \mathcal{O}(\Delta y^3).$$

Substituting equations (4.3)$\sim$(4.5) into (4.1), one has

$$\frac{1}{\Delta t}\Big[\frac{\partial b^{n}_{x,i\pm1/2,j}}{\partial t}\Delta t + \frac{\partial^2 b^{n}_{x,i\pm1/2,j}}{\partial t^2}\frac{\Delta t^2}{2} + \mathcal{O}(\Delta t^3)\Big] = \frac{1}{\Delta y}\Big[-\frac{\partial E^{n+1/2}_{z,i\pm1/2,j}}{\partial y}\Delta y + \mathcal{O}(\Delta y^3)\Big]. \quad (4.5)$$

Rearranging equation (4.5), one obtains

$$\frac{\partial b^{n}_{x,i\pm1/2,j}}{\partial t} + \frac{\partial E^{n+1/2}_{z,i\pm1/2,j}}{\partial y} = -\frac{\partial^2 b^{n}_{x,i\pm1/2,j}}{\partial t^2}\frac{\Delta t}{2} + \mathcal{O}(\Delta t^2, \Delta y^2). \quad (4.6)$$

Note that this equation (4.6) just derived is the modified equation of the original induction equation (1.6). This shows that when the difference equation (4.1) is used for MHD simulations it constitutes a solution of different PDE, namely, equation (4.6). Comparing with the original PDE of the induction equation (1.6), equation (4.6) contains an extra dissipation term (or artificial viscosity) $-\partial^2 b^{n}_{x,i\pm1/2,j}\big/\partial t^2$ on the right hand side and this extra term will effectively behave as a source. Since the sign of the dissipation term is negative, rather than positive, this artificial viscosity is destabilizing the solution rather than stabilizing. This phenomenon is hence *anti-dissipative* and the solution would be unstable, or at least lose accuracy, due to the accumulations of the anti-dissipative local truncation error which is shown to be proportional to Δt, over the computation time. This phenomenon might be even getting worse especially near regions of stagnation flows.

To yield useful information, the time derivative on the right hand side of the modified equation (4.6) can be replaced by spatial derivative, using the so-called *Cauchy-Kowalewski* procedure. Differentiating equation (4.6) with respect to t, one can obtain

$$\frac{\partial^2 b^n_{x,i\pm1/2,j}}{\partial t^2} = -\frac{\partial^2 E^{n+1/2}_{z,i\pm1/2,j}}{\partial t \partial y} - \frac{\partial^3 b^n_{x,i\pm1/2,j}}{\partial t^3}\frac{\Delta t}{2} + \mathcal{O}(\Delta t^2, \Delta y^2). \tag{4.7}$$

Substituting (4.7) from (4.6), one gets

$$\frac{\partial b^n_{x,i\pm1/2,j}}{\partial t} + \frac{\partial E^{n+1/2}_{z,i\pm1/2,j}}{\partial y} = \frac{\partial^2 E^{n+1/2}_{z,i\pm1/2,j}}{\partial t \partial y}\frac{\Delta t}{2} + \mathcal{O}(\Delta t^2, \Delta y^2). \tag{4.8}$$

In general, for a simple model linear advection PDE equation, $\frac{\partial u}{\partial t} + a\frac{\partial u}{\partial x} = 0$, one can replace all the time derivatives in a modified equation with the spatial derivatives by repeatedly differentiating the linear modified equation and obtain corresponding spatial derivatives instead. By contrast, the nonlinear induction equations are not such simple linear equations and the time derivative in $\partial^2 E^{n+1/2}_{z,i\pm1/2,j}\big/\partial t \partial y$ can hardly be replaced by the spatial derivative completely. To overcome this difficulty and accomplish an efficient dissipation control algorithm, the current study rather keeps the time derivative and uses that derivative information. Before proceeding to study the numerical algorithm of the SDDA scheme in the next section, the rest of this section will complete the discussion on deriving the modified equation of the induction equation for the y component magnetic field.

For equation (4.2), Taylor expansions yield:

$$b^{n+1}_{y,i,j\pm1/2} = b^n_{y,i,j\pm1/2} + \frac{\partial b^n_{y,i,j\pm1/2}}{\partial t}\Delta t + \frac{\partial^2 b^n_{y,i,j\pm1/2}}{\partial t^2}\frac{\Delta t^2}{2} + \mathcal{O}(\Delta t^3), \tag{4.9}$$

$$E^{n+1/2}_{z,i+1/2,j\pm1/2} = E^{n+1/2}_{z,i,j\pm1/2} + \frac{\partial E^{n+1/2}_{z,i,j\pm1/2}}{\partial x}\frac{\Delta x}{2} + \frac{\partial^2 E^{n+1/2}_{z,i,j\pm1/2}}{\partial x^2}\frac{\Delta x^2}{8} + \mathcal{O}(\Delta x^3), \tag{4.10}$$

$$E^{n+1/2}_{z,i-1/2,j\pm1/2} = E^{n+1/2}_{z,i,j\pm1/2} - \frac{\partial E^{n+1/2}_{z,i,j\pm1/2}}{\partial x}\frac{\Delta x}{2} + \frac{\partial^2 E^{n+1/2}_{z,i,j\pm1/2}}{\partial x^2}\frac{\Delta x^2}{8} + \mathcal{O}(\Delta x^3).$$

Substituting equations (4.9)$\sim$(4.11) into (4.2), one can obtain

$$\frac{1}{\Delta t}\Big[\frac{\partial b^n_{t,i,j\pm1/2}}{\partial t}\Delta t + \frac{\partial^2 b^n_{y,i,j\pm1/2}}{\partial t^2}\frac{\Delta t^2}{2} + \mathcal{O}(\Delta t^3)\Big] = \frac{1}{\Delta x}\Big[\frac{\partial E^{n+1/2}_{z,i,j\pm1/2}}{\partial x}\Delta x + \mathcal{O}(\Delta x^3)\Big]. \tag{4.11}$$

Canceling out Δt and Δx, and rearranging equation (4.11), one achieves

$$\frac{\partial b^n_{y,i,j\pm1/2}}{\partial t} + \frac{\partial\left(-E^{n+1/2}_{z,i,j\pm1/2}\right)}{\partial x} = -\frac{\partial^2 b^n_{y,i,j\pm1/2}}{\partial t^2}\frac{\Delta t}{2} + \mathcal{O}(\Delta t^2, \Delta x^2). \tag{4.12}$$

Notice again that the sign of the dissipation term $\partial^2 b^n_{y,i,j\pm1/2}\big/\partial t^2$ is negative and the term is proportional to Δt. Thus this will effectively introduce the same anti-dissipative phenomenon as in the case of the modified induction equation for the x component magnetic field. Further differentiating equation (4.12) with respect to t, one can obtain

$$\frac{\partial^2 b^n_{y,i,j\pm1/2}}{\partial t^2} = -\frac{\partial^2\left(-E^{n+1/2}_{z,i,j\pm1/2}\right)}{\partial t\partial x} - \frac{\partial^3 b^n_{y,i,j\pm1/2}}{\partial t^3}\frac{\Delta t}{2} + \mathcal{O}(\Delta t^2, \Delta x^2). \tag{4.13}$$

Substituting (4.13) from (4.12), one gets

$$\frac{\partial b^n_{y,i,j\pm1/2}}{\partial t} + \frac{\partial\left(-E^{n+1/2}_{z,i,j\pm1/2}\right)}{\partial x} = \frac{\partial^2\left(-E^{n+1/2}_{z,i,j\pm1/2}\right)}{\partial t\partial x}\frac{\Delta t}{2} + \mathcal{O}(\Delta t^2, \Delta x^2). \tag{4.14}$$

4.2 Difference Equations for the Dissipation-Control Algorithm

Now that the modified equations for the induction equations have been derived, one still needs to obtain a proper discretization scheme to use the dissipation terms in the SDDA scheme numerically. One way to achieve this is to propose an explicit,

forward[1] *time centered space* (FTCS) discretization for the terms $\frac{\partial^2}{\partial t \partial y} E^{n+1/2}_{z,i\pm 1/2,j}$ and $\frac{\partial^2}{\partial t \partial x}\left(-E^{n+1/2}_{z,i,j\pm 1/2}\right)$ in equations (4.8) and (4.14). For the rest of the derivative terms on the left hand side of equations (4.8) and (4.14), one should keep the original scheme (which is FTCS in fact) as is discretized in equations (4.1) and (4.2), because the derived modified equations stem from such discretization. For comparison, stencil diagrams of FTCS and BTCS are shown in Figure (4.1).

4.2.1 FTCS: Forward in Time Centered in Space

Equations (4.8) and (4.14) are now discretized in an FTCS manner as below. To control the anti-dissipative effect from the term $\frac{\partial^2}{\partial t \partial y} E^{n+1/2}_{z,i\pm 1/2,j}$ in the x component equation (4.8), a corresponding *dissipative* contribution should be made by adding the equivalent term with an opposite sign. In practical point of view, $\frac{\partial^2}{\partial t \partial y} E^{n+1/2}_{z,i\pm 1/2,j} \frac{\Delta t}{2}$ in equation (4.8) is to be replaced with $-\frac{\partial^2}{\partial t \partial y} E^{n+1/2}_{z,i\pm 1/2,j} \frac{\Delta t}{2}$.

First, one can discretize the derivative as follow:

$$\begin{aligned} -\frac{\partial^2 E^{n+1/2}_{z,i\pm 1/2,j}}{\partial t \partial y} &= -\frac{\partial}{\partial t}\frac{1}{\Delta y}\left\{E^{n+1/2}_{z,i\pm 1/2,j+1/2} - E^{n+1/2}_{z,i\pm 1/2,j-1/2}\right\} \\ &= -\frac{1}{\Delta t \Delta y}\Big\{\left(E^{n+1/2}_{z,i\pm 1/2,j+1/2} - E^{n+1/2}_{z,i\pm 1/2,j-1/2}\right) \\ &\qquad -\left(E^{n-1/2}_{z,i\pm 1/2,j+1/2} - E^{n-1/2}_{z,i\pm 1/2,j-1/2}\right)\Big\}. \end{aligned} \tag{4.15}$$

Notice that the cell-cornered electric fields $E^{n+1/2}_{z,i\pm 1/2,j\pm 1/2}$ are available from the IEC scheme (3.14). Multiplying by $\Delta t/2$ into the above equation (4.15), according to

[1]It will be used that the forward in time discretization refers to an explicit method, and the backward in time refers to an implicit method. See [51].

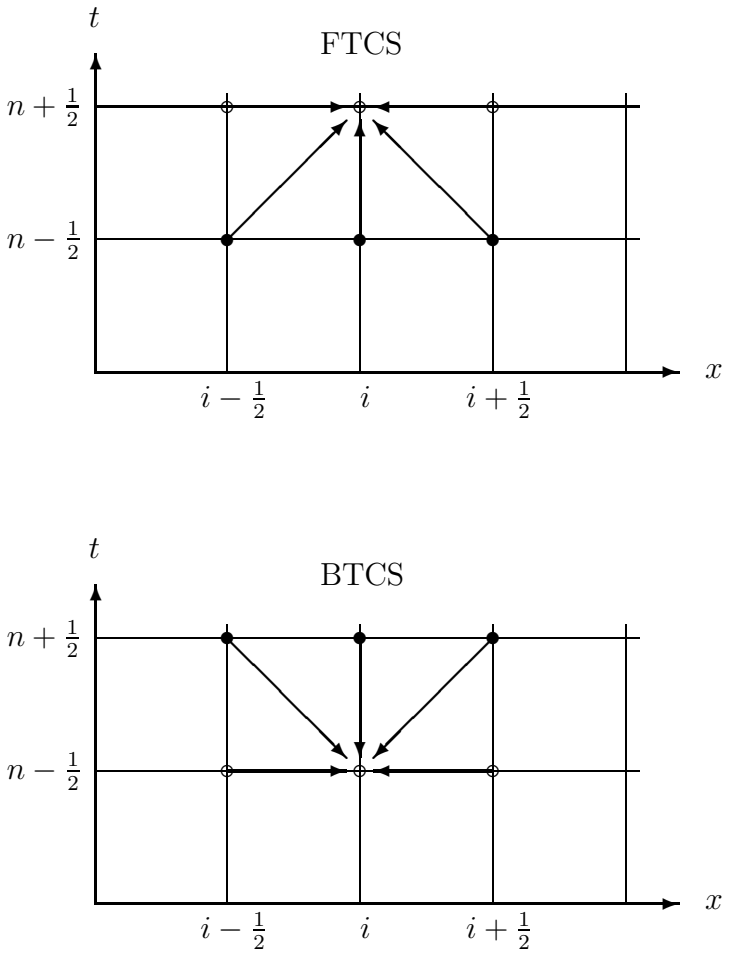

Figure 4.1: Comparison of stencil diagrams for forward time centered space (FTCS) and backward time centered space (BTCS). The circles represent the nodal points at which the derivative is considered and the solid dots represent the nodal points from which the forward and backward extrapolations are collected.

(4.8), one can get

$$\begin{aligned}\frac{1}{\Delta t}\left\{b^{n+1}_{x,i\pm1/2,j}-b^{n}_{x,i\pm1/2,j}\right\} &= -\frac{1}{\Delta y}\left\{E^{n+1/2}_{z,i\pm1/2,j+1/2}-E^{n+1/2}_{z,i\pm1/2,j-1/2}\right\}\\ &\quad -\frac{1}{2\Delta y}\Big\{\left(E^{n+1/2}_{z,i\pm1/2,j+1/2}-E^{n+1/2}_{z,i\pm1/2,j-1/2}\right)\\ &\quad -\left(E^{n-1/2}_{z,i\pm1/2,j+1/2}-E^{n-1/2}_{z,i\pm1/2,j-1/2}\right)\Big\}. \quad (4.16)\end{aligned}$$

Rearranging equation (4.16), the final form of the x component induction equation for the SDDA scheme now yields

$$\begin{aligned}b^{n+1}_{x,i\pm1/2,j} &= b^{n}_{x,i\pm1/2,j}-\frac{\Delta t}{\Delta y}\left\{E^{n+1/2}_{z,i\pm1/2,j+1/2}-E^{n+1/2}_{z,i\pm1/2,j-1/2}\right\}\\ &\quad -\frac{\Delta t}{2\Delta y}\Big\{\left(E^{n+1/2}_{z,i\pm1/2,j+1/2}-E^{n+1/2}_{z,i\pm1/2,j-1/2}\right)\\ &\quad -\left(E^{n-1/2}_{z,i\pm1/2,j+1/2}-E^{n-1/2}_{z,i\pm1/2,j-1/2}\right)\Big\}. \quad (4.17)\end{aligned}$$

Similarly, for the y component equation (4.14), one gets

$$\begin{aligned}\frac{1}{\Delta t}\left\{b^{n+1}_{y,i,j\pm1/2}-b^{n}_{y,i,j\pm1/2}\right\} &= -\frac{1}{\Delta x}\left\{-E^{n+1/2}_{z,i+1/2,j\pm1/2}+E^{n+1/2}_{z,i-1/2,j\pm1/2}\right\}\\ &\quad -\frac{1}{2\Delta x}\Big\{\left(-E^{n+1/2}_{z,i+1/2,j\pm1/2}+E^{n+1/2}_{z,i-1/2,j\pm1/2}\right)\\ &\quad -\left(-E^{n-1/2}_{z,i+1/2,j\pm1/2}+E^{n-1/2}_{z,i-1/2,j\pm1/2}\right)\Big\}. \quad (4.18)\end{aligned}$$

Rearranging terms and multiplying by Δt in equations (4.18), one now obtains the final SDDA form for the y component equation,

$$\begin{aligned}b^{n+1}_{y,i,j\pm1/2} &= b^{n}_{y,i,j\pm1/2}-\frac{\Delta t}{\Delta x}\left\{-E^{n+1/2}_{z,i+1/2,j\pm1/2}+E^{n+1/2}_{z,i-1/2,j\pm1/2}\right\}\\ &\quad -\frac{\Delta t}{2\Delta x}\Big\{\left(-E^{n+1/2}_{z,i+1/2,j\pm1/2}+E^{n+1/2}_{z,i-1/2,j\pm1/2}\right)\\ &\quad -\left(-E^{n-1/2}_{z,i+1/2,j\pm1/2}+E^{n-1/2}_{z,i-1/2,j\pm1/2}\right)\Big\}. \quad (4.19)\end{aligned}$$

Advantages of using the FTCS method for $\frac{\partial^2}{\partial t\partial y}E^{n+1/2}_{z,i\pm1/2,j}$ and $\frac{\partial^2}{\partial t\partial x}\left(-E^{n+1/2}_{z,i,j\pm1/2}\right)$ are threefold. First, the choice is consistent with the discretization originally used

for the derivatives in (4.1) and (4.2). Second, the centered in space discretization is also consistent with a physical consideration, in that the EMF is evaluated via Stokes' Theorem, followed by the line integrals, resulting the same formulations as in equations (3.6)$\sim$(3.8). Finally, the FTCS scheme as applied to $\frac{\partial^2}{\partial t \partial y} E^{n+1/2}_{z,i\pm 1/2,j}$ and $\frac{\partial^2}{\partial t \partial x}\left(-E^{n+1/2}_{z,i,j\pm 1/2}\right)$ requires the smallest possible stencil size in both space and time. In terms of the stencil range, the centered in space discretization only utilizes two cell-cornered electric field values that are always available within each cell. Thus, there is no need to obtain the neighboring cell's information and the scheme is truly local. Not only this affects computational efficiency, but also this will guarantee to preserve the divergence-free constraint for the SDDA scheme. In other words, for example, if other spatial discretization which requires wider stencil range such as an upwinding method were chosen, the spatial discretization would also require each neighboring cell's information, which will ultimately break the symmetry relationship[2] that should be guaranteed to keep the divergence-free constraint. In the next subsection, a numerical proof will be presented which shows the SDDA scheme developed in equations (4.17) and (4.19)indeed satisfies the divergence-free property.

One can make several useful observations in the SDDA development. The second-order in time and space dissipation controls for the induction equations are made available by considering the modified equations. From this study, the anti-dissipative relationship has been well introduced and established, which has been neglected in all the existing MHD algorithms. Such anti-dissipation controls have been achieved by recovering the dissipation relationships by balancing the anti-dissipation

[2]The perfect cancellations of the cell-cornered electric fields as was observed in equation (3.12).

terms with the oppositely signed dissipative terms in the modified induction equations. To incorporate the dissipation relationships, the SDDA scheme uses FTCS differencing method to discretize the related temporal and spatial derivatives. Several key advantages in using FTCS method were just mentioned above. The SDDA scheme, thus, explicitly controls the anti-dissipative phenomena in the evolutions of the cell face-centered magnetic fields. Lastly, the SDDA scheme can be incorporated with any CT based schemes without requiring any extra overhead. The algorithmic development achieved in the SDDA scheme will resolve undesired magnetic field growth in the induction equations and keep the proper amount of dissipations. In Chapter 6, it will be shown that there are crucial improvements in solutions of the magnetic fields by using the SDDA scheme.

4.2.2 Parameterized form of the SDDA

Finally, one can further parameterize the dissipation terms in equations (4.17) and (4.19). Let us choose a dissipation parameter $0 \leq \nu \leq 1$. The parameterized dissipation relationships for the SDDA scheme become

$$\begin{aligned} b^{n+1}_{x,i\pm1/2,j} &= b^{n}_{x,i\pm1/2,j} - \frac{\Delta t}{\Delta y}\left\{E^{n+1/2}_{z,i\pm1/2,j+1/2} - E^{n+1/2}_{z,i\pm1/2,j-1/2}\right\} \\ &\quad -\nu\frac{\Delta t}{2\Delta y}\Big\{\left(E^{n+1/2}_{z,i\pm1/2,j+1/2} - E^{n+1/2}_{z,i\pm1/2,j-1/2}\right) \\ &\quad -\left(E^{n-1/2}_{z,i\pm1/2,j+1/2} - E^{n-1/2}_{z,i\pm1/2,j-1/2}\right)\Big\}, \qquad (4.20) \\ b^{n+1}_{y,i,j\pm1/2} &= b^{n}_{y,i,j\pm1/2} - \frac{\Delta t}{\Delta x}\left\{-E^{n+1/2}_{z,i+1/2,j\pm1/2} + E^{n+1/2}_{z,i-1/2,j\pm1/2}\right\} \\ &\quad -\nu\frac{\Delta t}{2\Delta x}\Big\{\left(-E^{n+1/2}_{z,i+1/2,j\pm1/2} + E^{n+1/2}_{z,i-1/2,j\pm1/2}\right) \\ &\quad -\left(-E^{n-1/2}_{z,i+1/2,j\pm1/2} + E^{n-1/2}_{z,i-1/2,j\pm1/2}\right)\Big\}. \qquad (4.21) \end{aligned}$$

Thus far have obtained two slightly different versions of the SDDA equations, the first is without parameterization as found in (4.17) and (4.19), and the second with parameterization as in (4.20) and (4.21). Otherwise mentioned differently, the equations (4.20) and (4.21) will be generally called as *the SDDA equations* throughout the dissertation.

4.2.3 Initial Condition of the SDDA Equations

Since the SDDA scheme makes use of the electric fields at previous time step, one needs to initialize the electric fields before solving the SDDA equations. Notice that, in general, one does not require to initialize the electric fields in the base CT scheme. One simple choice for an initial condition of the electric fields can be obtained by using the relationship $\mathbf{E} = -\mathbf{u} \times \mathbf{B}$ directly. After initializing the cell-centered velocity and magnetic fields, one can get

$$u^0_{i+1/2,j+1/2} = \frac{1}{4}\left(u^0_{i,j} + u^0_{i+1,j} + u^0_{i,j+1} + u^0_{i+1,j+1}\right), \tag{4.22}$$

$$v^0_{i+1/2,j+1/2} = \frac{1}{4}\left(v^0_{i,j} + v^0_{i+1,j} + v^0_{i,j+1} + v^0_{i+1,j+1}\right), \tag{4.23}$$

$$B^0_{x,i+1/2,j+1/2} = \frac{1}{4}\left(B^0_{x,i,j} + B^0_{x,i+1,j} + B^0_{x,i,j+1} + B^0_{x,i+1,j+1}\right), \tag{4.24}$$

$$B^0_{y,i+1/2,j+1/2} = \frac{1}{4}\left(B^0_{y,i,j} + B^0_{y,i+1,j} + B^0_{y,i,j+1} + B^0_{y,i+1,j+1}\right). \tag{4.25}$$

Then the cell-cornered electric fields can be initialized[3] by

$$E^0_{z,i+1/2,j+1/2} = v^0_{i+1/2,j+1/2} B^0_{x,i+1/2,j+1/2} - u^0_{i+1/2,j+1/2} B^0_{y,i+1/2,j+1/2}. \tag{4.26}$$

[3]With an abuse of notation, one can let $E^0_{z,i+1/2,j+1/2} \equiv E^{-1/2}_{z,i+1/2,j+1/2}$ in (4.20) and (4.21) for $n = 0$.

As for another choice to handle the SDDA equations initially, the base induction equations (3.9) and (3.10) can be solved by taking $\nu = 0$ in (4.20) and (4.21) to get the very first time step $n = 1$, and take nonzero ν for $n > 1$. A proper choice of nonzero ν will be made in Chapter 6 in the test suite.

4.3 Proof of Divergence-Free Property of FTCS for SDDA

In this section, a proof of the divergence-free property for the SDDA equations is presented. As before one assumes that $(\nabla \cdot \mathbf{B})^n_{(i,j)} = 0$ initially at time step n. Then

$$
\begin{aligned}
(\nabla \cdot \mathbf{B})^{n+1}_{i,j} &= \frac{b^{n+1}_{x,i+1/2,j} - b^{n+1}_{x,i-1/2,j}}{\Delta x} + \frac{b^{n+1}_{y,i,j+1/2} - b^{n+1}_{y,i,j-1/2}}{\Delta y} \\
&= \frac{1}{\Delta x}\Big\{ b^n_{x,i+1/2,j} - \frac{\Delta t}{\Delta y}(E^{n+1/2}_{z,i+1/2,j+1/2} - E^{n+1/2}_{z,i+1/2,j-1/2}) \\
&\qquad -\nu\frac{\Delta t}{2\Delta y}\Big[E^{n+1/2}_{z,i+1/2,j+1/2} - E^{n+1/2}_{z,i+1/2,j-1/2} - E^{n-1/2}_{z,i+1/2,j+1/2} + E^{n-1/2}_{z,i+1/2,j-1/2}\Big] \\
&\qquad -b^n_{x,i-1/2,j} + \frac{\Delta t}{\Delta y}(E^{n+1/2}_{z,i-1/2,j+1/2} - E^{n+1/2}_{z,i-1/2,j-1/2}) \\
&\qquad +\nu\frac{\Delta t}{2\Delta y}\Big[E^{n+1/2}_{z,i-1/2,j+1/2} - E^{n+1/2}_{z,i-1/2,j-1/2} - E^{n-1/2}_{z,i-1/2,j+1/2} + E^{n-1/2}_{z,i-1/2,j-1/2}\Big]\Big\} \\
&\quad +\frac{1}{\Delta y}\Big\{ b^n_{y,i,j+1/2} - \frac{\Delta t}{\Delta x}(-E^{n+1/2}_{z,i+1/2,j+1/2} + E^{n+1/2}_{z,i-1/2,j+1/2}) \\
&\qquad +\nu\frac{\Delta t}{2\Delta x}\Big[-E^{n+1/2}_{z,i+1/2,j+1/2} + E^{n+1/2}_{z,i-1/2,j+1/2} + E^{n-1/2}_{z,i+1/2,j+1/2} - E^{n-1/2}_{z,i-1/2,j+1/2}\Big] \\
&\qquad -b^n_{y,i,j-1/2} + \frac{\Delta t}{\Delta x}(-E^{n+1/2}_{z,i+1/2,j-1/2} + E^{n+1/2}_{z,i-1/2,j-1/2}) \\
&\qquad -\nu\frac{\Delta t}{2\Delta x}\Big[-E^{n+1/2}_{z,i+1/2,j-1/2} + E^{n+1/2}_{z,i-1/2,j-1/2} + E^{n-1/2}_{z,i+1/2,j-1/2} - E^{n-1/2}_{z,i-1/2,j-1/2}\Big]\Big\} \\
&= \frac{b^n_{x,i+1/2,j} - b^n_{x,i-1/2,j}}{\Delta x} + \frac{b^n_{y,i,j+1/2} - b^n_{y,i,j-1/2}}{\Delta y} \\
&\quad +\frac{\Delta t}{\Delta x \Delta y}\Big\{ -E^{n+1/2}_{z,i+1/2,j+1/2} + E^{n+1/2}_{z,i+1/2,j-1/2} + E^{n+1/2}_{z,i-1/2,j+1/2} - E^{n+1/2}_{z,i-1/2,j-1/2} \\
&\qquad\qquad +E^{n+1/2}_{z,i+1/2,j+1/2} - E^{n+1/2}_{z,i-1/2,j+1/2} - E^{n+1/2}_{z,i+1/2,j-1/2} + E^{n+1/2}_{z,i-1/2,j-1/2}\Big\}
\end{aligned}
$$

$$
\begin{aligned}
&+\nu\frac{\Delta t}{2\Delta x\Delta y}\Big\{-E^{n+1/2}_{z,i+1/2,j+1/2}+E^{n+1/2}_{z,i+1/2,j-1/2}+E^{n+1/2}_{z,i-1/2,j+1/2}-E^{n+1/2}_{z,i-1/2,j-1/2}\\
&\qquad +E^{n-1/2}_{z,i+1/2,j+1/2}-E^{n-1/2}_{z,i+1/2,j-1/2}-E^{n-1/2}_{z,i-1/2,j+1/2}+E^{n-1/2}_{z,i-1/2,j-1/2}\\
&\qquad +E^{n+1/2}_{z,i+1/2,j+1/2}-E^{n+1/2}_{z,i-1/2,j+1/2}-E^{n+1/2}_{z,i+1/2,j-1/2}+E^{n+1/2}_{z,i-1/2,j-1/2}\\
&\qquad -E^{n-1/2}_{z,i+1/2,j+1/2}+E^{n-1/2}_{z,i-1/2,j+1/2}+E^{n-1/2}_{z,i+1/2,j-1/2}-E^{n-1/2}_{z,i-1/2,j-1/2}\Big\}\\
&=(\nabla\cdot\mathbf{B})^n_{i,j}\\
&=0. \qquad (4.27)
\end{aligned}
$$

Notice that the symmetry relationship gives perfect cancellations of the electric fields from which the divergence-free constraint is achieved. This proof also shows that the SDDA scheme preserves the divergence-free property in a local sense, leading to a fact that the constraint will also be easily maintained on AMR block structures. A parallel, AMR implementation of the SDDA scheme in the FLASH [36] computational framework will be discussed in the next chapter.

4.4 Reconstruction of Cell-Centered Fields

The dissipation controlled, divergence-free cell face-centered magnetic fields are available by solving the SDDA equations. To update other volumetric variables in the CT-type of Godunov based MHD solver, one now needs to reconstruct the cell-centered magnetic fields to evaluate the upwind step of the Godunov method. In the base CT scheme by Balsara & Spicer [9], and also many other CT schemes, one defines the volume-averaged magnetic field components at cell centers by taking the arithmetic average of the cell face-centered, divergence-free magnetic fields as

(see figure 4.2),

$$B^n_{x,i,j} = \frac{1}{2}\left(b^n_{x,i-1/2,j} + b^n_{x,i+1/2,j}\right), \tag{4.28}$$

$$B^n_{y,i,j} = \frac{1}{2}\left(b^n_{y,i,j-1/2} + b^n_{y,i,j+1/2}\right). \tag{4.29}$$

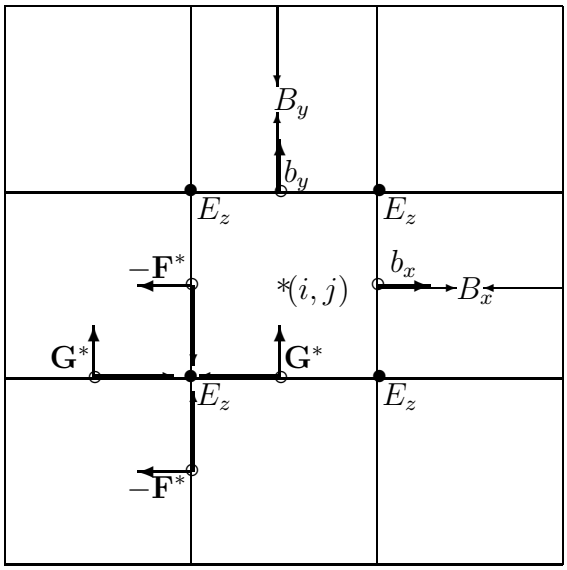

Figure 4.2: The 2D geometry of staggered mesh with interpolations. The upwinded fluxes $\mathbf{F}^*$ and $\mathbf{G}^*$ from the high order Godunov scheme are represented with short bold arrows and the interpolations for updating $\mathbf{B}$ with long thin arrows in the figure.

In this reconstruction step, the divergence-free constraint for the cell-centered fields is no longer to be preserved. Therefore, although the divergenceless evolution of the face centered fields are ensured after each SDDA step, the numerical monopoles are still introduced when one solves the upwind step of the Godunov method. This is because the upwinding procedure in the Riemann problem is based

on the cell center values of the magnetic fields, not the cell face-centered fields. (See also Appendix B.)

To overcome this non divergence-free issue for the magnetic fields at cell centers, Balsara [10, 11] recently proposed a new reconstruction algorithm that also ensures the divergence-free property for the cell-centered magnetic fields. His scheme uses

$$B^n_{x,i,j} = \frac{1}{2}\left(b^n_{x,i-1/2,j} + b^n_{x,i+1/2,j}\right) - a_{xx}\frac{\Delta x^2}{6}, \tag{4.30}$$

$$B^n_{y,i,j} = \frac{1}{2}\left(b^n_{y,i,j-1/2} + b^n_{y,i,j+1/2}\right) - c_{yy}\frac{\Delta y^2}{6}, \tag{4.31}$$

where the nonzero coefficients a_{xx} and c_{yy} are described therein. Although this approach has an extra advantage to guarantee the divergence-free constraint for the cell-centered fields, it is clear from (4.30) and (4.31) that the base reconstruction scheme in (4.28) and (4.29) are sufficient for a second-order scheme[4]. Thus the USM-IEC-SDDA scheme uses (4.28) and (4.29) as a default choice.

4.5 Remarks on IEC-SDDA

Some remarks are relevant by making observations on advantages of using the IEC-SDDA approach. First, the method provides the divergence-free fields in real space up to computer's round-off error. In this sense one can guarantee the divergence-free fields in the discrete formulation at all points on the computational domain. Keeping the divergence-free constraint in simulations is essential to com-

[4]In fact, it has been reported in [55] that there is no noticeable difference between the results of using the base scheme (4.28)∼(4.29) and the new scheme (4.30)∼(4.31).

pute correct geometries of the magnetic fields.

Second, because the divergence-free constraint is true in real space, the resultant magnetic fields are physically meaningful in a continuous sense over the computational domain. This is in contrast to the vector divergence-cleaning method, in which the divergence-free properties of the fields can be viewed only at discrete points in Fourier space.

Third, the nice local property in treating the divergence-free constraint enables minimal inter-communication on parallel machines, and thus an extension to AMR grid is natural to achieve.

Fourth, the issues such as extra handling with solving the elliptic Poisson equations and associated aliasing errors (if FFTs are used for the purpose) can be removed.

Finally, a novel way to control anti-dissipative phenomena, which are potentially subject to solving the induction equations, has been well established. By including the corresponding dissipation terms, unphysical growth of the magnetic fields can be resolved in a very efficient way. The importance of keeping the dissipation control terms will be shown to be very crucial in some MHD simulations and such impact will be further studied in the test suite described in Chapter 6.

Chapter 5

USM-IEC-SDDA IN FLASH3 WITH PARAMESH3

It would appear that
we have reached the limits of
what is possible to achieve with computer technology,
although one should be careful with such statements,
as they tend to sound pretty silly in five years.

Johann von Neumann, 1947

A successful implementation of the USM-IEC-SDDA scheme in the FLASH3 [36] computational framework is described in this chapter. The USM-IEC-SDDA scheme has been extended to a parallel adaptive mesh refinement (AMR) scheme that provides high performance computation (HPC) on massively parallel computational architectures. Special emphasis will be made on ideas that lead to preserve the divergence-free constraint at prolongation procedures on AMR grids.

FLASH is a publicly available modular, adaptive mesh, parallel simulation code which has been developed and evolved at the ASC/Alliances Flash Center under the auspices of the Department of Energy Advanced Simulation and Computing program. A new generation of the code, FLASH 3, recently has been developed to provide better code architectures. Within FLASH 3, the USM-IEC-SDDA scheme has been successfully implemented as a magnetohydrodynamics solver and will be

publicly released in early Fall, 2006.

In the following sections, we start with brief descriptions of the FLASH code and the PARAMESH library. As far as the purpose of this dissertation concerns, later sections mainly focus on three important routines that are required in parallel AMR grids for the USM-IEC-SDDA scheme: implementations of flux conservation, electric field correction, and divergence-free preserving prolongation.

5.1 FLASH Code

The Flash code is a collection of interoperable modules that are combined to generate different scientific applications. Examples of such applications consist of a wide variety of astrophysical problems as well as basic physics problems. A brief list includes X-ray bursts, magnetized galactic bubbles, classical novae, Type Ia supernovae as for astrophysics aspects, and the cellular structure of detonation, wind/wave interactions, and Rayleigh-Taylor instability as for basic physics aspects.

FLASH is written in a few different scientific languages. The majority is written in Fortran 90 and the rest in C and Python. It approximately consists of 600,000 lines of code and was awarded the 2000 Gordon Bell Award [22] in the Special Category for achieving 0.24 TFLOPS on 6420 processors of ASCI Red supercomputer.

The new architecture of FLASH 3 takes its primary effort to further simplify and streamline the date management by rigorously defining module architecture and clarifying the rules of interpolarbility between different modules. This has been

achieved by decentralizing the database. In previous versions the solution data was centralized and primarily owned by the *database* modules. Simultaneously, the mesh modules and the IO modules have to be given unrestricted to access to the solution data, completely violating the basic assumption of modularity. In FLASH 3, the database is decentralized in such a way that individual modules own the data most relevant to them. The database can be accessed through the use of accessor functions by other modules. For instance, the driver module owns the time step dt, while any module can get the value through accessor functions, the driver reserves the right to modify it so that it can not be accidentally changed. Other development of FLASH 3 also includes interfaces and inheritance of the modules, and eliminates lateral interactions between modules.

The USM-IEC-SDDA scheme has been implemented as an MHD solver of FLASH 3. In earlier versions of FLASH, the operator splitting based 8-wave scheme had been implemented. Successful implementation of the USM-IEC-SDDA scheme will provide an alternative choice to the user community with a new operator unsplit, flux-CT type of MHD solver.

5.2 Parallel Adaptive Mesh Refinement: PARAMESH

FLASH uses the PARAMESH [62] library to manage a block-structured adaptive grid, refining/de-refining block structures to increase/decrease resolutions only in local regions of flow where higher resolution is needed most. PARAMESH uses a block-structured or patch-based adaptive mesh refinement scheme that is a subset

of the Berger-Oliger [15] type algorithm. Each block contains n^d zones in d dimensions, and its data structure is in 2^d-tree hierarchy structure. A factor of 2 jumps in refinement between adjacent blocks is allowed. PARAMESH provides functions to handle mesh refinement/de-refinement, distribution of work to processors (parallel load balancing via Morton space-filling curve) and guard cell filling.

For ensuring consistency at a jump in refinement, PARAMESH also provides flux conservation, and vector fields (electric fields for the current study) correction where blocks of different refinement abut one other. For correct simulations of MHD flows, these routines should be called and performed to use consistent values of fluxes and electric fields at adjoining block interfaces that share coarse and refined block meshes. The next subsections will briefly describe these routines and the ways in which they have been implemented for USM-IEC-SDDA with PARAMESH in the FLASH 3 framework.

PARAMESH takes each block a logically Cartesian, uniformly spaced submesh, which keeps a block's children in a nested tree data structure. Each refined child block has a cell size one-half as large as its parent block in each spatial dimension.

The refinement criterion used by PARAMESH follows from the error estimator used to capture shocks by Löner (1987). Löner's estimator is a modified second derivative, normalized by the average of the gradient over one computational cell. The estimator, thus, has the advantage that it uses an entirely local calculation, and can be applied to any of the solution variables or any combination of them. The default variables (u in equation (5.1)) are density and pressure in PARAMESH. In

multidimension, the criterion can be written as

$$E_{i_1,i_2,i_3} = \left[\frac{\sum_{p,q} \left(\frac{\partial^2 u}{\partial x_p \partial x_q} \Delta x_p \Delta x_q \right)^2}{\sum_{p,q} \left\{ \left(|\frac{\partial u}{\partial x_p}|_{i_p+1/2} + |\frac{\partial u}{\partial x_p}|_{i_p-1/2} \right) \Delta x_p + \epsilon \frac{\partial^2 |u|}{\partial x_p \partial x_q} \Delta x_p \Delta x_q \right\}^2} \right]^{1/2}, \quad (5.1)$$

where the sums are carried out over coordinate directions, partial derivatives are evaluated at the center of the i_1, i_2, i_3-th zone, and the constant ϵ is given a value of 10^{-2}. The last term in the denominator with ϵ plays as a filter, preventing refinement of small ripples. A block is refined if $\max E_{i_1,i_2,i_3} > C_1$ and de-refined if $\max E_{i_1,i_2,i_3} < C_2$, where the maximum is taken over each block. FLASH default values for C_1, C_2 are $0.8, 0.2$, respectively.

5.2.1 AMR Restriction via Flux Conservation

The high-order Godunov type based schemes use fluxes at cell interfaces to update the cell-centered volumetric variables such as fluxes of mass, momentum and energy. Also in the IEC algorithm fluxes are used to construct the electric fields at cell corners. Such electric fields are then used to evolve the cell face-centered magnetic fields in the SDDA scheme. As a consequence, the cell-centered variables and the cell face-centered magnetic field variables are strongly tied with correct usages of fluxes at all times in the simulations. These requirements are automatically obtained if there is no refinement used for the simulation. By contrast, if one decides to use adaptive mesh refinement, it is required to enforce the flux conservation to make sure the computed fluxes at block interfaces of different refinement levels are consistent and being used for both the fine cells and the coarse cells.

To perform flux conservation routines, one first needs to call a FLASH 3 mod-

ule `Grid_putFluxData.F90` to store the computed fluxes at the PARAMESH arrays that are reserved for fluxes. That is, in a block computation routine one can adopt

```
begin block-wise computation
call Grid_putFluxData(blockID,IAXIS,xflux,datasize)
call Grid_putFluxData(blockID,JAXIS,yflux,datasize)
call Grid_putFluxData(blockID,KAXIS,zflux,datasize)
end of block-wise computation
```

These calls put fluxes `xflux, yflux, zflux` in x, y, z-directions into the PARAMESH arrays in a direction specified by axis information, `IAXIS, JAXIS, KAXIS` and for boundary cells for block having `blockID`.

Now the FLASH 3 flux conservation routines are to be called, viz.,

```
call Grid_conserveFluxes(myPE,IAXIS,level)
call Grid_conserveFluxes(myPE,JAXIS,level)
call Grid_conserveFluxes(myPE,KAXIS,level)
```

where `myPE` is an integer value which is a current processor number, and `level` an integer that carries the refinement level. Upon calling `Grid_conserveFluxes`, the flux in the parent that was computed by the more accurate fine zones is taken as the *correct* flux through the zone interface and is passed to the corresponding coarse face on the neighboring block. The idea of flux conservations in two-dimension is shown in figure 5.1.

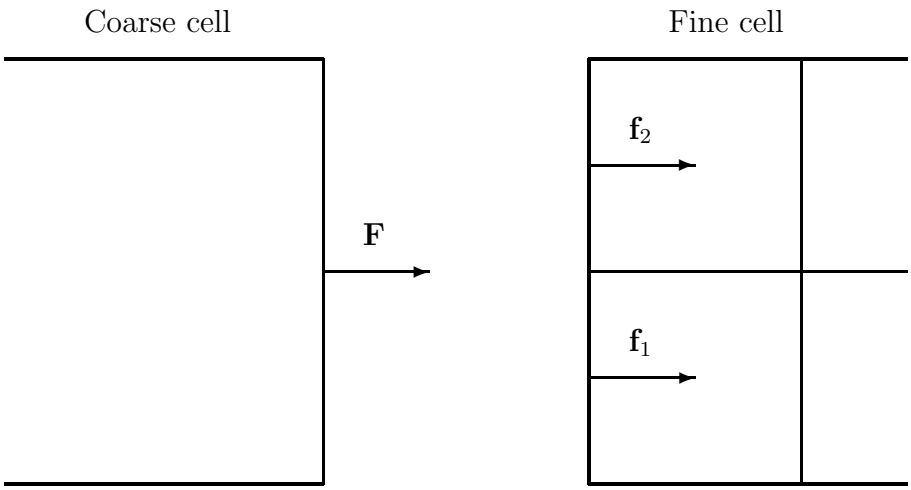

Figure 5.1: The 2D geometry of flux conservation. At a jump in refinement, the sum of fluxes calculated in the fine cell ($\mathbf{f}_1 + \mathbf{f}_2$) replaces the flux in the coarse cell ($\mathbf{F}$). Note that PARAMESH limits the jumps in refinement to be one level between two neighboring blocks.

5.2.2 AMR Restriction via Electric Field Correction

Similar consideration as the flux conservation should be also made for the electric fields at the cell corners that are sharing blocks at different levels of refinements. In FLASH 3, the flux conservation routines are readily available, for the PPM based hydrodynamics solver uses the same conservation requirement as well. However, a new implementation of a generic electric field correction routine is in need for the MHD modules, and such a brief implementation to meet the purpose of the current study is now presented in this subsection.

The arrays called `bedge_face*_#` are reserved in PARAMESH to store the edge-based variables. The symbols `*` and `#` denote x, y and z directions so as to represent data perpendicular to the `*`–axis and pointing in the `#`–direction. For instances, `bedge_facex_z` can be used for storing data $E_z(i, :, :)$, and `bedge_facey_z` for $E_z(:, j, :)$. Using these PARAMESH arrays, the USM-IEC-SDDA calls a generic electric field correction routine `mhd_electricFix.F90`, where the routine further calls `amr_edge_average.F`, e.g.,

```
do i=1, all_paramesh_blocks
   bedge_face*_#=oldElectricField
enddo
call amr_edge_average
do i=1, all_paramesh_blocks
   newElectricField=bedge_face*_#
enddo
```

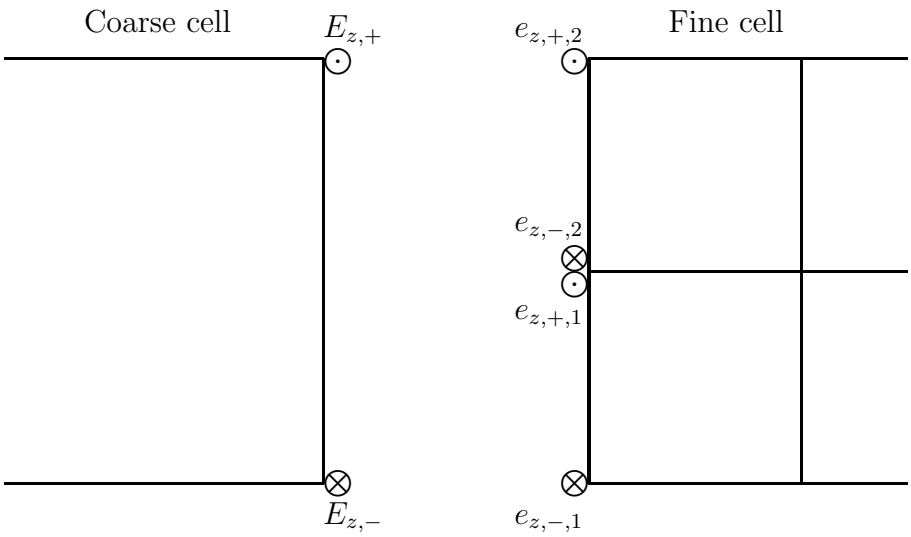

Figure 5.2: The 2D geometry of electric field correction. The symbol $\odot$ represents the electric field E_z pointing out of the figure and $\otimes$ represents the field pointing into the figure at each cell corner.

Calling the routine `amr_edge_average` will sum the edge (edge in 3D, corner in 2D) data values to ensure consistent evaluation required in the circulation integrals. In two-dimension, this routine simply becomes replacing the cell cornered electric fields at the coarse cell by the fields at the fine cell correspondingly. As illustrated in figure 5.2, this means

$$E_{z,+} = e_{z,+,2}, E_{z,-} = e_{z,-,1}, \tag{5.2}$$

where $e_{z,+,1}$ and $e_{z,-,2}$ are canceled by each other in the circulation integrals.

5.2.3 Divergence-Free Preserving Prolongation

Lastly, the divergence-free constraint at the coarse cell must be preserved at each refinement step. This whole regridding procedure from the parent mesh solution to the child mesh solution is called *prolongation*. In FLASH and PARAMESH, several different interpolation methods can be used for prolongation. By default, PARAMESH uses a linear interpolation to fill the cell-centered variables for newly created blocks. In MHD, such interpolations are also in need for the face-centered magnetic field variables. A careful choice should be made, however, for the magnetic fields because an interpolation such as a linear interpolation scheme will not preserve the divergence-free property for the field variables at refinement. As a result, one definitely loses the most important constraint in the whole MHD simulations.

To accomplish this requirement, we adopt a straightforward (and the simplest) approach in that each prolongation results in the direct injection interpolation for the fields variables in new children blocks. The divergence-free fields at the cell face centers of the parent blocks are subject to be injected directly to the cell face centers of the new children blocks. This will maintain the divergence-free property inside the grid block. Two other switches such as `AMR_PROLONG_FC_DIVBCONSIST` and `DIVERGENCE_FREE` also must be declared in `PARAMESH_PREPROCESSOR.FH` in PARAMESH to resolve possible non-zero divergence in the adjacent cells.

Balsara [10, 11] has studied a new algorithm to guarantee the divergence-free property over a given computational grid, which naturally can be extended to each prolongation step (e.g., see equations (4.30) and (4.31)). He proposed the quadratic

polynomial approach that provides the divergence-free field reconstruction everywhere at the grid cells. Balsara's scheme has not been adopted in this dissertation, yet such implementation will remain in the future work.

5.3 Boundary Condition Via Guard Cell Exchange

In parallel/AMR computation, a boundary condition is imposed by using the guard cell filling and exchange strategy. The boundary conditions needed to update interior cells are stored in the guard cells. The boundary conditions of the fine grid are defined by either external boundary conditions, or adjacent sibling blocks, or both, or interpolations from the coarse parent grid to the fine child grid. The number of guard cells is determined by the order the interpolation schemes and stencils a given scheme take. For example, the explicit hydrodynamics solver with PPM algorithm takes four guard cells in each direction.

In the USM-IEC-SDDA implementations, as seen in Chapter 3, the IEC scheme with the central differencing requires two guard cells in each direction, whereas three guard cells are required if the scheme uses the upwinding scheme. It is easy to see the extra amount of guard cell exchanges due to the extra number of guard cells. For instance, let use consider a simple d-dimensional case with N interior cells with NG guard cells in each direction. The total number of guard cell exchanges required per block is then $(N + 2NG)^d - N^d$, while having extra NG_α guard cells yields $(N + 2NG + 2NG_\alpha)^d - N^d$ many guard cell exchanges. Assuming there are $NVAR$ variables to be exchanged, then, in general, the extra guard cell

exchanges one should perform per each block becomes

$$\frac{(N+2NG+2NG_\alpha)^d - N^d}{(N+2NG)^d - N^d} \times NVAR. \tag{5.3}$$

One would also require double precision for each variable, for which 8 bytes of memory space should be taken. Now to see the final outcome, one further assumes that periodic boundary conditions are imposed in all directions, so that the guard cell exchanges are performed for all $NBLOCKS$ number of blocks in all direction. Then the total extra amounts of data that should be exchanged by parallel inter-communication between processors per one time step (assuming only one guard cell exchange is called per each time step) are

$$\frac{(N+2NG+2NG_\alpha)^d - N^d}{(N+2NG)^d - N^d} \times NVAR \times NBLOCKS \times 8\text{bytes}. \tag{5.4}$$

Notice that if there is an refinement level increase between time steps, then the above will further be increased by a factor of up to 2^d in an extreme case (i.e., all blocks are refined).

To quantify this factor, consider a typical parallel AMR choice with $N = 10, NG = 2$. The values of the factor $\frac{(N+2NG+2NG_\alpha)^d - N^d}{(N+2NG)^d - N^d}$ in (5.3) as a function of NG_α and d are compared in Table 5.1.

In the above example, therefore, using the central scheme in the IEC is 1.625 times cheaper computationally than using the upwinding scheme in two-dimensional problems. Also, the USM-IEC-SDDA MHD solver will be 2.333 times more efficient than that of any PPM based solver, at least, in terms of the guard cell exchange strategy.

Factor comparison			
	$d = 1$	$d = 2$	$d = 3$
$NG_\alpha = 1$	1.500	1.625	1.775
$NG_\alpha = 2$	2.000	2.333	2.771

Table 5.1: Extra amount of work for guard cell exchanges as a function of extra number of guard cells in each dimension. This simple example compares impacts of parallel communications with schemes using guard cells of 2, 3, and 4 for each direction in different dimensional problems.

In the next chapter, various results obtained by using the USM-IEC-SDDA scheme will be discussed.

Chapter 6

NUMERICAL RESULTS OF USM-IEC-SDDA

My goal is simple.

It is complete understanding of the universe,

why it is as it is and why it exists at all.

Stephen Hawking

Validation studies of the USM-IEC-SDDA scheme have been made in a suite of several 1D and 2D MHD test problems. A series of numerical studies show that the scheme is second-order accurate, and maintains the solenoidal constraint of magnetic fields up to round-off error. Numerical issues in simulating MHD problems and the relevance of the USM-IEC-SDDA implementation will be discussed in the chapter.

All simulations are performed using Courant numbers between 0.5 (2D) and 0.8 (1D), depending on the problem considered.

6.1 1D Results

In MHD problems in one-dimension, the normal component of the magnetic fields is treated as a constant because of the divergence-free constraint. This makes one-dimensional MHD problems simple, for which no efforts of preserving the divergence-free property is required.

6.1.1 Brio-Wu MHD Shock Tube

The 1D test problem consists of testing the Brio-Wu MHD shock tube problem [20] on the computational domain $[0, 1]$. This problem is an MHD version of the hydrodynamical Sod's shock tube problem in the presence of non-zero values of the magnetic fields. In this problem the Roe averages formulated in [20] are applied, as the Brio-Wu problem is of the $\gamma = 2$ plasma flow. For this problem, the USM-IEC-SDDA test results are compared with the solutions from the eight wave scheme in FLASH. The problem takes the outflow boundary conditions with the initial condition given by

$$B_x = 0.75, \tag{6.1}$$

$$(\rho, u, v, w, B_y, B_z, p)^T = \begin{cases} (1, 0, 0, 0, 1, 0, 1)^T & \text{for } x < \frac{1}{2}, \\ (0.125, 0, 0, 0, -1, 0, 0.1)^T & \text{for } x > \frac{1}{2}. \end{cases} \tag{6.2}$$

That there is no need to consider any divergence-free treatment for this problem, one can turn off the switches for the IEC and SDDA schemes and the whole USM-IEC-SDDA scheme reduces to a typical cell-centered Godunov type solver. The staggered algorithm is not required to be adopted.

In plots illustrated in figure 6.1, the USM scheme compares well with the eight wave scheme. One of the interesting features of simulating the Brio-Wu problem is to see five different MHD waves. In this high resolution case utilizing 800 cells over the domain, the USM code accurately produces solutions that reflect complicated MHD wave structures. For example, in the density plot, all five MHD waves are indicated clearly, and they are, respectively, from left to right: a fast rarefaction wave, a compound wave, a contact discontinuity, a slow shock and a fast rarefaction

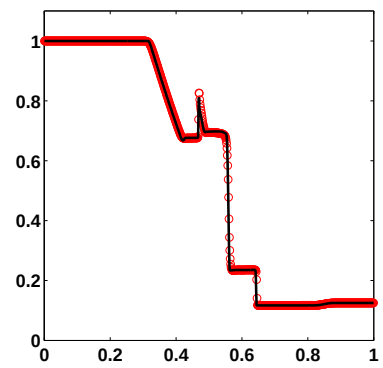

(a) Density

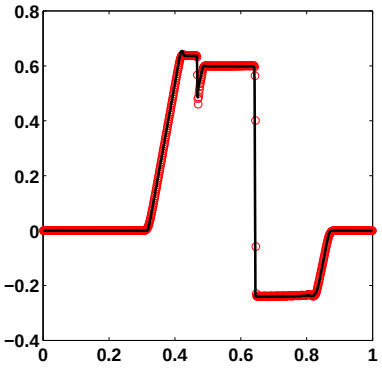

(b) x component velocity

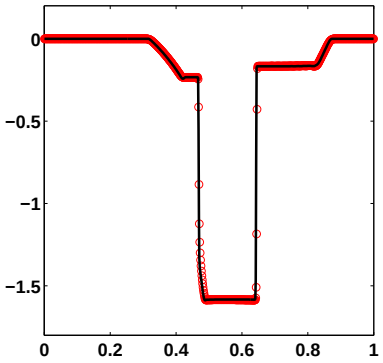

(c) y component velocity

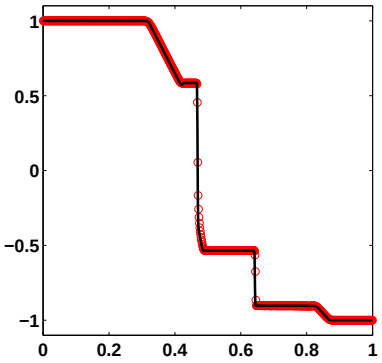

(d) y component magnetic field

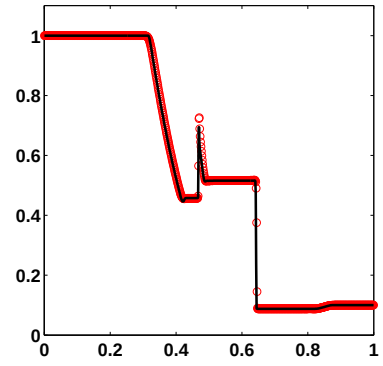

(e) Gas pressure

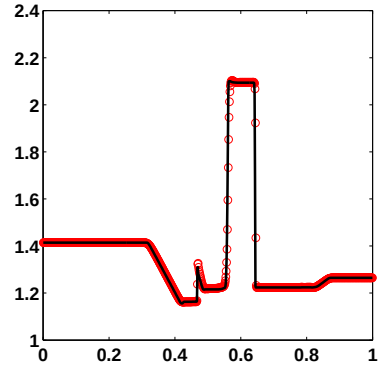

(f) Mach number

Figure 6.1: 1D Brio-Wu MHD shock tube problem. The USM results (red dots) are compared with the eight wave scheme results (black lines) on an 800 resolution.

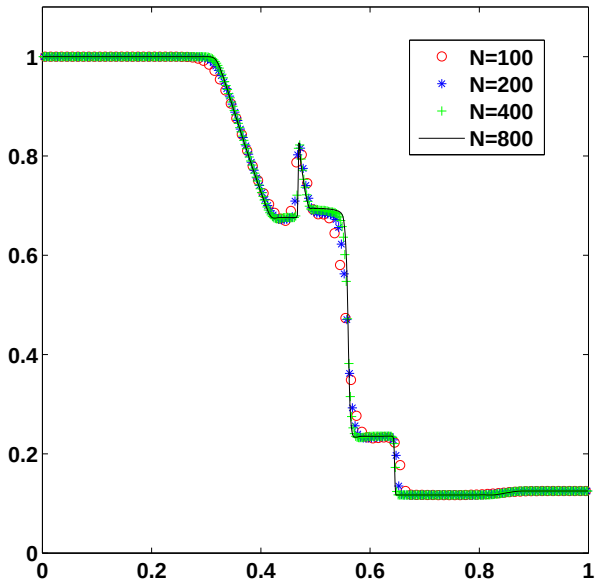

(a) Grid resolution test

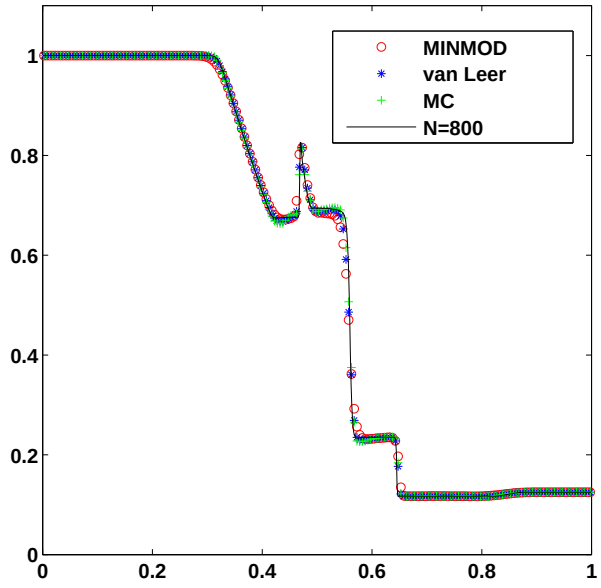

(b) Slope limiter test

Figure 6.2: Various tests in 1D Brio-Wu MHD shock tube problem.

waves. The compound wave structure is captured accurately, which involves shock and rarefaction waves of the same family moving together.

Shown in figure 6.2, two parameter tests have been performed, including (a) a grid resolution test and (b) a slope limiter test. In figure (a), solutions on four different domains of size $N = 100, 200, 400, 800$ are compared using MINMOD limiter. The density is a good choice for this matter because it carries all five different MHD waves. One can also take the highest resolution solution of size $N = 800$ as a customary choice for a reference (or *true*) solution, as there is no analytical solution available for this test problem. As expected, comparisons of solutions on coarse grids ($N = 100, 200$) with solutions on finer grids ($N = 400, 800$) confirm that a great deal of solution accuracy can be improved by increasing the grid resolution.

In figure (b), different slope limiters are tested for the density over 200 cells in x-direction. They are MINMOD, van Leer's, and MC (Monotonized Central-difference) limiters. It is apparent that MC limiter produces slight undershoot and overshoot in the solution near $x \approx 0.4$ and $x \approx 0.55$, respectively, which result from the limiter's inherent nature of a discontinuity-enhancing gradient function (LeVeque, 1997). Same phenomena are also observed from the eight wave solutions in figure 6.1–(a), even with using a high resolution of a size $N = 800$. Such behaviors are shown to be removed by using a less aggressive limiter, e.g., MINMOD or van Leer's limiter. These two limiters, however, give more diffusive solutions of other discontinuities, yet a use of high resolution will resolve this issue.

6.1.2 1D Accuracy Study

The solution convergence rate for the Brio-Wu problem is now examined in this section. Following Tóth [88], the relative numerical error of any arbitrary variable W obtained on an N grid can be calculated as,

$$Err = \frac{\sum_{i=1}^{N} |W_i - W_i^{\text{high}}|}{\sum_{i=1}^{N} |W_i^{\text{high}}|}, \tag{6.3}$$

where W^{high} is a coarsened high resolution solution. For example, when a solution on 800 cells is coarsened to a solution on 100 cells, solutions on every 8 cells are averaged in a finite volume sense.

For display in figure 6.3, the density is chosen for W. A high resolution solution of $N = 1600$ is coarsened to solutions of size $N = 100, 200, 400, 800$, with which the computed results of size $N = 100, 200, 400, 800$ are compared, respectively.

As shown in figure 6.3, the USM scheme generates a faster convergence rate (faster than the first-order convergence) as the resolution is increased. The overall convergence rate is approximately linear, although the scheme is a second-order accurate scheme. This is not surprising, since the order of accuracy of a method applies only to smooth flow and not to flows containing discontinuities. In fact, all modern shock capturing schemes are only first-order accurate in the vicinity of discontinuities, because a fully limited second-order scheme would reduce to a first-order scheme in regions of discontinuities.

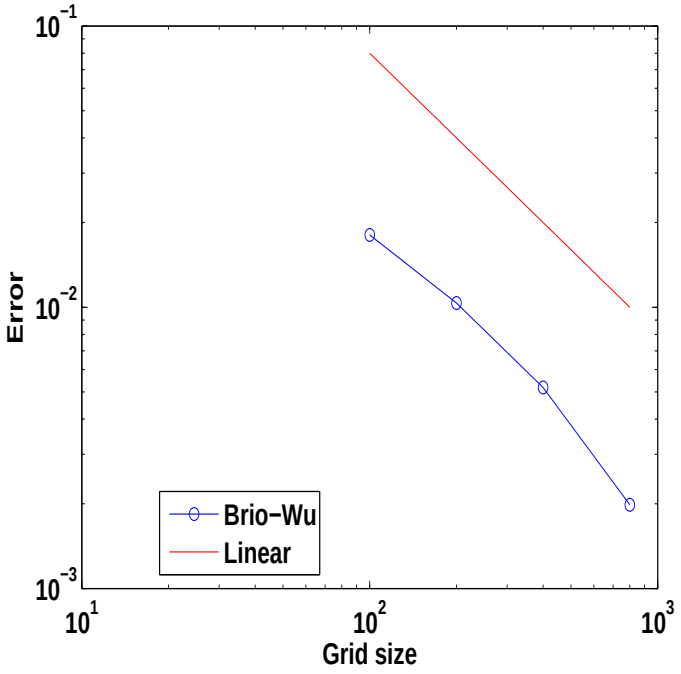

Figure 6.3: A convergence rate test for the Brio-Wu problem using the USM scheme. A linear slope is given as a reference. A convergence rate is shown to be accelerated by increasing the resolution.

6.2 2D Results

The results of several 2D MHD test problems are discussed in this section. The CFL number of 0.5 is chosen for stability in all test cases. Throughout multi-dimensional cases herein, both switches of the IEC and SDDA schemes have been turned on, as well as fully utilizing the multidimensional characteristic method in the data reconstruction-evolution step. Their roles will be carefully pointed out and shown to be of great important.

6.2.1 Field Loop Problem

The first test is the field loop problem [37] which has been considered to be one of the severe test cases in multidimensional MHD. This test problem considers two different set-ups of a weakly polarized magnetic field loop: the loop is either being advected with the flow or being held to be stationary. The first set-up of the advection case is much harder to achieve than the second case, the diffusion test, in a sense that it is harder to maintain the circular shape of the advecting field loop along the computational domain during the whole computation time. In the second diffusion test, the only dynamics is the numerical diffusion and hence it is easy to see how much the scheme is diffusive. In both cases, an insufficient amount of numerical dissipation will distort the circular shape of the field loop.

This problem is taken from Gardiner & Stone [37, 82]. The computational domain is $[-1, 1] \times [-0.5, 0.5]$, resolved on a size 256×148, with a doubly periodic boundary condition. The density and pressure are set to unity everywhere. The

velocity fields are defined as,

$$\mathbf{U} = u_0(\cos\theta, \sin\theta, 0) \tag{6.4}$$

with the advection angle θ, given by $\theta = \tan^{-1}(0.5) \approx 26.57°$. The choices for the initial velocity were set as $u_0 = 0$ for the diffusion test and $u_0 = \sqrt{5}$ for the advection test. The size of domain and other parameters are chosen in such a way that, for the advection case, the weakly magnetized field loop will make one complete orbit cycle by $t = 1$. To initialize $\nabla \cdot \mathbf{B} = 0$ numerically, the components of the magnetic field values are obtained by taking the numerical curls of the z-component of the magnetic vector potential A_z:

$$A_z = \begin{cases} A_0\,(R - r) & \text{if} \quad r \le R, \\ \\ 0 & \text{otherwise} \end{cases}, \tag{6.5}$$

and

$$B_{x,i,j} = \frac{A_{z,i,j+1} - A_{z,i,j-1}}{2\Delta y}, \quad B_{y,i,j} = -\frac{A_{z,i+1,j} - A_{z,i-1,j}}{2\Delta x}. \tag{6.6}$$

By using this initialization process, one can start with divergence-free magnetic fields that give a maximum value of $\nabla \cdot \mathbf{B}$ on the order of 10^{-16}. The parameters in (6.5) are $A_0 = 10^{-3}, R = 0.3$ with a field loop radius r. This initial condition results in a very high beta plasma $\beta = 2p/B^2 = 2 \times 10^6$ for the inner region of the field loop. Inside the loop the magnetic field strength is very weak and the flow dynamics is dominated by the gas pressure.

The first test for the advection case can be solved to final time $t = 2$ with a Courant number of 0.5. The advection test truly requires the full multidimensional MHD consideration, i.e., the inclusion of the multidimensional terms (2.18) and

(2.19) as described in Chapter 2. Since the field loop is being advected with an oblique angle to the x-axis of the computational domain, the values of $\partial B_x/\partial x$ and $\partial B_y/\partial y$ are non-zeros in general, and these terms together with the multidimensional terms $\mathbf{A}_{B_x}, \mathbf{A}_{B_y}$ should be included properly.

The dynamics of the flow advects the field loop with the advection angle to the grid. During the evolution of the advection process a good numerical scheme must maintain the circular symmetry at all time. The lack of numerical dissipation will result in spurious oscillations at the loop and will break the circular symmetry. In figure 6.4 the initial conditions of the current density, magnetic field lines (the 20 contour lines of A_z are shown), and magnetic pressure are illustrated. As for the default value, the SDDA scheme (4.20) and (4.21) with a choice of $\nu = 0.5$ is adopted and the IEC central differencing scheme is used.

From the results in figure 6.5, the USM-IEC-SDDA scheme maintains the circular shapes of the flow geometry extremely well to the final time step. The first image of the current density $\mathbf{j}$ is the curl of the field components and is very sensitive to oscillations in the field components. The USM-IEC-SDDA scheme successfully preserves the initial circular symmetry without suffering any oscillations. In the second plot (b) it is clear that the 20 field lines are still present in the final solution, keeping the original circular symmetry very well. There is only a slight dissipation at the inner most center, which leads to disappearance of the smallest circular field line. The final result (c) of the magnetic pressure $B_p = (B_x^2 + B_y^2)/2$ is also compared well with the results of Gardiner *et al.* [37]. The results obtained here have led to conclude that the anti-dissipation control in the SDDA scheme plays an

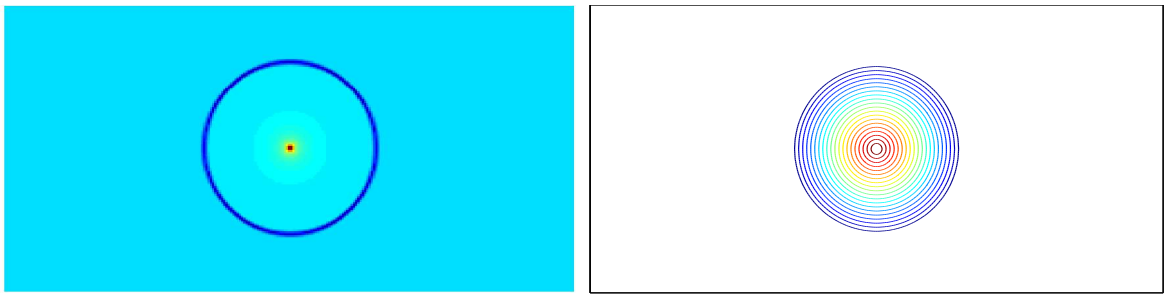

(a) Current density at $t = 0$

(b) Magnetic field lines at $t = 0$

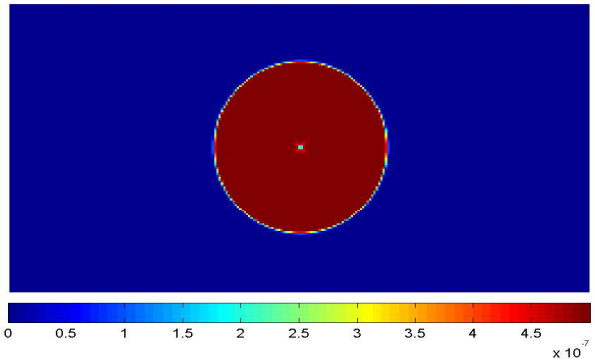

(c) Magnetic pressure at $t = 0$

Figure 6.4: The initial conditions of the field loop advection problem on a 256×148 resolution.

essential role to achieve correct amounts of numerical dissipation in the magnetic field components.

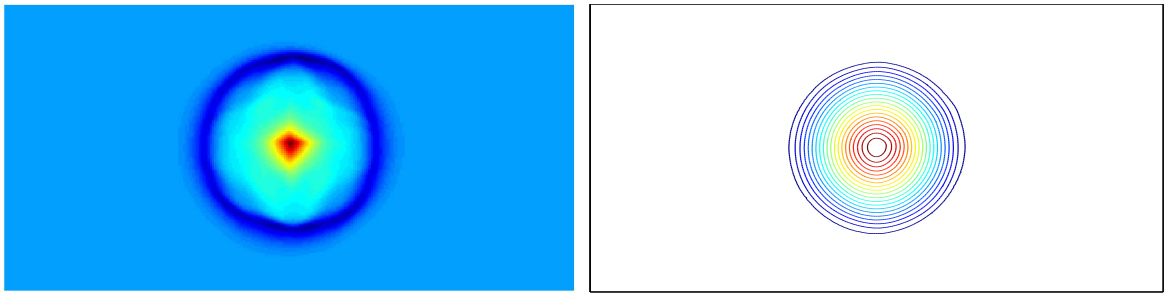

(a) Current density at $t = 2$

(b) Magnetic field lines at $t = 2$

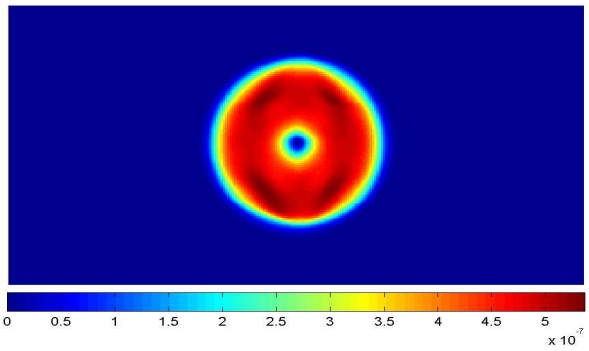

(c) Magnetic pressure at $t = 2$

Figure 6.5: The field loop advection problem at time $t = 2$. The value $\nu = 0.5$ is used.

To further amplify the role of the SDDA treatment, the results obtained without turning on the SDDA switch ($\nu = 0$) is presented in figure 6.6. In plot (b) the magnetic pressure already suffers from strong oscillations over the entire loop even at relatively earlier time $t = 0.2$. Notice also that the magnitude of the magnetic pressure has been increased by an order of 10^{-1}, as a consequence of the absence of

anti-dissipation control in the scheme. The final solution in (c) is quite disastrous, leaving no trace of the initial circular shape. The magnitude has reached up to 0.12 which is an order of 10^7 larger than the initial value (See the initial magnitude in (c) in figure 6.4.)

It is preferable to see an effect of the value ν for the SDDA scheme. Let us now consider the same advection problem using the maximum possible value of $\nu = 1$. This larger value clearly gives more dissipation that prevents further growth of the magnetic field components. However, since the SDDA scheme employs the electric field value E_z from the previous time step, the dynamics of the magnetic fields is coupled with the behavior of the previous time step solution. This phenomenon is seen in figure 6.7–(a) that the original circular shape evolved to an oval shape along the direction of the advection. From this test it is desirable to set the value to $\nu = 0.5$ as the default choice.

In (b), one can see the result of using the upwinded differencing algorithm for the IEC scheme. As was asserted in Chapter 3, the effect of upwinding the electric field does not seem to improve any qualitative behavior of the solution.

The diffusion test is now considered, where the magnetic field loop remains stationary in the domain. The only dynamics of the simulation is the numerical dissipation and it diffuses the shape of the flow. In figure 6.8 one can observe that the USM-IEC-SDDA scheme maintains the circular shape of the flow variables only allowing correct amounts of minimum possible dissipation. The small hole in the magnetic pressure reflects the small amount of diffusion that has occurred in the scheme. Indeed, the final solutions in the diffusion test are quite equivalent as the

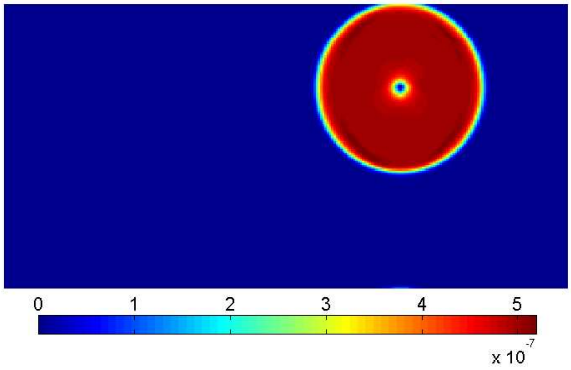

(a) Magnetic pressure at $t = 0.2$ with SDDA

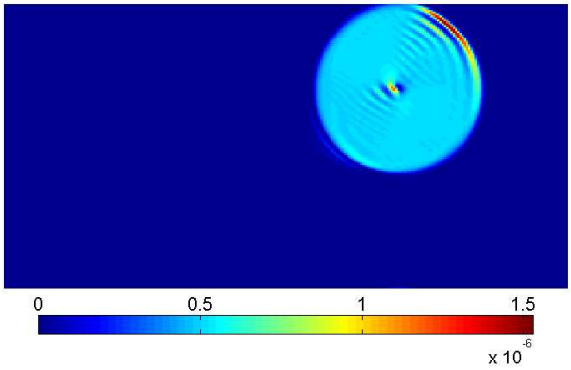

(b) Magnetic pressure at $t = 0.2$ without SDDA

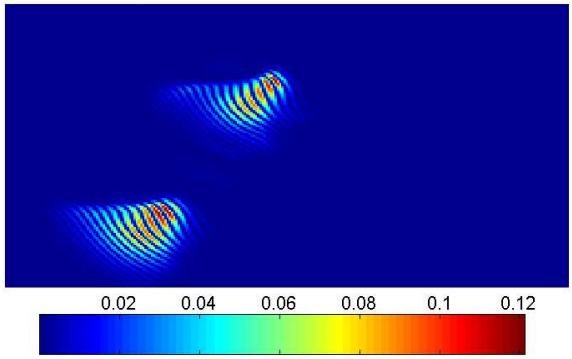

(c) Magnetic pressure at $t = 2$ without SDDA

Figure 6.6: Effect of the SDDA on the field loop advection test.

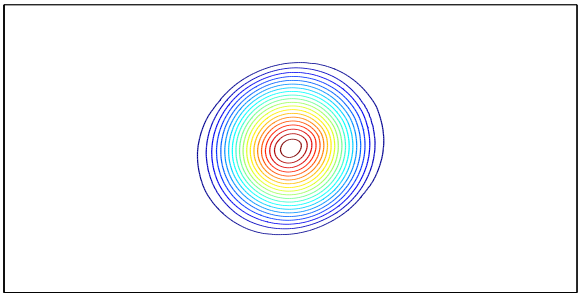

(a) Magnetic field lines at $t = 2$ with $\nu = 1$

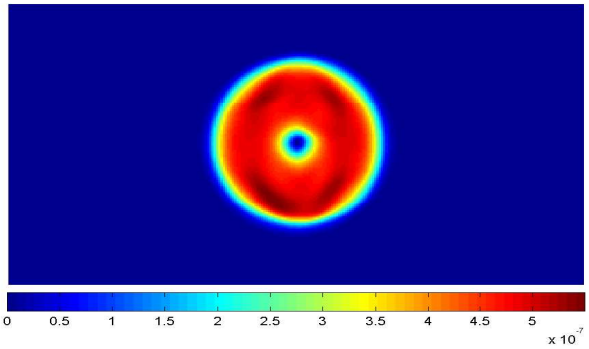

(b) Magnetic pressure at $t = 2$ using the upwinding scheme in IEC

Figure 6.7: A parameter test for ν is shown in (a). The larger value $\nu = 1$ tends to disrupt the circular shape of the magnetic field lines at time $t = 2$. In (b), another test using the upwinding scheme in the IEC is also illustrated.

initial solutions, proving that the USM-IEC-SDDA scheme works absolutely well in controlling anti-dissipation phenomena of the scheme.

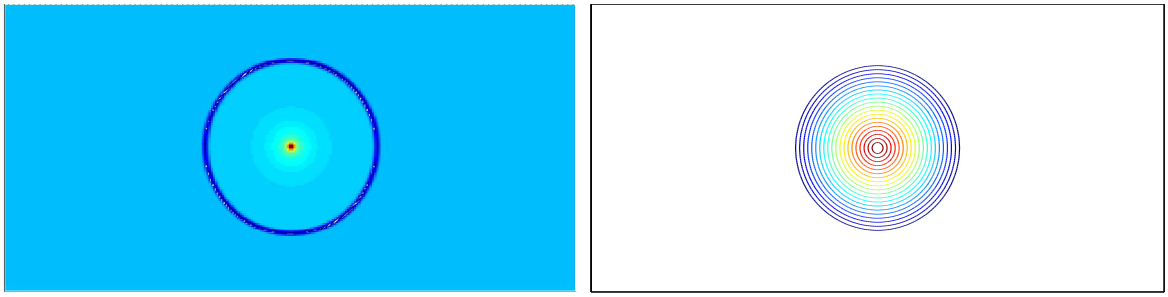

(a) Current density at $t = 2$ (b) Magnetic field lines at $t = 2$

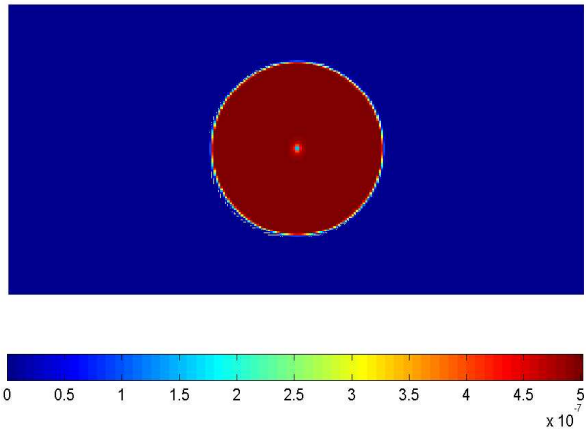

(c) Magnetic pressure at $t = 2$

Figure 6.8: The first field loop diffusion problem on a 256×148 resolution. The solutions at time $t = 2$ are presented.

The last case in the field loop problem considers another diffusion case which will help to understand the in-plane geometry in two-dimension. For two-dimensional MHD flows, it is important to maintain the relevant in-plane flow properties. To see

this, one would like to consider a variant of the previous diffusion problem, where the velocity fields can now be set as

$$\mathbf{U} = (0, 0, 1). \tag{6.7}$$

With this condition, one can see how the in-plane dynamics is influenced by $\nabla \cdot \mathbf{B}$. It has been already seen in the previous diffusion test that the in-plane diffusion of the magnetic field is essentially negligible. Hence, on each subsequent time step the $\nabla \cdot \mathbf{B}$ error will be unchanged between time steps. This will of course proceed until B_z becomes sufficiently large to influence the in-plane dynamics. To see this, let us look at the induction equation for B_z component:

$$\frac{\partial B_z}{\partial t} + B_z \frac{\partial u}{\partial x} - B_x \frac{\partial w}{\partial x} - w \frac{\partial B_x}{\partial x} + u \frac{\partial B_z}{\partial x} + B_z \frac{\partial v}{\partial y} - B_y \frac{\partial w}{\partial y} - w \frac{\partial B_y}{\partial y} + v \frac{\partial B_z}{\partial y} = 0. \tag{6.8}$$

Notice that the fourth and eighth terms in the above equation (6.8) are the multidimensional terms that have been taken care of in the data reconstruction-evolution step. The terms have been treated in an unsplit fashion using the multidimensional characteristic method without applying any limiting (See equation (2.29)). The sum of these two terms is $w\nabla \cdot \mathbf{B} = w(\Delta B_{x,i}/\Delta x + \Delta B_{y,j}/\Delta y)$, and hence if there is any secular growth in the $\nabla \cdot \mathbf{B} = (\Delta B_{x,i}/\Delta x + \Delta B_{y,j}/\Delta y)$ error, it will change the in-plane geometry due to an unphysical growth of B_z with a rate proportional to $\Delta t w \nabla \cdot \mathbf{B}$. For dimensionally splitting MHD schemes, therefore, this kind of undesirable situations are hard to be avoided, since the terms $\Delta B_{x,i}/\Delta x$ and $\Delta B_{y,j}/\Delta y$ are not calculated simultaneously.

Figure 6.9 shows two results obtained in the USM-IEC-SDDA scheme at the final time step $t = 2$. The first plot in (a) is the numerical values of $\nabla \cdot \mathbf{B}$ and the

second plot in (b) is the z component of the magnetic fields. The 30 contour lines were plotted in both cases, where the results seem to be no more than noise plots. One can see that both the values of the divergence of the magnetic fields and B_z are in the range of orders of 10^{-15}. These two results clearly show that the USM-IEC-SDDA scheme does correctly maintain the in-plane geometry without causing any unphysical phenomena.

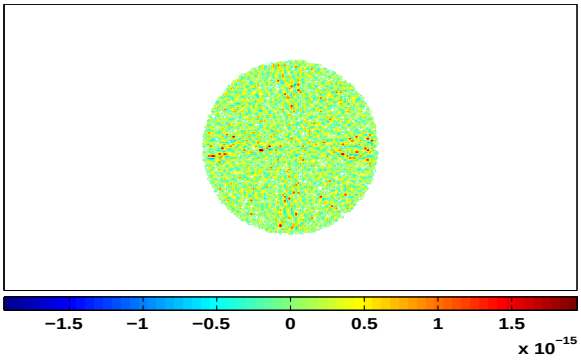

(a) $\nabla \cdot \mathbf{B}$

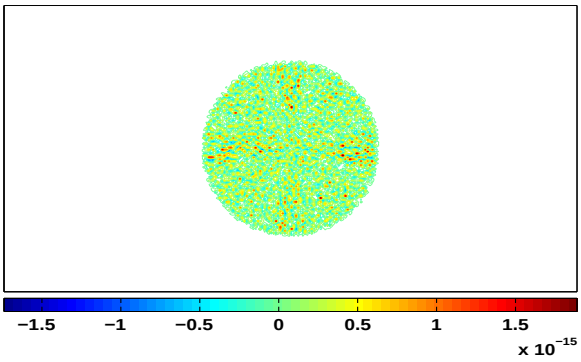

(b) B_z

Figure 6.9: The second diffusion problem of the field loop at $t = 2$. The numerical values of the divergence of the magnetic fields and the z component field are shown.

6.2.2 Orszag-Tang Problem

The second test problem is the Orszag-Tang MHD vortex problem [65]. This test problem has been used in many papers and served as a good validation test for two-dimensional MHD codes. The computational domain is $[0,1] \times [0,1]$, with a resolution of $N \times N$. The initial condition is given by smooth sinusoidal wave structures,

$$\mathbf{U} = u_0(-\sin\pi y, \sin 2\pi x, 0), \tag{6.9}$$

$$\mathbf{B} = B_0(-\sin\pi y, \sin 4\pi x, 0). \tag{6.10}$$

where B_0 is chosen so that the ratio of the gas pressure to the rms magnetic pressure is equal to 2γ, where $\gamma = 5/3$. The initial density, the speed of sound and u_0 are set to unity, therefore, both the initial pressure and B_0 are set to $1/\gamma$. Periodic boundary conditions are used for both boundaries. The final solutions are obtained at time $t = 0.5$. The mixed type of the slope limiter (MINMOD+MC) was adopted as described in Chapter 2.

The density plot on a 400×400 grid size at the final time $t = 0.5$ is shown in figure 6.10–(a). The density plot shows that the initially smooth flow has been developed into an increasingly complicated structure involving many discontinuous features.

The solution accuracy study of the USM-IEC-SDDA scheme is conducted and shown in (b). The convergence rate test uses the 2D version of the relative error

which can be defined in the similar fashion as in 1D (6.3), viz.,

$$Err = \frac{\sum_{j=1}^{M}\sum_{i=1}^{N}|W_{i,j} - W_{i,j}^{\text{high}}|}{\sum_{j=1}^{M}\sum_{i=1}^{N}|W_{i,j}^{\text{high}}|}. \tag{6.11}$$

Figure 6.10–(b) shows that the convergence rate of the USM-IEC-SDDA scheme is faster than the rates obtained from other MHD algorithms with lower values of error. Two compared results are the convergence rates of the projection based MHD solver and Balsara & Spicer's flux-CT scheme, obtained from a table-lookup in Tóth [88]. Similarly as before, the solution on a high resolution of size 400×400 is coarsened to solutions of sizes $50 \times 50, 100 \times 100, 200 \times 200$ to compute the convergence rates of these three different size solutions. Two different convergence rates of the USM-IEC ($\nu = 0$) and USM-IEC-SDDA ($\nu = 0.5$) are also compared.

Tóth has concluded in [88] that the projection scheme and the Balsara-Spicer's flux-CT scheme are the two most accurate schemes among many other MHD schemes he tested. This convergence test supports that the current USM scheme can generate even faster convergence rate with noticeably lower errors. In both cases of USM-IEC and USM-IEC-SDDA, the slopes connecting 100×100 and 200×200 tend to be dropped with faster rates, indicating a better convergence rate of the current MHD solver. There is also an improvement in the convergence rate by turning on the SDDA switch.

Finally in figures 6.11 two different results of $\nabla \cdot \mathbf{B}$ from the numerical divergences calculated from (a) the USM-IEC-SDDA scheme and (b) the eight wave scheme are compared. Clearly, very small errors in the numerical values of $\nabla \cdot \mathbf{B}$ are seen in (a), whereas the non-zero quantities are dominant from the eight wave

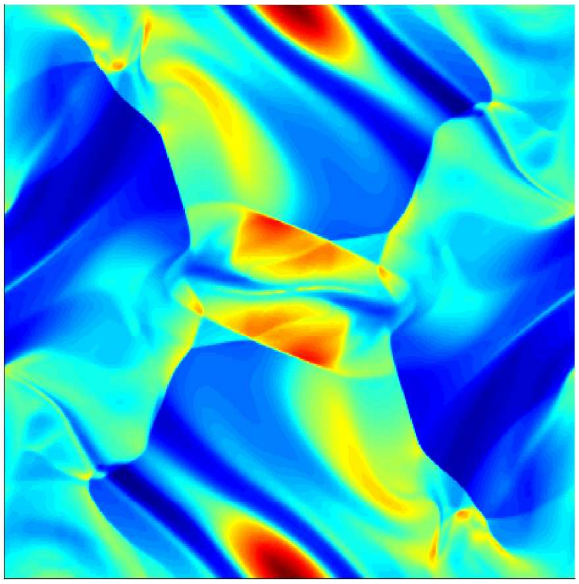

(a) Density plot at $t = 0.5$

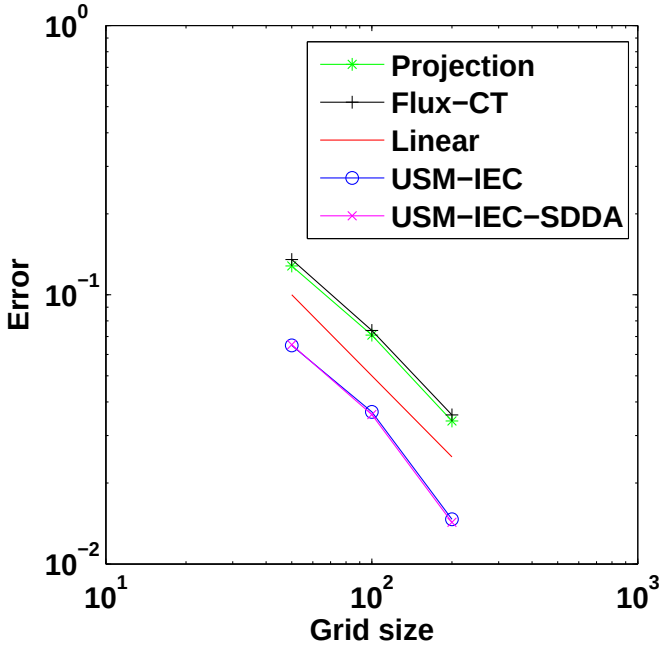

(b) Convergence rate

Figure 6.10: The density plot (a) at $t = 0.5$ on a high resolution 400×400. A comparison of the convergence rates for the Orszag-Tang problem is shown in (b).

calculation in (b).

The numerical values of $\nabla \cdot \mathbf{B}$ from the eight wave calculation are shown to be non-zero finite values, ranging from negative to positive. The USM-MHD scheme, however, maintains $\nabla \cdot \mathbf{B} = 0$ up to orders of 10^{-12} errors over the simulation time. One can see in (b) that the locations of non-zero values of $\nabla \cdot \mathbf{B}$ and the discontinuities of the solution are quite identical. (See figure 6.10–(a)). This indicates that the eight wave scheme poorly resolves the divergence-free constraint near discontinuities. This is in contrast with the USM-IEC-SDDA scheme, which preserves the divergence-free constraint extremely well allowing $\nabla \cdot \mathbf{B}$ upto the order of 10^{-12} as illustrated in (a).

6.2.3 Rotor Problem

The next test to consider is the rotor problem which was originally studied by Balsara & Spicer [9], and also by many others [11, 55, 56, 60, 88]. This model problem is to study the onset and propagation of strong torsional Alfvén waves, which is thereby relevant for star formation.

The computational domain is a unit square $[0, 1] \times [0, 1]$ with non-reflecting boundary conditions on all four sides. The initial conditions are given by

$$\rho(x, y, 0) = \begin{cases} 10 & \text{for } r \leq r_0 \\ 1 + 9f(r) & \text{for } r_0 < r < r_1 \\ 1 & \text{for } r \geq r_1 \end{cases} \tag{6.12}$$

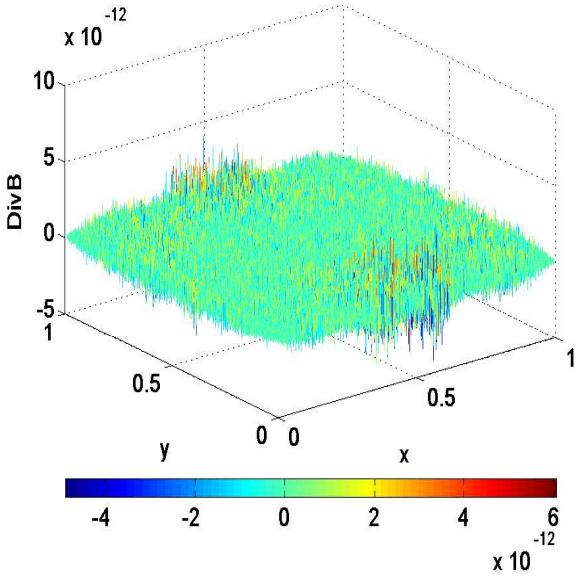

(a) $\nabla \cdot \mathbf{B}$ of USM-IEC-SDDA

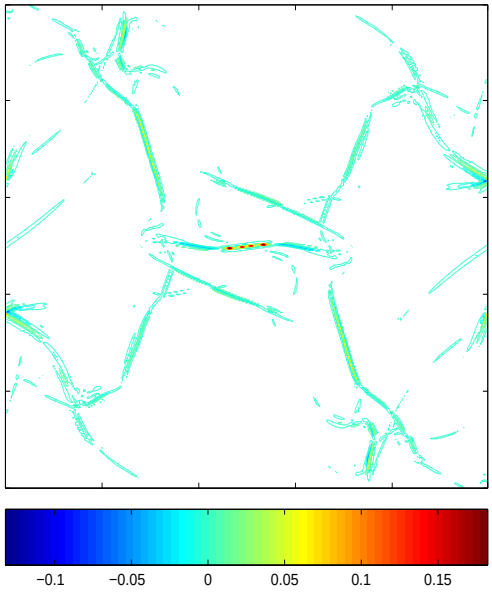

(b) $\nabla \cdot \mathbf{B}$ of eight wave

Figure 6.11: The divergence-free properties obtained from the (a) USM-IEC-SDDA scheme and (b) eight wave scheme.

$$u(x,y,0) = \begin{cases} -f(r)u_0(y-0.5)/r_0 & \text{for } r \le r_0 \\ -f(r)u_0(y-0.5)/r & \text{for } r_0 < r < r_1 \\ 0 & \text{for } r \ge r_1 \end{cases} \tag{6.13}$$

$$v(x,y,0) = \begin{cases} f(r)u_0(x-0.5)/r_0 & \text{for } r \le r_0 \\ f(r)u_0(x-0.5)/r & \text{for } r_0 < r < r_1 \\ 0 & \text{for } r \ge r_1 \end{cases} \tag{6.14}$$

$$p(x,y,0) = 1 \tag{6.15}$$

$$B_x(x,y,0) = \frac{5}{\sqrt{4\pi}} \tag{6.16}$$

$$B_y(x,y,0) = 0, \tag{6.17}$$

where $r_0 = 0.1, r_1 = 0.115, r = \sqrt{(x-0.5)^2 + (y-0.5)^2}, w = B_z = 0$ and a taper function $f(r) = (r_1 - r)/(r - r_0)$. The value $\gamma = 1.4$ is used. The initial set-up is therefore occupied by a dense rotating disk at the center of the domain, surrounded by the ambient flow at rest with uniform density and pressure. The rapidly spinning rotor is not in an equilibrium state due to the centrifugal forces. As the rotor spins with the given rotating velocity, the initially uniform magnetic field in x-direction will wind up the rotor. The rotor will be wrapped around by the magnetic field, and hence start launching torsional Alfvén waves into the ambient fluid. The angular momentum of the rotor will be diminished in later times. The circular rotor will be progressively compressed into an oval shape by the build-up of the magnetic pressure around the rotor.

Shown in figures 6.12 are the contour plots of the (a) density, (b) gas pressure, (c) Mach number and (d) magnetic pressure at the final time $t = 0.15$ on a grid resolution 400×400. By this final time, we can see in (d) that the Alfvén waves

have almost reached the boundary. For all cases (a)∼(d), the 30 contour lines were plotted. One of the important features in this rotor problem is to maintain clean and nice contour profiles at the central part of the Mach number [88]. A scheme that produces undershoots in pressure and the corresponding sound speed will result in spurious peaks in the Mach number, especially at the central region. Any signatures of such distortion of the oval contour lines can be useful to identify a poor scheme. The USM-IEC-SDDA scheme has no such spurious signatures as clearly illustrated in (c).

For a fair comparison as found in Tóth [88], the Mach number on a low 100×100 resolution was computed and presented in figure 6.13. In figure 20 of the Tóth's work, the seven different Mach numbers obtained from the seven different MHD schemes on the same resolution (100×100) were compared with each other. It is very noticeable that the result of the USM-IEC-SDDA scheme is just as superior to all the results therein. The results in figure 6.14 can be clearly compared with the plot (b) in figure 6.13 of the USM-IEC-SDDA scheme, indicating that the USM-IEC-SDDA scheme is more accurate and reliable than many other conventional MHD schemes.

In the work of Londrillo & Del Zanna [59], a similar rotor problem has been presented with minor changes in the flow parameters. They asserted that their results were convincing, however, the divergence of the magnetic fields is shown to be reached up to the order of 10^{-4} on their 240×240 calculation. The USM-IEC-SDDA scheme, however, keeps the value to orders of 10^{-12} even with a lower resolution of size 200×200. This rotor problem will also be calculated using FLASH

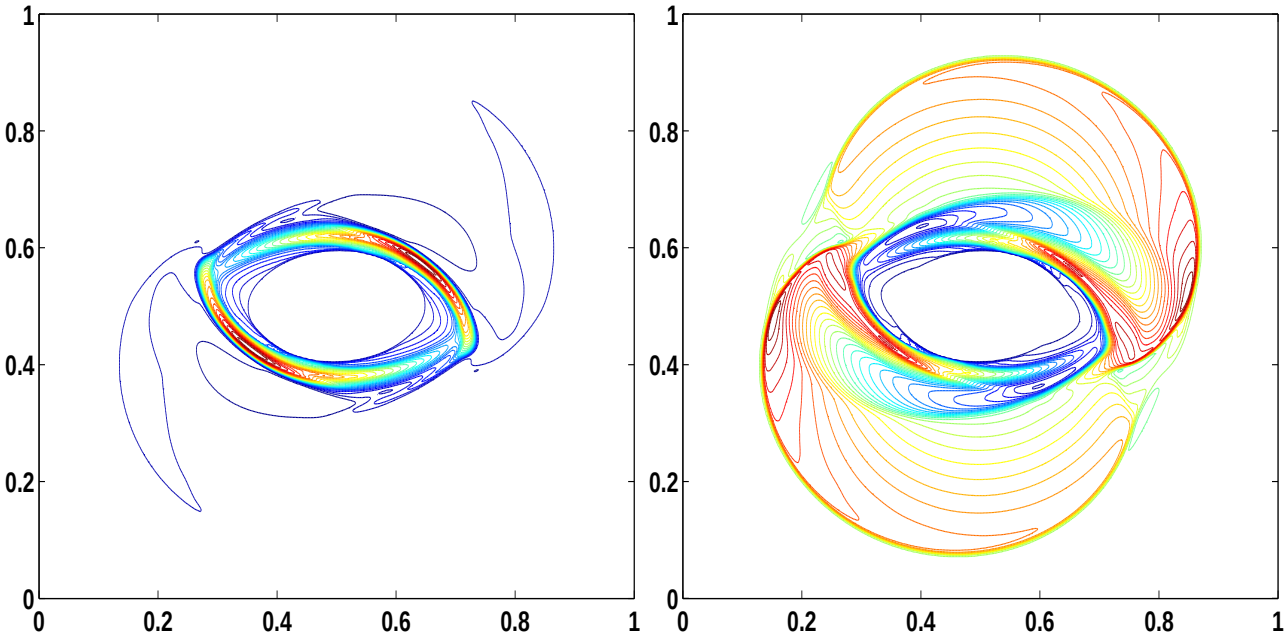

(a) Density at $t = 0.15$

(b) Gas pressure at $t = 0.15$

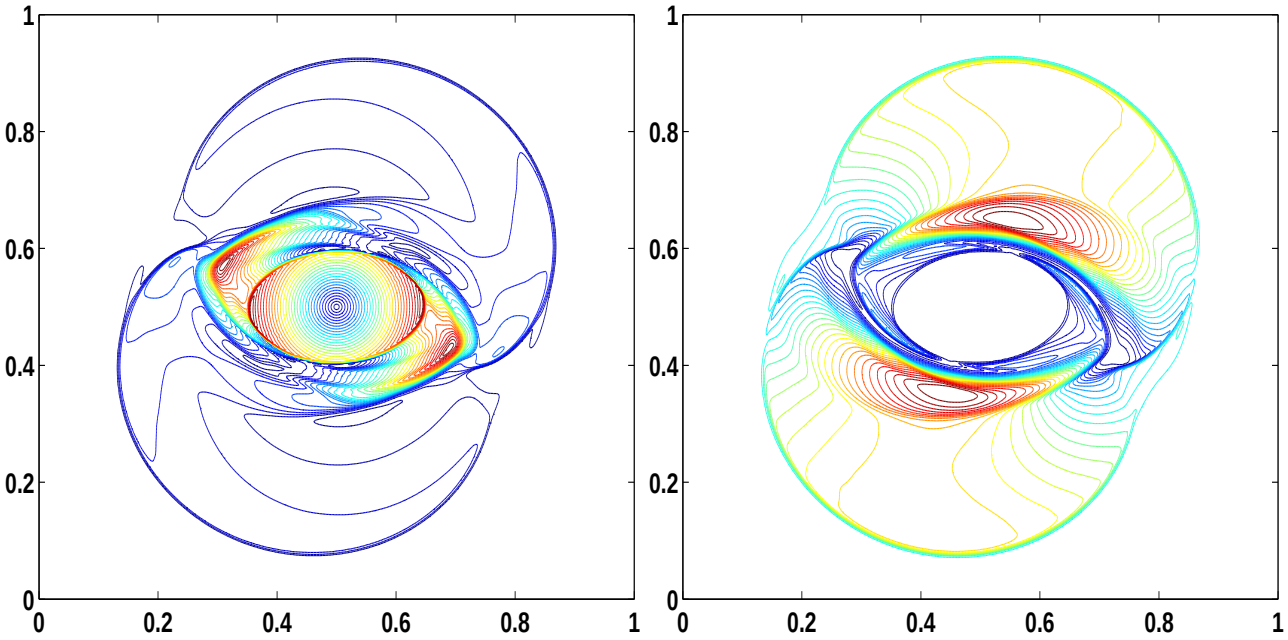

(c) Mach number at $t = 0.15$

(d) Magnetic pressure at $t = 0.15$

Figure 6.12: The rotor problem on a resolution of 400×400. The 30 contour lines are plotted.

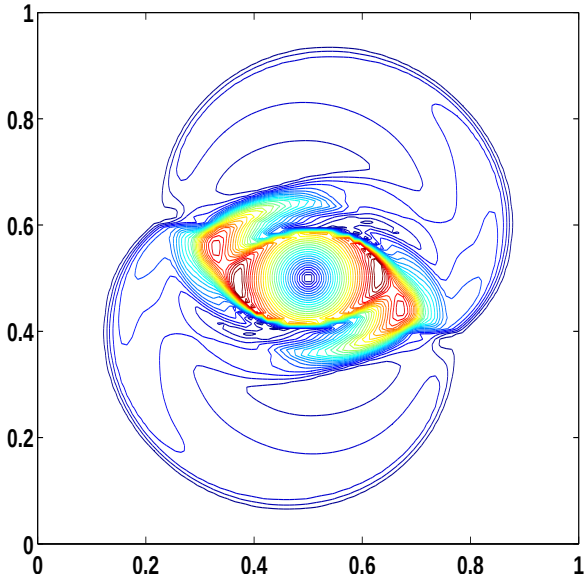

(a) Mach number at $t = 0.15$

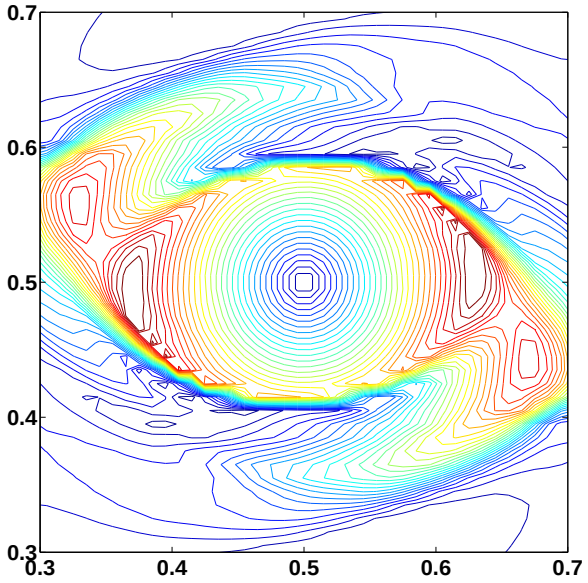

(b) A close up view at the center

Figure 6.13: The Mach number $|v|/c_s$ for the rotor problem on a resolution of 100×100. The 30 contour lines are shown. In (b) the circular shapes of the contour lines are well captured even with this low resolution.

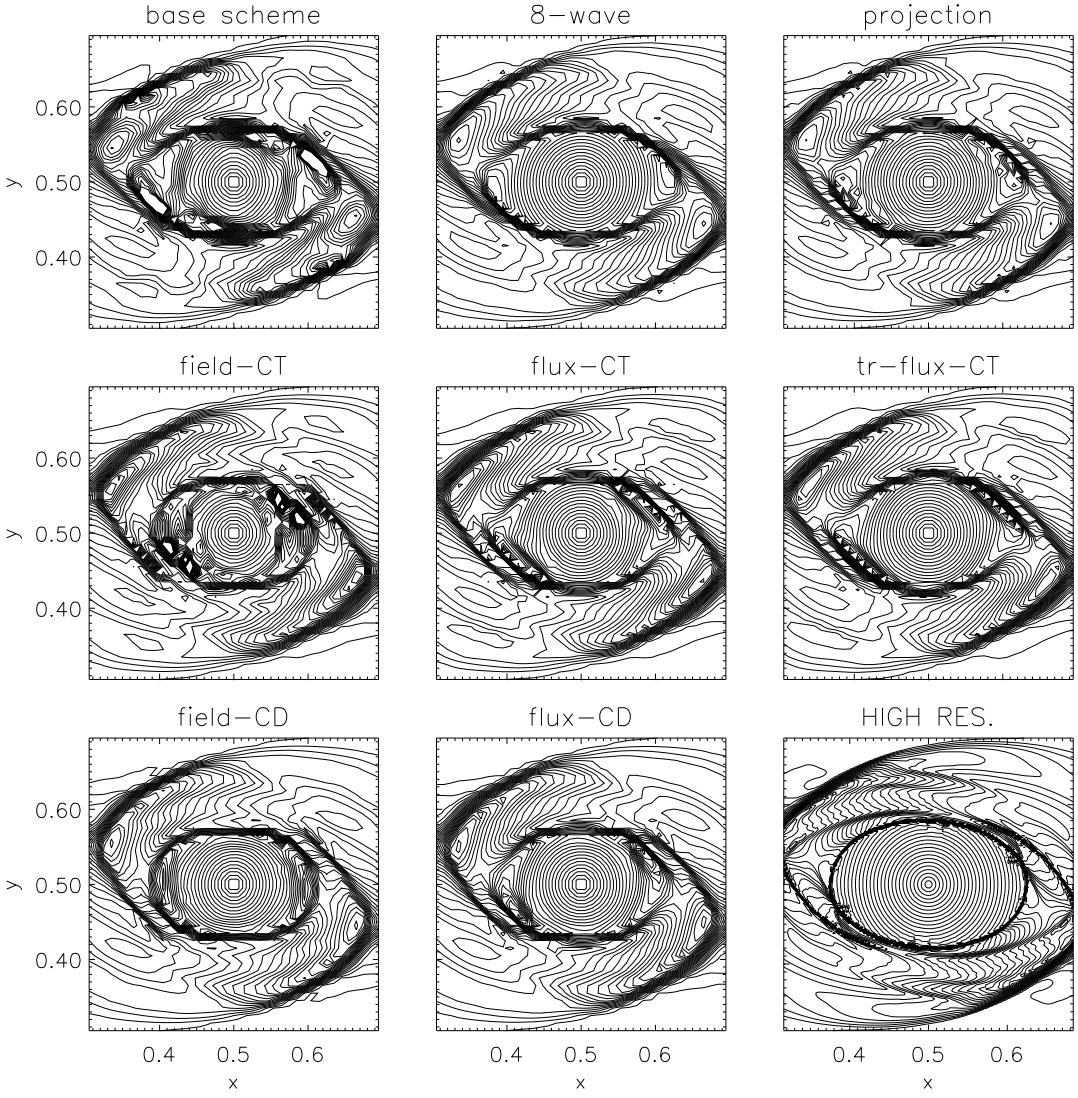

Figure 6.14: Tóth's results for rotor problem using several different MHD schemes on a resolution 100×100. The figure was taken from [88] with permission.

3's parallel AMR version in later section.

6.2.4 Cloud & Shock Interaction

The next test problem considers the interaction of a high density cloud with a strong shock wave. This problem, also known as the Dai & Woodward's cloud-shock problem [28], has been studied in several papers [56, 88] to test robustness of MHD schemes. The challenge for this problem is to demonstrate supersonic flows in the pre-shock and the post-shock regions, as well as the correct physics near the sharp boundaries of the cloud without crashing of simulation.

The same initial condition has been adopted as presented in [88]. The flow is solved on the computational domain of size $[0,1] \times [0,1]$ on a uniform $N \times N$ grid. The results were carried out to the final time $t = 0.06$ with $N = 400$. The initial discontinuity involves the left and right states along a line $x = 0.6$ parallel to the y axis. The left and right states are,

$$(\rho, u, v, w, B_x, B_y, B_z, p) = \begin{cases} (3.86859, 0, 0, 0, 0, 2.1826182, -2.1826182, 167.345) \\ \qquad \text{if } \; x \leq 0.6, \\ (1, -11.2536, 0, 0, 0, 0.56418958, 0.56418958, 1) \\ \qquad \text{if } \; x > 0.6. \end{cases} \tag{6.18}$$

The high density cloud is located on the right side of the domain, for which the circular shape is defined by $(x - 0.8)^2 + (y - 0.5)^2 = 0.15^2$. The density $\rho = 10$ and the pressure $p = 1$ are fixed in the inner region. The velocity and the magnetic fields are the same as the surrounding right state plasma values. The supersonic inflow boundary condition is imposed along the right-most boundary at $x = 1$ and

outflow boundary conditions are used for all other boundaries. A Courant number for this test was set to 0.5.

As shown in the density plots (a)∼(d) in figure 6.15, the temporal evolutions illustrate the disruption of the high density cloud as it enters the shock boundary located at $x = 0.6$. The red areas indicate the highly strong shock regions and they compares well with the results in [56, 88]. It was found by Tóth that the dimensionally splitting MHD algorithm with one step TVD scheme can easily fail due to unphysical states (e.g., negative pressure or density) produced during the violent collision of the shock and the cloud even when the diffusive MINMOD limiter was used. In the USM-IEC-SDDA scheme, the final time step was successfully reached without experiencing such problems.

6.2.5 MHD Blast Wave

The spherical explosion of the MHD blast wave problem, which was first appeared in Zachary *et al.* [95], was chosen as for the last test case in serial calculation. The following series of explosion problems concern the formation and propagation of strong MHD discontinuities, relevant to many astrophysical phenomena where the magnetic field energy has dynamical effects. Moreover, with a numerical scheme that simply fails to preserve the divergence-free constraint, it is probable to yield the onset of unphysical states involving negative gas pressure because the background magnetic pressure will increase the strength of the magnetic monopoles. (Refer the earlier discussion in Chapter 1.)

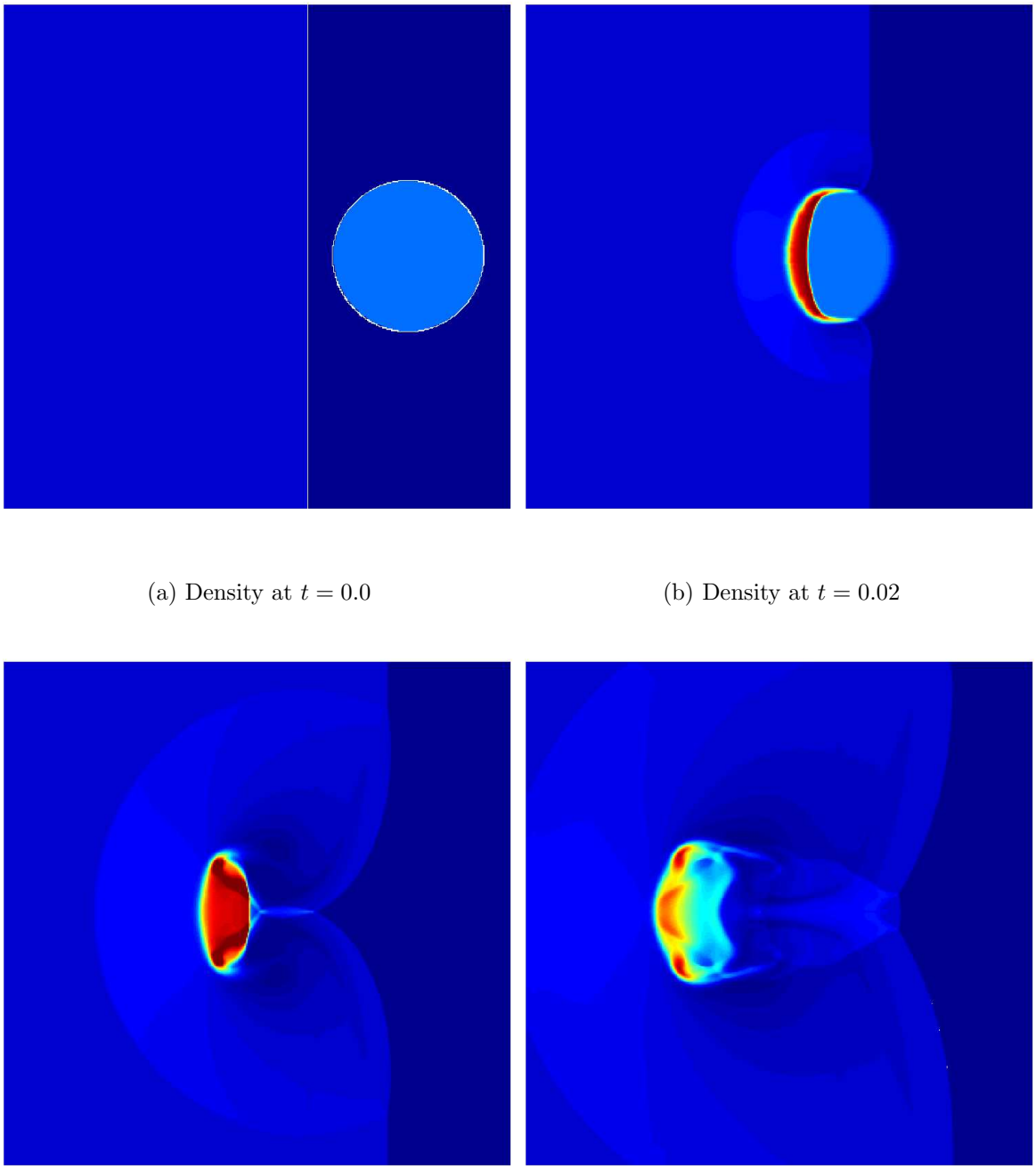

(a) Density at $t = 0.0$

(b) Density at $t = 0.02$

(c) Density at $t = 0.04$

(d) Density at $t = 0.06$

Figure 6.15: The MHD interaction between the high density cloud and shock structures resolved on 400×400 grid.

This problem was solved in three different flow regimes by taking a zero magnetic field strength, an intermediate strength, and a strong strength. The computational domain is square with a size of $[-0.5, 0.5] \times [-0.5, 0.5]$ on a grid resolution 200×200. The explosion is driven by an over-pressurized circular region at the center of the domain with the radius $r = 0.1$. The initial density is unity everywhere. The pressure of the ambient region is given as 0.1, while the pressure of the inner region is 1000. Three different regimes of the uniform magnetic field in x-direction are given as $B_x = 0, 50/\sqrt{4\pi}, 100/\sqrt{4\pi}$. The last two set-ups result very low-β ambient plasmas, $\beta = 1 \times 10^{-3}$ and 2.513×10^{-4}, respectively. Through these low-β ambient plasmas, the explosion will emit propagations of an almost spherical fast magneto-sonic shock with the fastest wave speeds in wave families. The flow takes $\gamma = 1.4$ for all three flow regimes.

In the first test case ($B_x = 0$) as shown in figure 6.16, the computed solutions are essentially identical to the one obtained with any other purely hydrodynamical codes. The 30 contour plots of the density, gas pressure, velocity square, and magnetic pressure at the final time $t = 0.01$ are shown. Notice that there is only one spherically circular symmetric hydrodynamic shock wave propagating in the outward direction. The solutions obtained here are compared well with the results in [95].

In the second set-up, illustrated in figure 6.17 with $B_x = 50/\sqrt{4\pi}$, one can apparently see an increased anisotropic explosion behavior due to the existence of the non-zero magnetic field strength in x-direction. With this intermediate strength in the B_x field, the shock waves still somewhat preserve the spherically symmetric

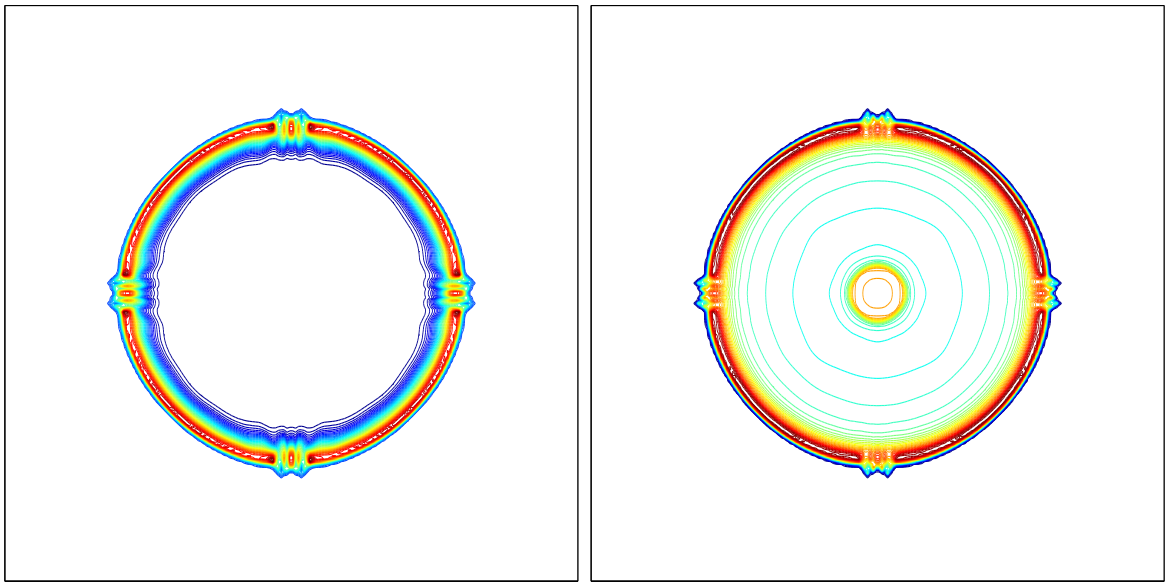

(a) Density at $t = 0.01$

(b) Gas pressure at $t = 0.01$

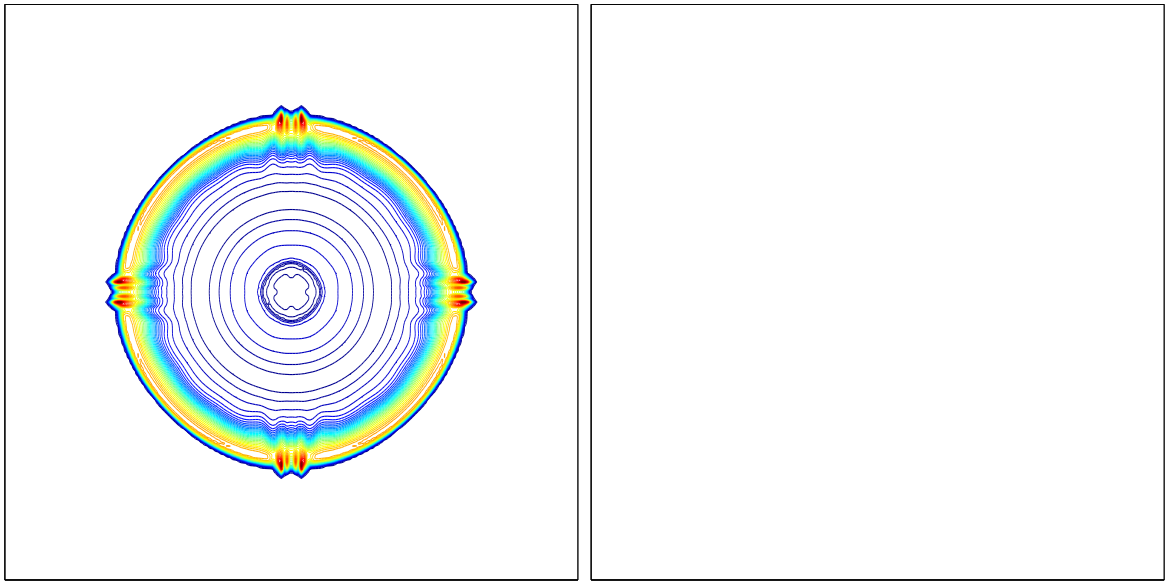

(c) Velocity square at $t = 0.01$

(d) Magnetic pressure at $t = 0.01$

Figure 6.16: The first results from the blast problem with $B_x = 0$.

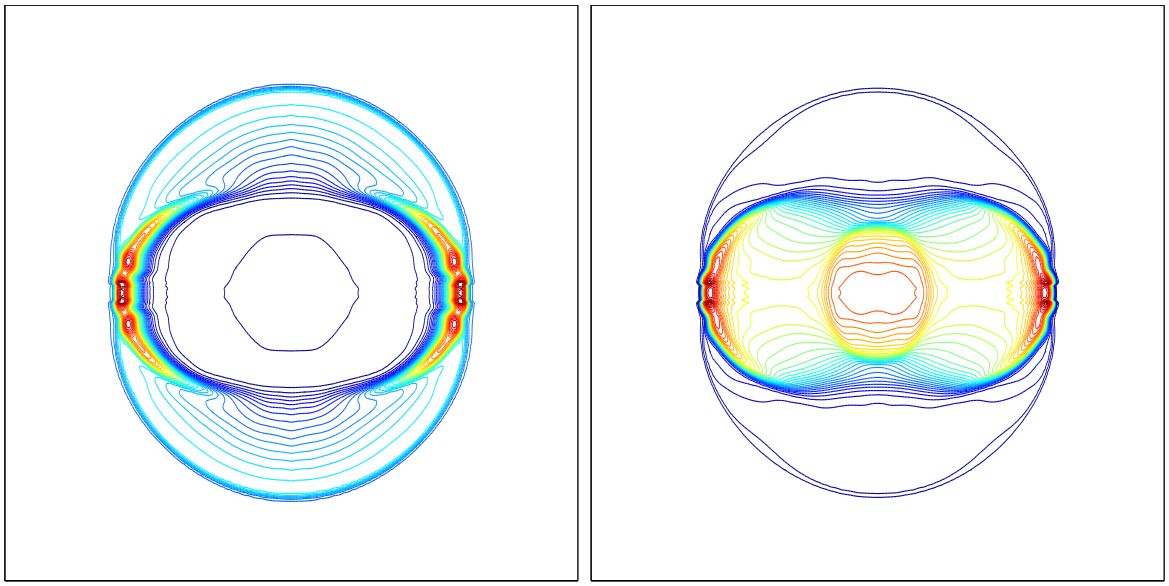

(a) Density at $t = 0.01$

(b) Gas pressure at $t = 0.01$

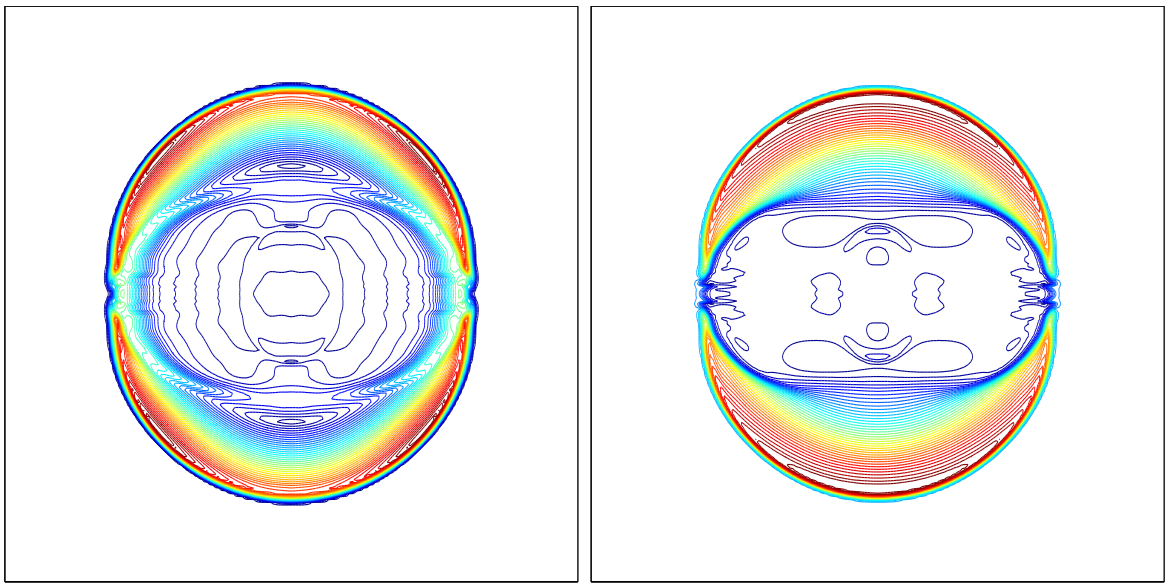

(c) Velocity square at $t = 0.01$

(d) Magnetic pressure at $t = 0.01$

Figure 6.17: The second results from the blast problem with $B_x = 50/\sqrt{4\pi}$.

shapes, as one can start to see the development of the elongated wave structures in the direction parallel to the B_x field.

For the strongest magnetic strength $B_x = 100/\sqrt{4\pi}$, the explosion now becomes highly anisotropic. As shown in figure 6.18–(b), the displacement of gas in the transversal direction (y-direction) is increasingly inhibited and the hydrodynamical shocks are propagating in both positive and negative x-directions parallel to B_x. It is also observed in plot (d) that several weak magneto-sonic waves are radiated transverse to x-direction. This process will take place until total pressure equilibrium is obtained at the center region.

It was also found by Balsara [11] that the strong wave propagation oblique to the mesh can cause the unphysical negativity of the pressure variable. Such effects will be reflected as distortions of the contours especially at the outer boundary, where a large and unphysical drop in the pressure would take place immediately ahead of the shock.

One can further consider the effects of the unphysical drop by taking the logarithm with base 10 of the pressure variable. Balsara [11] recently asserted that his new modified flux-CT scheme together with his elaborated slope limiters (e.g., denoted as the fast TVD limiter and genuinely multidimensional limiter therein) performs well for this stringent blast problem. However, as clearly illustrated in plots (a) and (b) of figure 6.19, the sudden drops of the pressure variable, especially at the regions where the direction of the strong wave propagation makes oblique to the mesh, are observed. In (a), for which the fast TVD slope limiter was adopted, the distorted profiles at the outer boundary at those regions are present. These effects

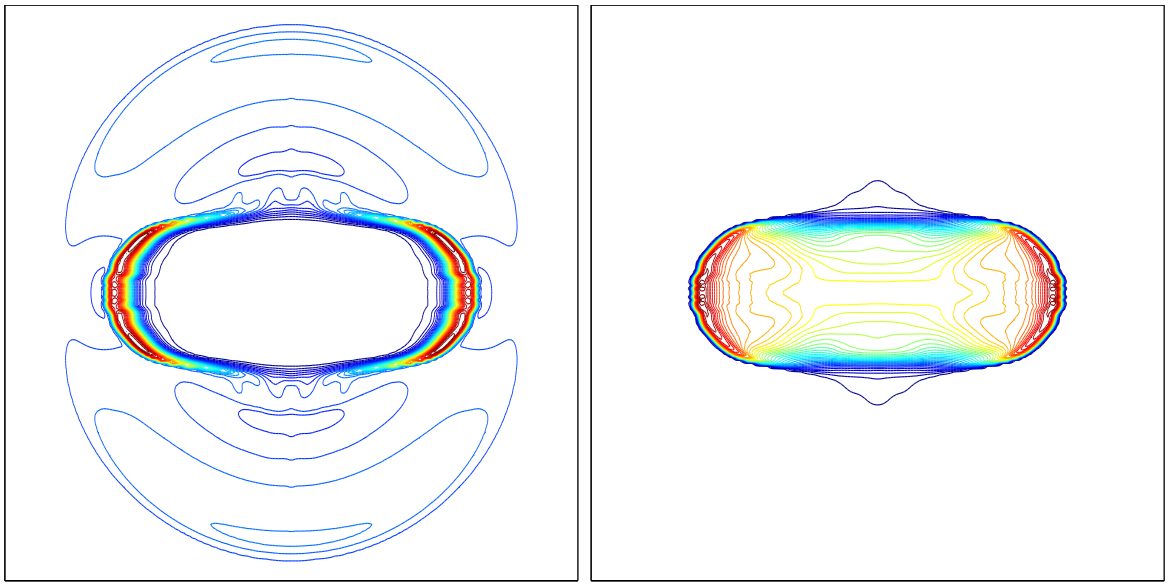

(a) Density at $t = 0.01$

(b) Gas pressure at $t = 0.01$

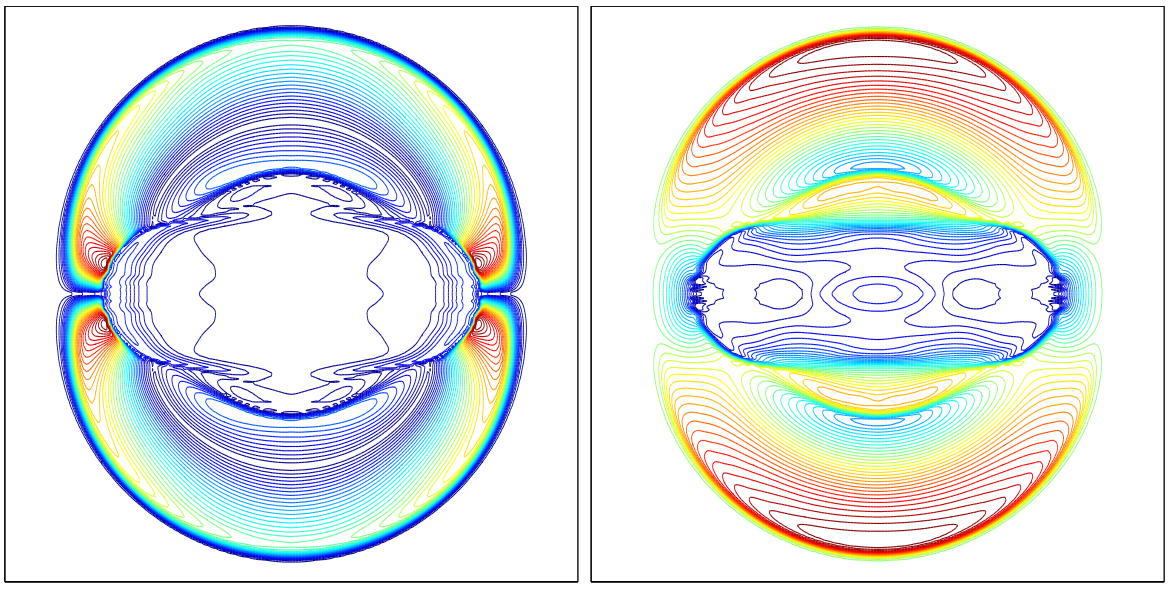

(c) Velocity square at $t = 0.01$

(d) Magnetic pressure at $t = 0.01$

Figure 6.18: The third results from the blast problem with $B_x = 100/\sqrt{4\pi}$.

are not completely removed even with the use of the genuinely multidimensional slope limiter in (b). The figures (a) and (b) are directly taken from [11] with permission. It is quite pleasing to see that the USM-IEC-SDDA scheme shows more crisp profiles at such regions in the outer boundary, as presented in (c). One can also notice that Balsara's modified flux-CT scheme is more diffusive than the USM-IEC-SDDA scheme, exhibiting a narrower band width in y direction at the center of the inner blast wave structure. It is also noticeable to see another exhibit of each scheme's diffusivity in that the overall wave structures are predicted in more detail with the USM-IEC-SDDA scheme, while there exist only simple and flat patterns with Balsara's scheme. The dissipation control from the SDDA scheme also outperforms in the pre-shock regions in both the negative and positive x axis directions, at which the plots (a) and (b) show more diffusive features.

The current study has found that the USM-IEC-SDDA scheme does not suffer from any types of the unphysical effects and maintains the clean profiles of the contours. The USM-IEC-SDDA results are found to be very reliable and accurate, as other MHD schemes are prone to generate the strong distortions of the outer contours (See [55]). For instance, figure 6.20 shows the contour plot of the density using the eight wave scheme, where the contour lines evidently show unphysical peaks and distortions. In contrast, nice and clean profiles are achieved in the USM-IEC-SDDA scheme as indicated in the plot (a) in figure 6.18.

In [55], Li has also tested several other CT-type schemes such as Balsara's modified flux-CT and the upwinding-CT (UTC) schemes. He pointed out that the negativity of the pressure variable could easily be introduced especially in low-β

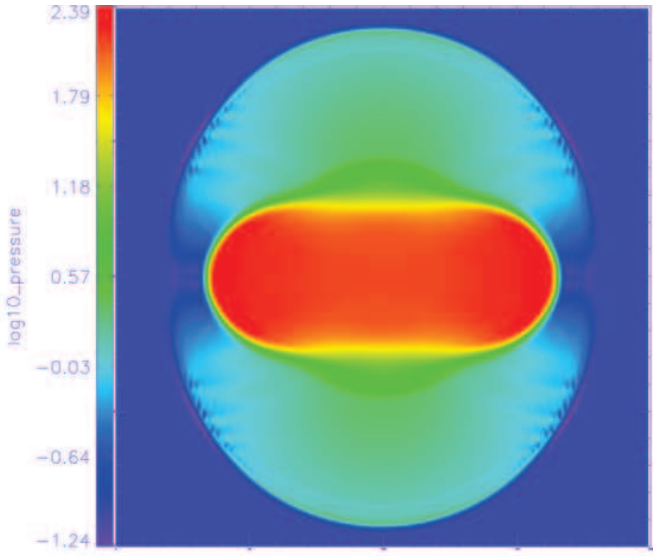

(a) $\log_{10}(p)$ at $t = 0.01$

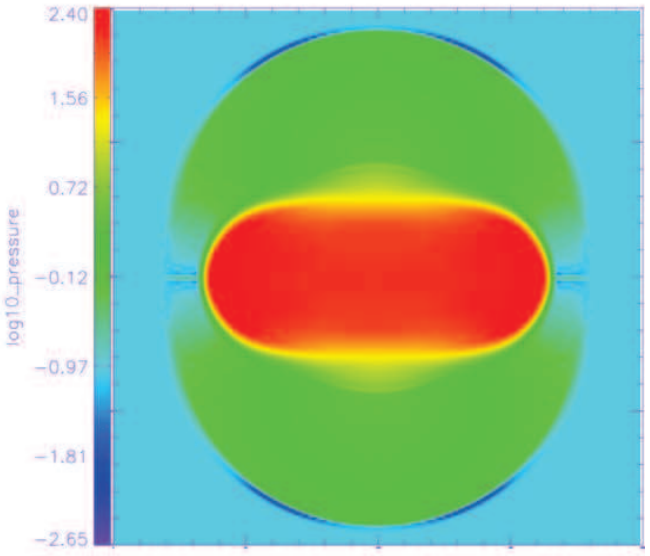

(b) $\log_{10}(p)$ at $t = 0.01$

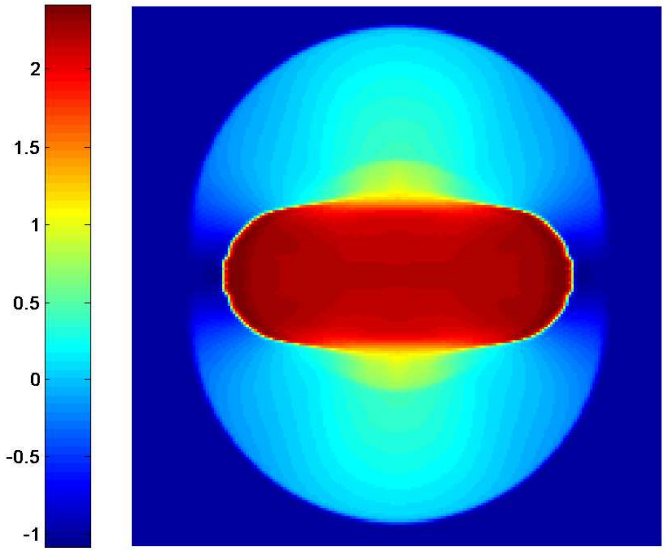

(c) $\log_{10}(p)$ at $t = 0.01$

Figure 6.19: Comparison of $\log_{10}$ of pressure for the blast problem with $B_x = 100/\sqrt{4\pi}$. The results in (a) and (b) are taken from [11] with permission. The USM-IEC-SDDA result is shown in (c).

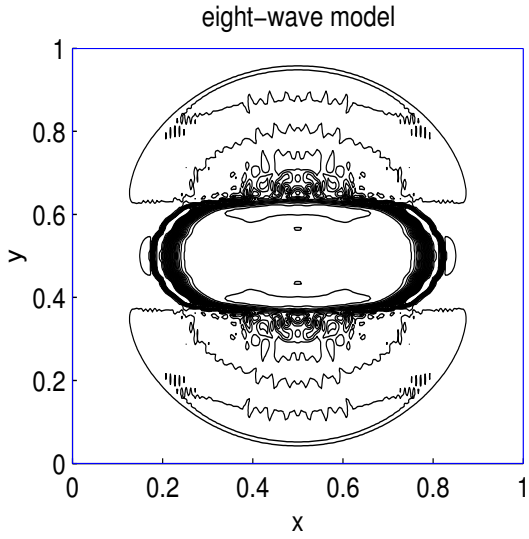

Figure 6.20: Result for blast problem using the eight wave MHD schemes. The figure was taken from [55] with permission.

simulation like this blast wave problem and found it useful to turn on the energy-fix switch in order to overcome such issue. The situations became even worse in the UTC-based schemes in that only several runs with some specific parameters successfully worked, where all the other runs failed in the tests therein.

Even with fixing the negativity issue, however, there still exist distortions of the contour lines using these schemes as indicated in figure 6.21. It can also be seen in plots of BS2 and BS3 that there is no qualitative difference between the results of adopting Balsara's new reconstruction scheme as discussed in equations (4.30) and (4.31). In all, it is quite pleasing to see that the USM-IEC-SDDA scheme performs much better than any other schemes do in this test problem.

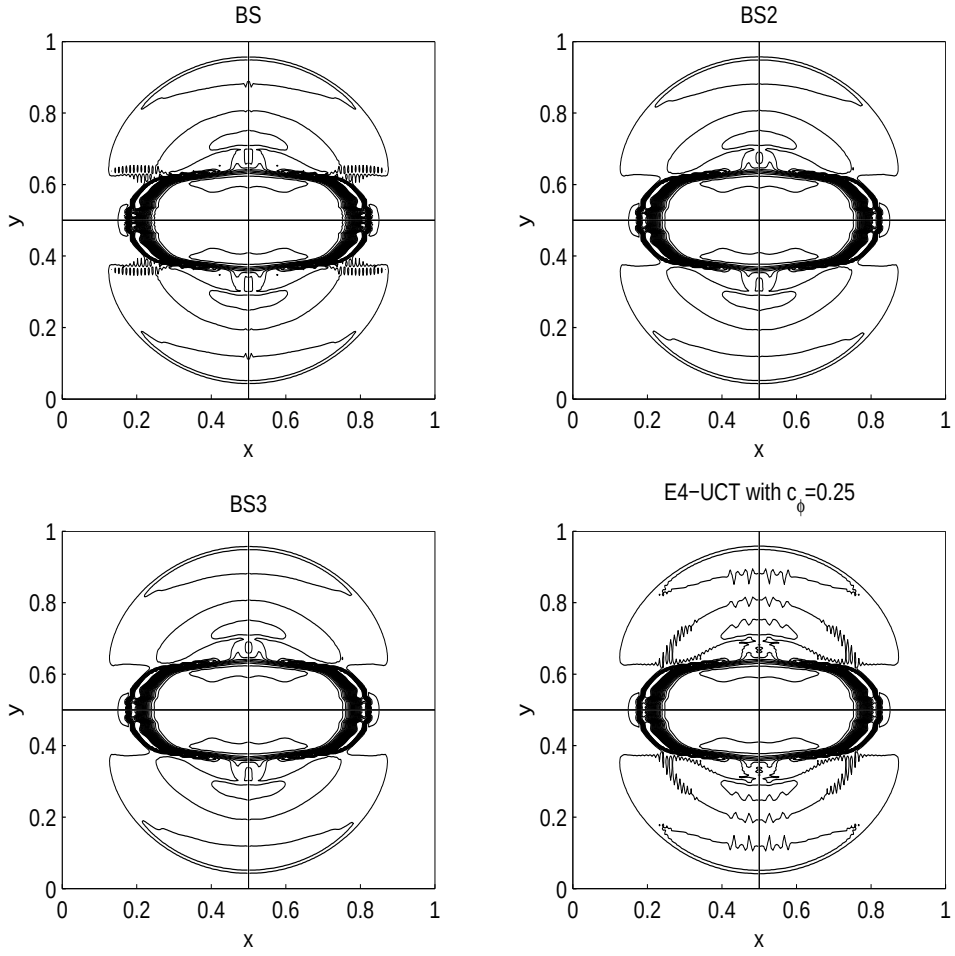

Figure 6.21: Result for blast problem using the CT-based MHD schemes. Balsara and Spicer's base CT scheme [9] with limited slopes in both x and y directions is denoted as BS, Balsara's modified flux-CT scheme [11] without applying limited slopes in the normal direction is denoted as BS2, and his modified flux-CT scheme using the new reconstruction scheme (See equations (4.30) and (4.31).) is further indicated as BS3. The upwinding-flux CT (UTC) scheme with a specific choice of parameters is shown in the last plot. The figure was taken from [55] with permission.

6.3 FLASH Parallel-AMR Tests

This section presents two results that use a parallel AMR version of the USM-IEC-SDDA scheme, which has been implemented in FLASH 3.

6.3.1 Current Sheet and Magnetic Reconnection

The current sheet test, originally taken from Gardiner *et al.* [37], concerns the magnetic reconnection process through the formation of two current sheets. This problem, in particular, is very useful to demonstrate the sensitivity of the numerical dissipation. In ideal MHD, the proper amount of dissipation will result in the diffusive effects of the magnetic field geometry, leading to changes in the magnetic field lines. As a consequence, the magnetic reconnection will take place where the magnetic field orientation is oblique to the grid.

When the magnetic reconnection occurs it can cause the magnetic flux to approach vanishingly small values. The loss in the magnetic energy is converted into heat (thermal energy). This phenomenon also changes the overall topology of the magnetic fields and hence affects the global magnetic configuration and the propagation of MHD waves, both of immense importance in the solar wind. During the reconnection process, the magnetic islands can be developed.

To simulate this, two current sheets are initialized in the computational domain

$[-0.5, 0.5] \times [-0.5, 0.5]$ in such a way that,

$$B_y = \begin{cases} \frac{B_0}{\sqrt{4\pi}} & \text{if} \quad -0.5 \leq x < -0.25, \\ -\frac{B_0}{\sqrt{4\pi}} & \text{if} \quad -0.25 \leq x \leq 0.25, \\ \frac{B_0}{\sqrt{4\pi}} & \text{if} \quad 0.25 < x \leq 0.5, \end{cases} \tag{6.19}$$

where $B_0 = 1$. The other magnetic field components B_x, B_z are set to be zeros. This problem is resolved on the six levels of refinement. Periodic boundary conditions are applied on all boundaries. The x component of the velocity is $u = u_0 \sin 2\pi y$ with $u_0 = 0.1$, and all other components are initialized with zeros. The density is unity and the gas pressure $p = 0.1$.

The temporal evolution of the B_y field is shown in figure 6.22, along with the AMR block structures at each step. The changes of the magnetic fields seed the magnetic reconnection and develop a series of magnetic islands along the two current sheets. By the time $t = 6$, the signatures of small island formations are observed and these islands are merged into the bigger islands ($t \geq 9$) by continuously shifting up and down along the current sheets. At the nodal points where the curvatures are changing dramatically, the magnetic field lines are disconnected and reconnected. In between these nodal points, the islands are easily developed by moving toward the anti-node regions. The AMR results clearly show such reconnection process, in which the merging process comes to an end until there is one big island left in each current sheet.

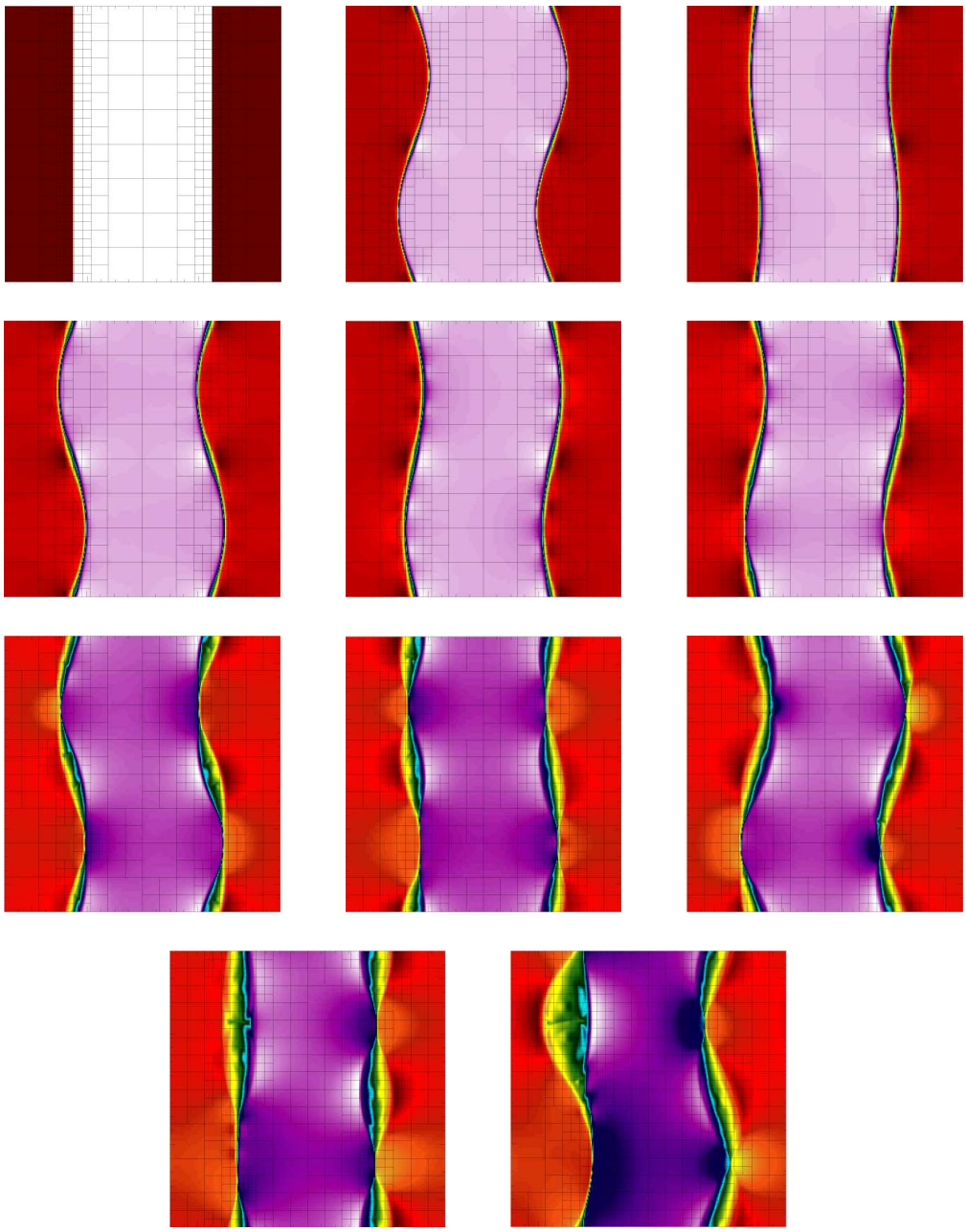

Figure 6.22: Time evolutions of B_y on the 6 levels of AMR grid. Time increases from left to right and top to bottom in normal reading order. The sequence of images at times $t = 0, 1, 2, 3, 4, 5, 6, 7, 8, 9, 10$. The formation of the magnetic islands indicates the reconnection process in the simulation.

6.3.2 Rotor Problem on Parallel AMR Grid

We finally solve the rotor problem again on the seven refinement levels of AMR grids. The initial conditions are the same as in the previous serial run.

In figure 6.23, one can clearly see that the AMR grid resolutions are effectively increased/decreased where there are sharp/smooth gradients of any given refinement variable(s). The refinement variables were set to be the density and gas pressure for this problem. At the final time step $t = 0.15$ the total number of AMR blocks has reached $2,245$.

The divergence-free constraint is also correctly resolved on this AMR grid, as shown in figure 6.24. The USM-IEC-SDDA scheme successfully preserves the $\nabla \cdot \mathbf{B}$ constraint by allowing the values only up to orders of 10^{-11}. It can be seen that the non-zero noise peaks in $\nabla \cdot \mathbf{B}$ are coherent with the locations of solution discontinuities illustrated in figure 6.23. This phenomenon is natural since the solution accuracy is decreased to first-order at discontinuities, and such errors get populated as the AMR resolutions are increased in those regions.

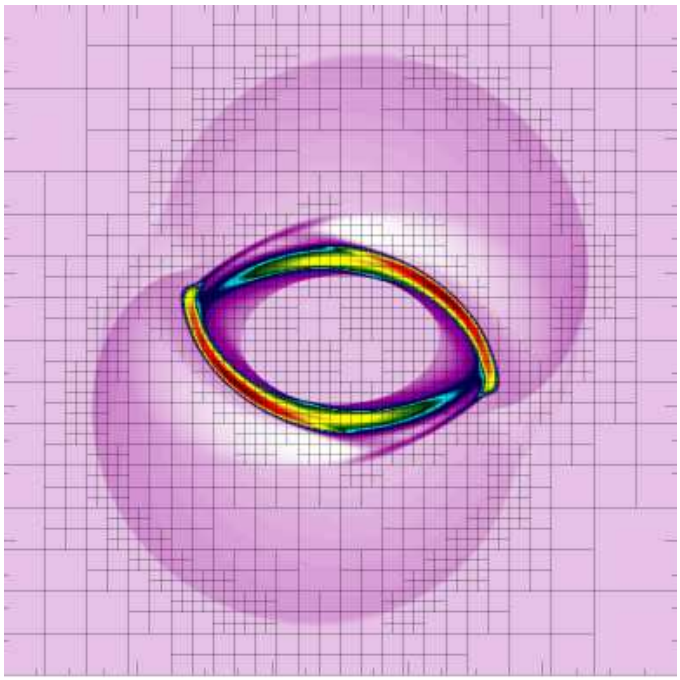

(a) Density at $t = 0.15$

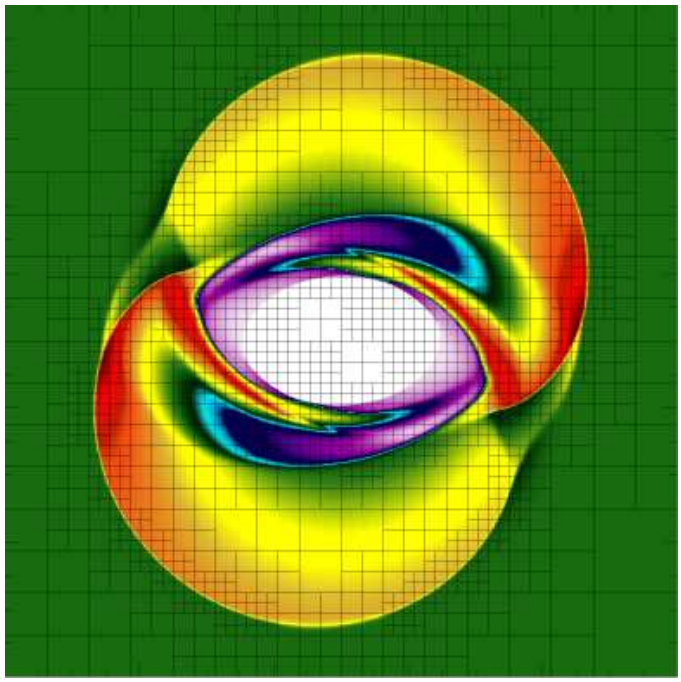

(b) Gas pressure at $t = 0.15$

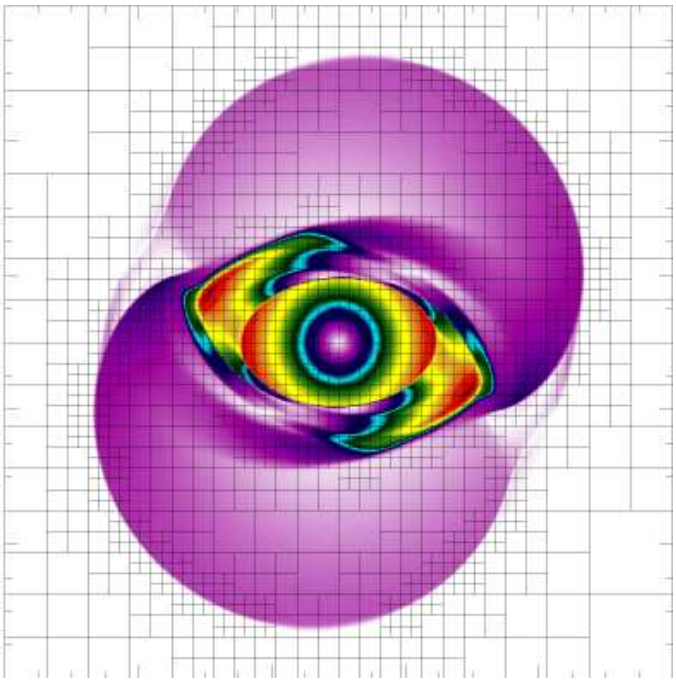

(c) Mach number at $t = 0.15$

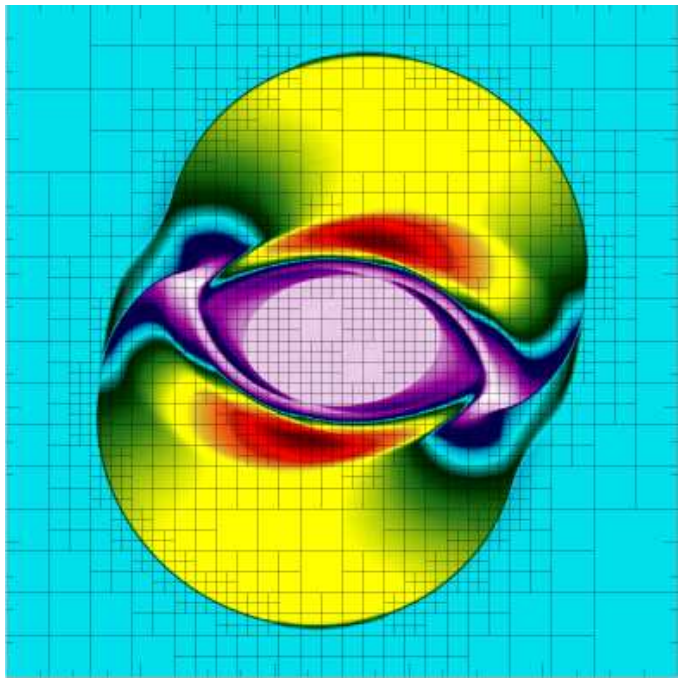

(d) Magnetic pressure at $t = 0.15$

Figure 6.23: The rotor problem on a resolution of an AMR grid.

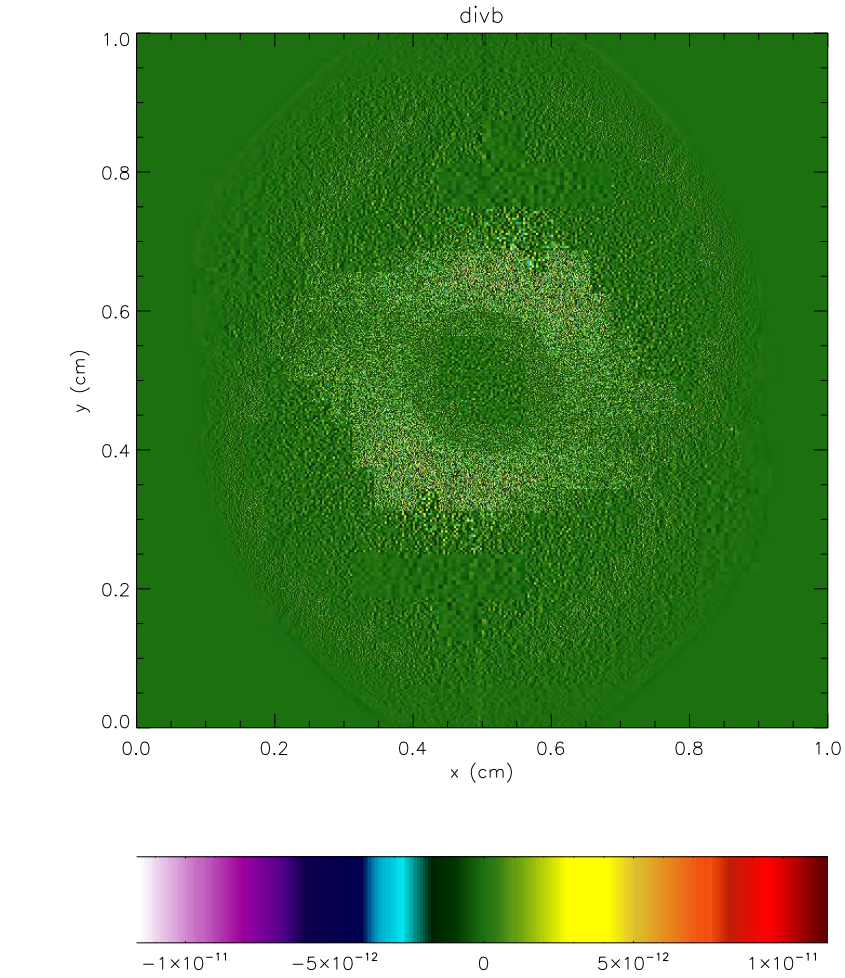

Figure 6.24: The divergence of the magnetic fields on a resolution of an AMR grid.

The 7 refinement levels are used.

Chapter 7

CONCLUSION

The most exciting phrase to hear in science,

the one that heralds new discoveries,

is not "Eureka!" but "That's funny..."

Isaac Asimov

The multidimensional USM-IEC-SDDA scheme is introduced, developed and studied in this dissertation. The method first uses characteristic analysis to account for the contribution of both normal and transversal MHD fluxes. New developments of a very efficient dissipation control algorithm (SDDA) of the staggered magnetic fields as well as an improved electric field construction (IEC) scheme have been well established. Overall, the results presented here give considerable confidence in the USM-IEC-SDDA scheme for use as a robust and reliable second-order MHD algorithm. The test results of immediate relevance to space physics problems are particularly encouraging. The following conclusions are drawn from this research:

1. The second-order accurate multidimensional unsplit MHD algorithm has been successfully developed on the staggered grid, with capability of maintaining the divergence-free constraint numerically. The method preserves the numerical MHD constraint extremely well both on a uniform grid and an AMR grid without yielding to any evidence of numerical instability or accumulation of

unphysical errors. As validation, the MHD tests presented in this study include various aspects of several stringent MHD simulations in both 1D and 2D. They consist of the evolution of a very weak magnetic field problem, strong magneto-sonic shocks, a test for the magnetic reconnection, well-known benchmark problems such as the Brio-Wu & the Orszag-Tang problems, the spinning rotor problem, and the explosion problem. The USM-IEC-SDDA scheme has been thoroughly tested and has shown to provide a confidence level in generating the correct physics required for a wide range of MHD problems.

2. The fully multidimensional MHD scheme that handles the multidimensional MHD terms is developed in the characteristic method. Such multidimensional treatments have been ignored in most of the operator splitting based MHD schemes. The approach involves correct physical consideration that many multidimensional MHD schemes should require. In particular, for many two-dimensional test cases, such multidimensional consideration will guarantee to prevent the unphysical secular growth that would deviate from the in-plane geometry. To see this phenomenon, in a two-dimensional MHD problem such as the second field loop diffusion case, spurious numerical errors proportional to $\nabla \cdot \mathbf{B}$ will affect the growth in B_z, ruining the in-plane dynamics of the problem. The current data reconstruction-evolution method resolves such issues by using the multidimensional characteristic method in a novel way.

3. A new improved methodology to construct the electric field has been developed in the IEC scheme, which establishes a more accurate way to obtain the electric

field than usual base schemes (e.g., Balsara-Spicer's flux-CT scheme). The IEC scheme takes more directional consideration of the high-order Godunov fluxes obtained from the duality relationship in the base flux-CT scheme.

4. The most remarkable development of the current study has been made in the SDDA scheme for the induction equations in that a great deal of improvement in the magnetic fields solution has been achieved, especially in the field loop tests. Without adopting the SDDA scheme for the simulation, the circular shapes of the field loop problem were shown to be easily destroyed. The proper amount of the numerical dissipation in MHD schemes is important to obtain, not only for the accuracy of solutions, but also for stability purposes as well. In the SDDA development a new way to suppress undesirable anti-dissipative effects that potentially exist in the induction equations has been established.

5. A version of parallel adaptive mesh refinement of the USM-IEC-SDDA scheme has been implemented in the new generation of FLASH. For correct implementation, the routines such as the electric field correction as well as the divergence-free treatment on the AMR grid have been implemented. The USM-IEC-SDDA scheme will serve as a MHD solver in FLASH 3 which will be publicly released.

6. Extending the USM-IEC-SDDA scheme to full three-dimensions are envisioned to be straightforward since the multidimensional issues have been addressed in this dissertation. For further applications in space physics, the accuracy of

the scheme, its robustness, and its divergence-free properties as demonstrated on the test problems of interest, encourage to pursue simulations relevant to solar wind configurations.

Appendix A

Eigensystem for MHD Equations

For the purpose of the current study, the eigenstructure of the quasi-linearized matrices $\hat{\mathbf{A}} = (\hat{\mathbf{A}}_x, \hat{\mathbf{A}}_y, \hat{\mathbf{A}}_z)$ are presented in this Appendix. Roe & Balsara [76] have presented a systematic study of the 1D ideal MHD eigensystem and introduced normalizing parameters for both right and left eigenvectors to avoid difficulties associated with coinciding wave speeds. A more general 2D eigenstructure is given here based on their study. Similar eigenstructures are also found in [70, 77, 78].

The eigensystem of the Roe matrix $\hat{\mathbf{A}}$ plays a key role in that the eigenvalues λ_k represent the wave speeds, the right eigenvectors $\mathbf{r}_k$ define the directions of the wave in phase space and the left eigenvectors $\mathbf{l}_k$ define the characteristics. The eigenstructure of the matrix $\hat{\mathbf{A}}$ is composed of the following seven waves, $\lambda_f^- \leq \lambda_a^- \leq \lambda_s^- \leq \lambda_e \leq \lambda_s^+ \leq \lambda_a^+ \leq \lambda_f^+$.

One can first define the following quantities (a 2D version is presented here):

$$u_N = \begin{cases} u & \text{for } \hat{\mathbf{A}}_x \\ v & \text{for } \hat{\mathbf{A}}_y \end{cases} \qquad u_T = \begin{cases} v & \text{for } \hat{\mathbf{A}}_x \\ u & \text{for } \hat{\mathbf{A}}_y \end{cases}, \tag{A.1}$$

$$B_N = \begin{cases} B_x & \text{for } \hat{\mathbf{A}}_x \\ B_y & \text{for } \hat{\mathbf{A}}_y \end{cases} \qquad B_T = \begin{cases} B_y & \text{for } \hat{\mathbf{A}}_x \\ B_x & \text{for } \hat{\mathbf{A}}_y \end{cases}, \tag{A.2}$$

$$\beta_N = \begin{cases} \beta_x & \text{for } \hat{\mathbf{A}}_x \\ \beta_y & \text{for } \hat{\mathbf{A}}_y \end{cases} \qquad \beta_T = \begin{cases} \beta_y & \text{for } \hat{\mathbf{A}}_x \\ \beta_x & \text{for } \hat{\mathbf{A}}_y \end{cases}. \tag{A.3}$$

The flux Jacobian matrices $\hat{\mathbf{A}}$ are decomposed into eigenvectors and eigenvalues. The eigenstructure shown here is derived from the primitive form of the

governing equations and hence one needs to multiply the Jacobian matrices (2.3) and (2.5) with the left and right eigenvectors when constructing the numerical fluxes (B.2). For the eigensystem of the matrix $\hat{\mathbf{A}}_x$, one has

- Four magneto-acoustic waves

$$\lambda_f^{\pm} = u_N \pm c_f, \tag{A.4}$$

$$\lambda_s^{\pm} = u_N \pm c_s, \tag{A.5}$$

$$\begin{aligned}\mathbf{r}_f^{\pm} = \Big(&\alpha_f\rho, \pm\alpha_f c_f, \mp\alpha_s c_s\beta_T \mathrm{sgn}b_N, \mp\alpha_s c_s\beta_z \mathrm{sgn}b_N, 0,\\ &\alpha_s\sqrt{\rho}a\beta_T, \alpha_s\sqrt{\rho}a\beta_z, \alpha_f\rho a^2\Big)^T,\end{aligned} \tag{A.6}$$

$$\begin{aligned}\mathbf{l}_f^{\pm} = \frac{1}{2a^2}\Big(&0, \pm\alpha_f c_f, \mp\alpha_s c_s\beta_T \mathrm{sgn}b_N, \mp\alpha_s c_s\beta_z \mathrm{sgn}b_N, 0,\\ &\alpha_s a\frac{\beta_T}{\sqrt{\rho}}, \alpha_s a\frac{\beta_z}{\sqrt{\rho}}, \frac{\alpha_f}{\rho}\Big),\end{aligned} \tag{A.7}$$

$$\begin{aligned}\mathbf{r}_s^{\pm} = \Big(&\alpha_s\rho, \pm\alpha_s c_s, \pm\alpha_f c_f\beta_T \mathrm{sgn}b_N, \pm\alpha_f c_f\beta_z \mathrm{sgn}b_N, 0,\\ &-\alpha_f\sqrt{\rho}a\beta_T, -\alpha_f\sqrt{\rho}a\beta_z, \alpha_s\rho a^2\Big)^T,\end{aligned} \tag{A.8}$$

$$\begin{aligned}\mathbf{l}_s^{\pm} = \frac{1}{2a^2}\Big(&0, \pm\alpha_s c_s, \pm\alpha_f c_f\beta_T \mathrm{sgn}b_N, \pm\alpha_f c_f\beta_z \mathrm{sgn}b_N, 0,\\ &-\alpha_f a\frac{\beta_T}{\sqrt{\rho}}, -\alpha_f a\frac{\beta_z}{\sqrt{\rho}}, \frac{\alpha_s}{\rho}\Big),\end{aligned} \tag{A.9}$$

- Two Alfvén waves

$$\lambda_a^{\pm} = u_N \pm c_a, \tag{A.10}$$

$$\mathbf{r}_a^{\pm} = \Big(0, 0, \pm\beta_z, \mp\beta_T, 0, -\sqrt{\rho}\beta_z \mathrm{sgn}b_N, \sqrt{\rho}\beta_T \mathrm{sgn}b_N, 0\Big)^T, \tag{A.11}$$

$$\mathbf{l}_a^{\pm} = \frac{1}{2}\Big(0, 0, \pm\beta_z, \mp\beta_T, 0, -\beta_z \mathrm{sgn}\frac{b_N}{\sqrt{\rho}}, \beta_T \mathrm{sgn}\frac{b_N}{\sqrt{\rho}}, 0\Big), \tag{A.12}$$

$$\tag{A.13}$$

- One entropy wave

$$\lambda_e = u_N, \tag{A.14}$$

$$\mathbf{r}_e = \Big(1,0,0,0,0,0,0,0\Big)^T, \tag{A.15}$$

$$\mathbf{l}_e = \Big(1,0,0,0,0,0,0,-\frac{1}{a^2}\Big). \tag{A.16}$$

Similarly for the matrix $\hat{\mathbf{A}}_y$, the eigenstructure is the same except the second and third entries as well as the fifth and sixth entries in each right and left eigenvectors are swapped. The parameters used above are defined as follow:

$$b_{x,y,z} = \frac{B_{x,y,z}}{\sqrt{\rho}}, \tag{A.17}$$

$$c_a = b_N, \tag{A.18}$$

$$c_{f,s}^2 = \frac{1}{2}\left(\frac{\gamma p + \mathbf{B}^2}{\rho} \pm \sqrt{\Big(\frac{\gamma p + \mathbf{B}^2}{\rho}\Big)^2 - \frac{4\gamma p B_N^2}{\rho^2}}\right), \tag{A.19}$$

$$\alpha_f^2 = \begin{cases} \frac{a^2-c_s^2}{c_f^2-c_s^2} & \text{if } b_T^2 + b_z^2 \neq 0, \\ 1 & \text{if } b_T^2 + b_z^2 \to 0 \ \& \ \frac{b_N^2}{\rho} = a^2 \end{cases} \tag{A.20}$$

$$\alpha_s^2 = \begin{cases} \frac{c_f^2-a^2}{c_f^2-c_s^2} & \text{if } b_T^2 + b_z^2 \neq 0, \\ 1 & \text{if } b_T^2 + b_z^2 \to 0 \ \& \ \frac{b_N^2}{\rho} = a^2 \end{cases} \tag{A.21}$$

$$\beta_{T,z} = \begin{cases} \frac{b_{T,z}}{\sqrt{b_y^2+b_z^2}} & \text{if } b_T^2 + b_z^2 \neq 0, \\ \frac{1}{\sqrt{2}} & \text{if } b_T^2 + b_z^2 \to 0. \end{cases} \tag{A.22}$$

Appendix B

Approximate Riemann Solver

A Roe-type approximate Riemann solver is implemented in the USM-IEC-SDDA scheme using the the eigenstructure of the ideal MHD governing equations outlined in Appendix A. Given two left and right Riemann states, $\mathbf{U}_L$ and $\mathbf{U}_R$, a numerical diffusive flux vector Φ takes of the form

$$\Phi = \frac{1}{2}\sum_{k=1}^{7} |\lambda_k| \mathbf{l}_k \frac{\partial \mathbf{V}}{\partial \mathbf{U}} \cdot (\mathbf{U}_R - \mathbf{U}_L) \frac{\partial \mathbf{U}}{\partial \mathbf{V}} \mathbf{r}_k, \tag{B.1}$$

where r^k and l^k are the right and left eigenvectors, and λ^k is the eigenvalue corresponding to the k-th eigenvector of a quasi-linearized flux Jacobian matrix $\hat{\mathbf{A}}$. These eigensystems are all evaluated at the corresponding averaged states. A Roe-type approximate Riemann solver evaluates the numerical flux as

$$\mathbf{F}^*(\mathbf{U}_L, \mathbf{U}_R) = \frac{1}{2}\Big\{\mathbf{F}(\mathbf{U}_R) + \mathbf{F}(\mathbf{U}_L)\Big\} - \Phi. \tag{B.2}$$

Note that the first term expressing the smooth component leads to a centered two-point formula in flux differentiation and the second is a dissipation term coming from the upwinding procedure.

BIBLIOGRAPHY

[1] Anderson, H. D., *Modern Compressible Flow*, McGraw-Hill, 1990.

[2] Anderson, H. D., *Fundamentals of Aerodynamics*, McGraw-Hill, 1991.

[3] Anderson, H. D., *Computational Fluid Dynamics: The Basic With Applications*, McGraw-Hill, 1995.

[4] Atkinson, K. E., *An Introduction to Numerical Analysis*, John Wiley & Sons, 1989.

[5] Balbás, J., Tadmor, E., Wu, C. C., Non-oscillatory Central Schemes for One- and Two-dimensional MHD Equations: I, *J. Comp. Phys.*, 201:261–285, 2004.

[6] Balls, G. T., Colella, P., A Finite Difference Domain Decomposition Method Using Local Corrections for the Solution of Poisson's Equation, *J. Comp. Phys.*, 180:25-53, 2002.

[7] Balsara, D. S., Linearized Formulation of the Riemann Problem for Adiabatic and Isothermal Magnetohydrodynamics, *The Astrophys. Supplement Series*, 116:119–131, 1998.

[8] Balsara, D. S., Total Variation Diminishing Scheme for Adiabatic and Isothermal Magnetohydrodynamics, *The Astrophys. Supplement Series*, 116:133–153, 1998.

[9] Balsara, D. S., Spicer, D. S., A Staggered Mesh Algorithm Using High Order Godunov Fluxes to Ensure Solenoidal Magnetic Fields in Magnetohydrodynamics Simulation, *J. Comp. Phys.*, 149:270–292, 1999.

[10] Balsara, D. S., Divergence-Free Adaptive Mesh Refinement for Magnetohydrodynamics, *J. Comp. Phys.*, 174:614–648, 2001.

[11] Balsara, D. S., Second-Order-Accurate Schemes For Magnetohydrodynamics With Divergence-Free Reconstruction, *The Astrophys. Supplement Series*, 151:149–184, 2004.

[12] Balsara, D. S., Kim, D., An Intercomparison Between Divergence-Cleaning and Staggered Mesh Formulations for Numerical Magnetohydrodynamics, oai:arXiv.org:astro-ph/0310728, 2003.

[13] Berger, M. J., Colella, P., Local Adaptive Mesh Refinement for Shock Hydrodynamics, *J. Comp. Phys.*, 82:64–84, 1989.

[14] Bateman, G., *MHD Instabilities*, The MIT Press, 1978.

[15] Berger, M. J., Oliger, J., Adaptive Mesh Refinement for Hyperbolic Partial Differential Equations, *J. Comp. Phys.*, 53:484–512, 1984.

[16] Biskamp, D., *Nonlinear Magnetohydrodynamics*, Cambridge University Press, 1993.

[17] Biskamp, D., *Magnetic Reconnection in Plasmas*, Cambridge University Press, 2000.

[18] Brackbill, J. U., Barnes, D. C., The Effect of Nonzero $\nabla \cdot \mathbf{B}$. on the Numerical Solution of the Magnetohydrodynamic Equations, *J. Comp. Phys.*, 87:171–200, 1990.

[19] Brecht, S. H., Lyon, J. G., Fedder, J. A., Hain, K., *Geophys. Res. Lett.*, 8:397, 1981.

[20] Brio, M., Wu, C. C., An Upwind Differencing Scheme for the Equations of Ideal Magnetohydrodynamics, *J. Comp. Phys.*, 75:400–422, 1988.

[21] Brown, J. D., Lowe, L. L., Multigrid Elliptic Equation Solver With Adaptive Mesh Refinement *J. Comput. Phys.*, 209:582–598, 2005.

[22] Calder, A. C., Fryxell, B., Plewa, T., Rosner, R., Dursi, L. J., Weirs, V. G., Dupont, T., Robey, H. F., Kane, J. O., Remington, B. A., Drake, R. P., Dimonte, G., Zingale, M., Timmes, F. X., Olson, K., Ricker, P., MacNeice, P., Tufo, H. M. On Validating An Astrophysical Simulation Code, *Astrophys. J.*, 143:201–229, 2002.

[23] Cargo, P., Gallice, G., Roe Matrices for Ideal MHD and Systematic Construction of Roe Matrices for Systems of Conservation Laws, *J. Comp. Phys.*, 136:446–466, 1997.

[24] Colella, P., Multidimensional Upwind Methods for Hyperbolic Conservation Laws, *J. Comp. Phys.*, 87:171–200, 1990.

[25] Colella, P., Woodward, P., The Piecewise Parabolic Method (PPM) for Gasdynamical Simulations, *J. Comp. Phys.*, 54:174–201, 1984.

[26] Crockett, R. K., Colella, P., Fisher, R. T., Klein, R. I., McKee, C. F., An Unsplit, Cell-Centered Godunov Method for Ideal MHD, *J. Comput. Phys.*, 203:422–448, 2005.

[27] Dai, W., Woodward, P., An Approximate Riemann Solver for Ideal Magnetohydrodynamics, *J. Comput. Phys.*, 111:354–372, 1994.

[28] Dai, W., Woodward, P., A Simple Finite Difference Scheme for Multidimensional Magnetohydrodynamics, *J. Comput. Phys.*, 142:331–369, 1998.

[29] Deane, A. E., Parallel Performance of An AMR MHD code, Parallel CFD, Egmond En Zee, Netherlands, 2001.

[30] Dedner, A., Kröner, D., Rohde, C., Wesenberg, M., Godunov Methods: Theory and Applications, Kluwer Academic/Plenum Publishers, New York, pages 209–216, 2001.

[31] Dedner, A., Kemm, F., Kröner, D., Munz, C. D., Schnitzer, T., Wesenberg, M., Hyperbolic Divergence Cleaning for the MHD Equations, *J. Comput. Phys.*, 175:645–673, 2002.

[32] Dendy, R. O., Editor, *Plasma Physics: An Introductory Course*, Cambridge University Press, 1993.

[33] DeVore, C. R., Flux Corrected Transport Techniques for Multidimensional Compressible Magnetohydrodynamics, *J. Comput. Phys.*, 92:142, 1991.

[34] Evans, C. R., Hawley, J. F., Simulation of Magnetohydrodynamic Flows: A Constrained Transport Method, *Astrophys. J.*, 332:659–677, 1988.

[35] Freidberg, J. P., Ideal Magnetohydrodynamic Theory of Magnetic Fusion System, *Review of Modern Phys.*, 54:801–903, 1982.

[36] FLASH, version 2.3, <http://flash.uchicago.edu>, June, 2003.

[37] Gardiner, T., Stone, J., An Unsplit Godunov Method for Ideal MHD via Constrained Transport, *J. Comput. Phys.*, 205:509–539, 2005.

[38] Goedbloed, H., Poedts, S., *Principles of Magnetohydrodynamics*, Cambridge University Press, 1991.

[39] Goldstein, M. L., Roberts, D. A., Deane, A. E., Ghosh, S., Numerical Simulation of Alfvénic Turbulence in the Solar Wind, *J. Geophys. Res.*, 104, A7:14437–14451, 1999.

[40] Goldstein, M. L., Roberts, D. A., Burlaga, L. F., Sirigar, E., Deane,A. E., North-south flows observed in the outer heliosphere at solar minimum: Vortex streets or corotating interaction regions?, *J. Geophys. Res.*, 106, A8:15973–15984, 2001.

[41] Gombosi, T. I., DeZeeuw, D. L., Häberli, R. M., Powell, K. G., Three Dimensional Multiscale MHD Model of Cometary Plasma Environments, *J. Geophys. Res.*, 101, A7:15233–15253, 1996.

[42] Gottlieb, S., Shu, C. W., Total Variation Diminishing Runge-Kutta Schemes, *Math. of Comp.*, 67:73–85, 1998.

[43] Goossens, M., *An Introduction to Plasma Astrophysics And Magnetohydrodynamics*, Kluwer Academic Publishers, 2003.

[44] Grifiths, D. J., *Introduction to Electrodynamics*, Prentice-Hall, 1989.

[45] Harten, A., On the Symmetric Form of Systems of Conservation Laws with Entropy, *J. Comput. Phys.*, 49:151–164, 1983.

[46] Howell, L. H., Bell, J., An Adaptive Mesh Projection Method for Viscous Incompressible Flow, *SIAM J. Sci. Comput.*, 18:996–1013, 1997.

[47] Huba, J. D., *NRL Plasma Formulary*, Naval Research Laboratory, 2004.

[48] Janhunen, P., A Positive Conservative Method for Magnetohydrodynamics Based on HLL and Roe Methods, *J. Comput. Phys.*, 160:649, 2000.

[49] Kirk, J. G., Melrose, D. B., Priest, E. R., *Plasma Astrophysics*, Saas-Fee Advanced Course 24, Springer, 1994.

[50] Kundu, P. K., Cohen, I. M., *Fluid Mechanics*, Academic Press, Second Edition, 2002.

[51] Laney, C. B., *Computational Gas Dynamics*, Cambridge University Press, 1998.

[52] Lee, D., Deane, A., A Parallel Unsplit Staggered Mesh Algorithm for Magnetohydrodynamics, Parallel CFD, Egmond En Zee, Netherlands, 2005.

[53] LeVeque, R. J., *Numerical Methods for Conservation Laws*, Birkhäuser, 1992.

[54] LeVeque, R. J., Mihalas, D., Dorfi, E. A., Müller, E., *Computational Methods For Astrophysical Fluid Flow*, Saas-Fee Advanced Course 27, Springer, 1997.

[55] Li, S., Note on Upwinding Constrained Transport Method for Ideal Magneto-hydrodynamics, *Los Alamos Report*, LA-UR-03-8925, 2003.

[56] Li, S., Li, H., A Modern Code for Magneto-hydrodynamics or Hydrodynamics Equations, *Los Alamos Report*, LA-UR-03-8925, 2003.

[57] Linde, T. J., *A Three-Dimensional Adaptive Multifluid MHD Model of the Heliosphere*, Ph.D. Thesis, The University of Michigan, 1998.

[58] Linde, T. J., Gombosi, T. I., Roe, P. L., Powell, K. G., DeZeeuw, D. L., The Heliosphere in the Magnetized Local Interstella Medium: Results of a 3D MHD Simulation, *J. Geophys. Res.*, 103, A2:1889–1904, 1998.

[59] Londrillo, P., Del Zanna, L., High Order Upwind Schemes For Multidimensional Magnetohydrodynamics, *Astrophys. J.*, 530:508–524, 2000.

[60] Londrillo, P., Del Zanna, L., On the Divergence-Free Condition in Godunov-Type Schemes for Ideal Magnetohydrodynamics: The Upwind Constrained Transport Method, *J. Comp. Phys.*, 195:14–48, 2004.

[61] Mathieu, J., Scott, J., *An Introduction to Turbulent Flow*, Cambridge University Press, 2000.

[62] MacNeice, P., Olson, K., PARAMESH version 3.4, <http://www.physics.drexel.edu/∼olson/paramesh-doc/Users_manuals/amr.html>

[63] Myong, R. S., Roe, P. L., On Godunov-Type Schemes for Magnetohydrodynamics: 1. A Model System, *J. Comp. Phys.*, 147:545–567, 1998.

[64] Murawski, K., Tanaka, T., Modern Numerical Schemes For Solving Magnetohydrodynamic Equations, *Astrophysics and Space Science*, 254:187-210, 1997.

[65] Orszag, A., Tang, C. M., Small-scale Structure of Two-Dimensional Magnetohydrodynamics Turbulence, *J. Fluid Mech.*, 90:129–143, 1979.

[66] Parks, G. K., *Physics of Space Plasmas: An Introduction*, Perseus Books, 1991.

[67] Pen, U., Arras, P., Wong, S., A Free, Fast, Simple and Efficient TVD MHD Code, *The Astrophys. Supplement Series*, 149:447–455, 2003.

[68] Powell, K. G., A Riemann Solver for Ideal MHD: That works in More Than One Dimension, ICASE Report, 94–24, Langely, VA, 1994.

[69] Powell, K. G., Roe, P. L., Myong, R. S., Gombosi, T. I., De Zeeuw, D. L., An Upwind Scheme for Magnetohydrodynamics, *AAIA 12th Computational Dynamics Conference*, AAIA-95-1704, San Diego, CA, 1995.

[70] Powell, K. G., Roe, P. L., Linde, T. J., Gombosi, T. I., De Zeeuw, D. L., A Solution-Adaptive Upwind Scheme for Ideal Magnetohydrodynamics, *J. Comp. Phys.*, 154:284–309, 1999.

[71] Roberts, D. A., Ghosh, S., Goldstein, M. L.,Matthaeus, W. H., Magneto-hydrodynamic Simulation of the Radial Evolution and Stream Structure of Solar-Wind Turbulence, *Phys. Rev. Lett.*, 67,27:3741–3744, 1991.

[72] Roberts, D. A., Goldstein, M. L., Matthaeus, W. H., Ghosh, S., Velocity Shear Generation of Solar Wind Turbulence, *J. Geophys. Res.*, 97, A11:17115–17130, 1992.

[73] Roberts, D. A., Wiltberger, M. J., Nonequilibrium, Large-Amplitude MHD Fluctuations in the Solar Wind, *J. Geophys. Res.*, 100, A4:3405–3415, 1995.

[74] Roberts, D. A., Goldstein, M. L., Deane A. E., Ghosh, S., Quasi-Two-Dimensional MHD Turbulence in Three-Dimensional Flows, *Phys. Rev. Lett.*, 82:548–551, 1999.

[75] Roe, P. L., Approximate Riemann Solvers, Parameter Vectors, and Difference Schemes, SIAM, *J. Comp. Phys.*, 43:357–372, 1981.

[76] Roe, P. L., Balsara, D. S., Notes on the Eigensystem of Magnetohydrodynamics, SIAM, *J. Appl. Math.*, 56:57–67, 1996.

[77] Ryu, D, Jones, T. W., Numerical Magnetohydrodynamics in Astrophysics: Algorithm and Tests for One-dimensional Flow, *Astrophys. J.*, 442:228–258, 1995.

[78] Ryu, D, Miniati, F., Jones, T. W., Frank, A., A Divergence-Free Upwind Code For Multidimensional Magnetohydrodynamic Flow, *Astrophys. J.*, 509:244–255, 1999.

[79] Ruderman, M. S., Goldstein, M. L., Roberts, D. A., Deane, A. E., Ofman, L., Alfvén wave phase mixing driven by velocity shear in two-dimensional open magnetic configurations, *J. Geophys. Res.*, 104, A8:17057–17068, 1999.

[80] Schey, H. M., *div grad curl and all that*, W. W. Norton & Company, Inc., Fourth Edition, 2005.

[81] Shu, F. H., *The Physics of Astrophysics, Volume II, Gas Dynamics*, University Science Books, 1992.

[82] Stone, J., The Athena Test Suite, <http://www.astro.princeton.edu/∼jstone>

[83] Stone, J., Norman, M., ZEUS-2D: A Radiation Magnetohydrodynamics Code for Astrophysical Flows in Two Space Dimensions. II. The Magnetohydrodynamic Algorithms and Tests, *Astrophys. J.*, 80:791–818, 1992.

[84] Sturrock, P. A., *Plasma Physics: An Introduction to the Theory of Astrophysical, Geophysical & Laboratory Plasmas*, Cambridge University Press, 1994.

[85] Torrilhon, M., Balsara, D. S., High Order WENO Schemes: Investigations on Non-Uniform Convergence for MHD Riemann Problems *J. Comp. Phys.*, 201:586–600, 2004.

[86] Toro, E. F., *Riemann Solvers and Numerical Methods for Fluid Dynamics, A Practical Introduction*, Springer, 1997.

[87] Tóth, G., Computational Magnetohydrodynamics; Notes For An Introductory Level Course, <http://hermes.elte.hu/~gtoth>, 1998.

[88] Tóth, G., The $\nabla \cdot \mathbf{B} = 0$ Constraint in Shock-Capturing Magnetohydrodynamics Codes, *J. Comp. Phys.*, 161:605–656, 2000.

[89] Tóth, G., Conservative and Orthogonal Discretization for the Lorentz Force, *J. Comp. Phys.*, 182:346–354, 2002.

[90] Tóth, G., Roe, P., L., Divergence- and Curl- Preserving Prolongation and Restriction Formulas, *J. Comp. Phys.*, 180:736–750, 2002.

[91] Inan, U. S., Inan, A. S., *Electromagnetic Waves*, Prentice Hall, 2000.

[92] White, F., *Viscous Fluid Flow*, McGraw-Hill, Second Edition, 1991.

[93] Yang, H., An Artifical Compression Method for ENO Schemes: The Slope Modification Method, *J. Comp. Phys.*, 89:125–160, 1990.

[94] Yee, K. S. Numerical Solution of Initial Boundary Value Problems Involving Maxwell's Equations in Isotropic Media *IEEE Trans. Antenna Propagation*, AP-14:302–307

[95] Zachary, A., Malagoli, A., Colella, P., A Higher-Order Godunov Method for Multidimensional Ideal Magnetohydrodynamics, *J. Comp. Phys.*, 2:263–284, 1994.

[96] Zachary, A., Colella, P., A Higher-Order Godunov Method for the Equations of Ideal Magnetohydrodynamics, *J. Comp. Phys.*, 99:341–347, 1992.